Phase Change Materials for Controllable Stiffness of Robotic Joints

Bingyin Ma

Submitted in accordance with the requirements for the degree of
Doctor of Philosophy

The University of Leeds
Institute of Design, Robotics and Optimisation
School of Mechanical Engineering

September 2018

The candidate confirms that the work submitted is his own and appropriate credit has been given within the thesis where reference has been made to the work of others.

Acknowledgements

Undertaking this PhD has been a life-changing experience for me and it would not be possible to do without the guidance and support I received from many people.

I would like to thank my mom and dad for believing in me and always being there for me. I am forever indebted to my parents for giving me the opportunities and support that have made me who I am. Thank you to my mother, Zhang Li-Jun, for raising me, guiding me and encouraging me to explore new directions in life. This journey would not have been possible if not for you, and I dedicate this milestone to you, mom.

I owe my deepest gratitude to my supervisor Professor Robert Richardson, you have been a tremendous mentor for me. Your guidance helped me in all the time of research and writing of this thesis. Without your enthusiasm, encouragement, support and continuous optimism this thesis could hardly have been completed. I could not have imagined having a better boss for my PhD study.

To my friends, thank you for supporting me through this entire process. Special thanks to Jason Liu, Wang Qiang, Hongkai Ye and Farhan Maqbool for your friendship and generous help.

Thank you, Marcy. *Merci.*

.

Abstract

Snake-like manipulators are well suited for operation in restricted and confined environments where the manipulator body can bend around obstacles to place an end effector at a difficult to access location. They require high stiffness when self-supporting weight against gravity and undertake precision manipulation task, but also require soft properties when operating in complex and delicate environments. A controllable stiffness manipulator has the potential to meet the application demands as it can switch between rigid and soft state.

This thesis experimentally investigates the properties of four materials, (low melting point solder, hot-melt adhesive, low melting point alloy and granular material) as candidates for mechanically altering the stiffness of the joints/modules in snake-like manipulators. These materials were evaluated for bonding strength, repeatability, and activation time. Modules for a snake-like manipulator were fabricated using 3D printing and silicone casting techniques including, for the first time, variable stiffness joints that use hot-melt adhesive and low melting point alloy. These modules were evaluated for stiffness properties and low melting point solder based module was found to achieve a stiffness change 150X greater than the state of the art granular material approach. In addition, the proposed modules were able to support 25X of their own weight.

Table of Contents

List of Tables

List of Figures

List of Abbreviations

LMPS	Low Melting Point Solder
HMA	Hot-melt Adhesive
LMPA	Low Melting Point Alloy
GM	Granular Material
LMPS(R)	Revolute joint that Utilizes LMPS-based Locking Mechanism
HMA(R)	Revolute joint that Utilizes HMA-based Locking Mechanism
LMPS(S)	Spherical Joint that Utilizes LMPS-based Locking Mechanism
HMA(S)	Spherical Joint that Utilizes HMA-based Locking Mechanism

Chapter 1
Introduction

This chapter discusses the background, motivation, aims and objectives of this research. The contribution of the study is highlighted, and the structure of the thesis is presented.

1.1 Introduction

There are many scenarios where there is a need to deploy a tool through a small hole to collect data or manipulate objects. These challenges include, for example: i) Robotic minimally invasive surgery where procedures are performed through the smallest incision and often require exerting cutting forces on tissue, the retraction of the surgically removed tissue or the transportation of relatively heavy tool. ii) Search and rescue where slender tools need to be inserted through small holes in collapsed structures.

The challenge is to create a slender articulating tool that behaves ‘soft’ when navigating the environment to reach a location as not to exert undesired forces, but has the capability to become rigid when deploying tools or exerting external forces. Rigidity is particularly important as the length of the tool increases and it is required to support its own weight against gravity. Snake-like manipulators offer the potential to meet these application demands.

1.1.1 Snake-like Manipulator

Snake-like manipulators are formed from large numbers of serially configured joints that allow the manipulator body to follow complex paths, with appearance similar to a biological snake. These manipulators are well suited for operation in restricted and confined environments where the manipulator body can bend around obstacles to place an end effector at a difficult to access location.

Snake-like manipulators can be broken down into two classifications based on the actuation method. Distributed actuator snake arm manipulators have actuators distributed across their length, typically an actuator for each joint. They have the ability of large angle changes at each section and therefore can have a small radius of curvature – ideal for grasping or holding slender objects. However, the weight of distributed actuators across the snake body greatly reduces the robot’s capability for unsupported reaching, i.e. the number of body sections that can be lifted against gravity is limited.

Furthermore, snake robots with on-board actuators have a relatively large cross section area in order to accommodate the distributed motors [1, 2].

An alternative approach to the distributed actuators is to place all the actuators in one location at the base and use tendons (wires) to transmit forces from the base to the sections of the snake. This removes the weight of the actuators from the snake sections and allows a much longer unsupported length and slender cross section. However, due to the design of many wires actuated snake arms, they are not capable of producing as large angles as distributed actuator snakes. In addition, externally actuated snake-manipulators have an inherent disadvantage comparing to its counterpart: lack of stiffness or strength.

In application where self-supporting snake manipulators are required or where the snake-like manipulator is required to be as slender as possible (e.g. to enter through a small hole such in surgery or search and rescue tasks) tendon based snake arm manipulators are normally the only option.

Snake-like manipulators can also be categorized into hard manipulators and soft manipulators on the basis of their underlying materials. Hard manipulators are designed to be stiff so that external forces do not affect the accuracy of movement or precision of manipulation. Soft manipulators are constructed with soft and deformable materials (e.g. silicone, rubber, or compliant mechanical parts like springs) of that the inherent compliance minimises the force applied during contact with objects to reduce damage [3, 4].

While hard manipulators are capable of being accurate, many of them lack the ability to alter the rigidity or stiffness when required [5, 6]. One approach to a stiffness controlled snake-manipulator used friction between joints to modulate the overall stiffness of the manipulator [7, 8]. Although this design is impressive, it lacks the ability to alter the stiffness individual sections independently.

Soft manipulators and hard manipulators exploit different mechanisms to enable dexterous mobility. Soft manipulators have large deformability and compliance, they can be deployed through opening diameter smaller than their original dimensions [3]. Soft manipulators can actively interact with the environment without causing damages, which makes them appeal for the medical application and human-safe industry. However, their inherent advantages result in limited output force, reducing the quality of manipulation precision. High forces are tough to achieve without the support of any rigid

components. The core challenge of soft robotics is the control of their deformability and softness.

1.1.2 Stiffness Modulation

In order to overcome aforementioned challenges, researchers have focused on robots with the capability of stiffness modulation. Stiffness modulation is the way for hard and soft robots to interact with the working environment effectively [9]. Softness enables dexterity and prevents the damage to the environment, whereas rigidity can transfer the forces to the environment when required. This kind of robot is undoubtedly promising, especially when robots need to operate in a confined or unstructured environment.

The growing interest in stiffness modulation has led to an increased interest in smart materials. Specifically, materials can rapidly and reversibly change their stiffness. Examples include magnetorheological (MR) fluids [10], electrorheological (ER) fluids [11], thermorheological (TR) fluids [12, 13], and granular materials [14-16]. MR and ER fluids have fast transition time and good relative stiffness change. However, they suffer from low repeatability [17], i.e. fluids are subjected to thickening after prolonged use. TR fluids are an interesting solution to realize stiffness modulation. There have been a series of attempts with wax [18], hot-melt adhesive [18], and low melting point alloy [17, 19] to create controllable stiffness elements in soft robots. However, these materials are thermally activated, which means they require additional heating elements. Their efficiency is affected by thermal input. Granular jamming has been gaining attention recently as an alternative way to achieve soft manipulator with controllable stiffness capability [14-16]. Granular jamming uses vacuum pressure to cause powder materials to transition between solid-like and fluid-like states. However, it requires high vacuum pressure and a large volume of granular materials to achieve a significant stiffness modulation [9]. Therefore, it is challenging to scale smaller. Although there is no clear trend to provide stiffness modulation capability for robots, the awareness of the importance of such feature is emerging in robotics community.

This research investigates the approaches for on-demand stiffness modulation capability, incorporates current technologies into the design of a snake-like manipulator. Although variable stiffness robotics is a very recent filed, this technique could potentially pave the way to new capabilities for manipulation, operation and extraction.

1.2 Motivation for Research

The motivation for this research is to undertake study into controllable stiffness mechanisms for modular snake-like manipulator in order to expand capabilities of current systems. These capabilities will enable the manipulator to switch between soft state and rigid state when required. Softness will prevent the damage to the working environment, and rigidity will transfer the force and provide the stability during the operation.

This thesis discusses the path taken from identifying the limitations of hard and soft robots to the synthesis, design, analysis and experimentation of the controllable stiffness mechanisms that can be employed by the snake-like manipulator.

1.3 Aims and Objectives

The aim of this research to analyse and validate methods for controllable stiffness modules for a modular snake-like manipulator. To fulfil the research aim, the following objectives are highlighted:

1. To identify the possible materials that can be used for the development of the controllable stiffness mechanisms.
2. To investigate the properties of the identified materials related to the design of the controllable stiffness mechanisms.
3. To design the controllable stiffness mechanism that can be implemented as module of a snake-like manipulator.
4. To experimentally characterise the performance of the single module with emphasis on measurement of stiffness and response time.

1.4 Statement of Contribution

The areas of the original work carried out in this research are highlighted below:

1. Three thermorheological fluids (i.e. Field’s Metal, hot-melt adhesive, and Lens 136) were selected and investigated to develop controllable stiffness modules for modular snake-like manipulators. Field’s metal, hot-melt adhesive and Lens 136 materials were chosen for this application for the first time and found significant stiffness increases for the developed modules.

2. The properties of Field's Metal were experimentally investigated under different conditions for the first time (i.e. the temperature influence on shear strength and the change of shear strength over repetitions).
3. Finite element analysis was carried out on the bellows-like silicone structure. The number of the bellows was optimised.

1.5 Structure of Thesis

This thesis presents an exploration of modular approaches to construct a controllable stiffness manipulator through five related studies, each of which is discussed thoroughly in Chapter 2-6. The conclusion and future work are presented in the end. The structure of the thesis is given below:

1. Chapter 1 discusses the background, motivation, aims and objectives of the reported research.
2. Chapter 2 presents a thorough review on hard and soft robots with the emphasis on medical applications and human-safe industry. This chapter investigates application need and current state of the art of controllable stiffness robots. This process will shed light on the advantages and limitations associated with current robotic technology, and identify research gaps to be explored in this thesis.
3. Chapter 3 introduces the experimental characterisation of materials used in this research, including smart materials for designing controllable stiffness elements and silicone materials for the fabrication of the soft structures.
4. Chapter 4 presents the design and analysis of the single module for the modular manipulator. Mechanical models of the bonding torque are developed and FEA simulations are conducted on the single modules to estimate the bending stiffness. Thermal models are introduced in the end.
5. Chapter 5 highlights the fabrication method of the single module. Application method of the low melting point solder and hot-melt adhesive are discussed.
6. Chapter 6 presents the experimental characterisation of the single module. The prototypes of each design are presented with performance analysis, with the emphasis on the stiffness change and the response time.
7. Chapter 7 discusses the results from the experimental studies. The advantages and limitations of each design are presented. The recommendations of the future research are presented in the end.

Figure 1.1 presents a visual representation of the thesis structure.

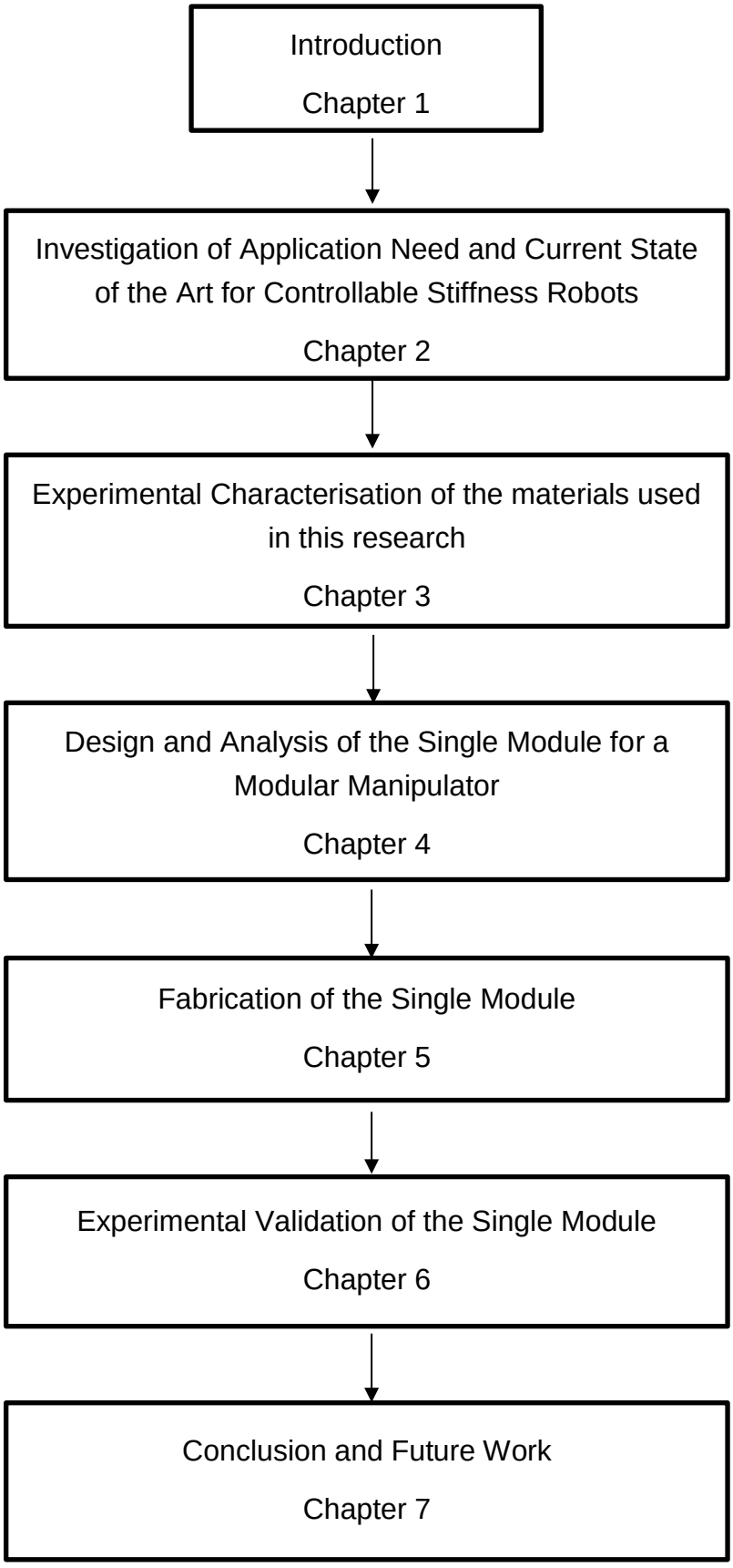

Figure 1.1 Graphical design of thesis structure.

Chapter 2
Literature Review

The chapter presents a thorough review on hard and soft robots with the emphasis on medical applications and human-safe industry. This process will shed light on the advantages and limitations associated with current robotic technology, and identify the research gaps to be explored in this thesis.

2.1 Introduction

Snake-like manipulators are formed from large numbers of serially configured joints that allow the manipulator body to follow complex paths, with appearance similar to a biological snake. These manipulators are well suited for operation in restricted and confined environments where the manipulator body can bend around obstacles to place an end effector at a difficult to access location.

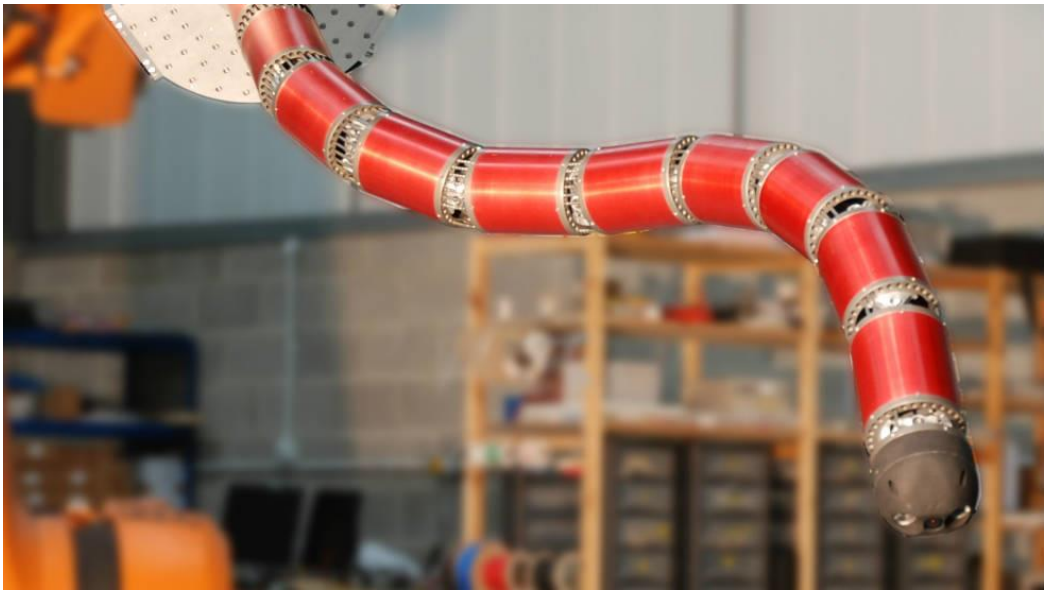

Figure 2.1 Snake-like manipulator from OC Robotics [20].

In general, snake-like manipulators can be categorised into hard manipulators and soft manipulators on the basis of their underlying materials [4], as shown in Figure 2.2. Hard manipulators are composed of rigid components, such as joints and links. In comparison to hard manipulators, soft manipulators are constructed with soft and deformable materials. Soft manipulators can actively interact with the environment without causing damage, which makes them ideal for medical applications and human-safe industry.

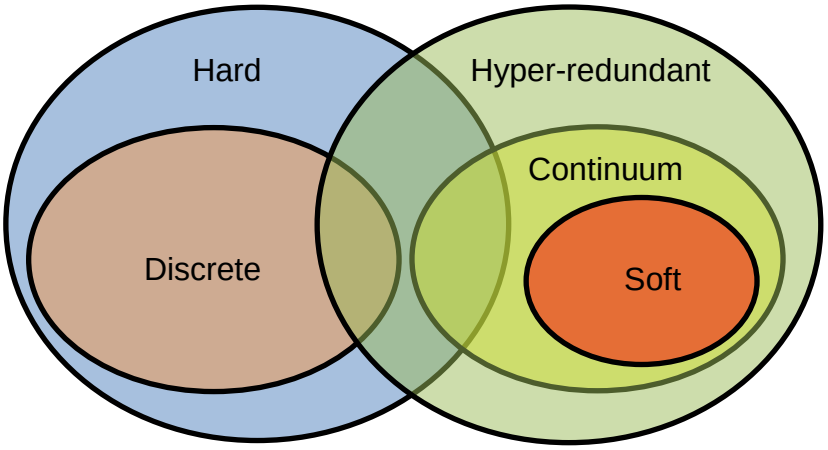

Figure 2.2 Classification of Snake-like manipulators on the basis of materials and degree of freedom [4].

2.2 Hard Manipulators

2.2.1 Discrete Hyper-Redundant Manipulators

Hard hyper-redundant manipulator can be further classified as hyper-redundant discrete manipulator and continuum manipulator. Hyper-redundant discrete manipulator combines short rigid links with a large number of joints. This creates highly dexterous mechanisms which appear to produce a snake-like curve. Shang *et al.* [21] developed a snake-like robot, namely i-Snake® robot, for Natural Orifice Transluminal Endoscopic Surgery procedure. The main novelty of the device is the modular unit design based on a hybrid actuation scheme (tendon and motor driven) which allows independent control of each rotation DOF while leaving sufficient space for internal channels within the links. Three internal channels of diameters 3mm, 3mm and 1.8mm are available for passing visualisation, interventional instrumentation, and control lines. Although it is impressive to design and manufacture articulated joints in small dimension, the inherent advantage (independent actuation of each joint) also increases the complexity of the control. The model of the articulated joint is shown in Figure 2.3.

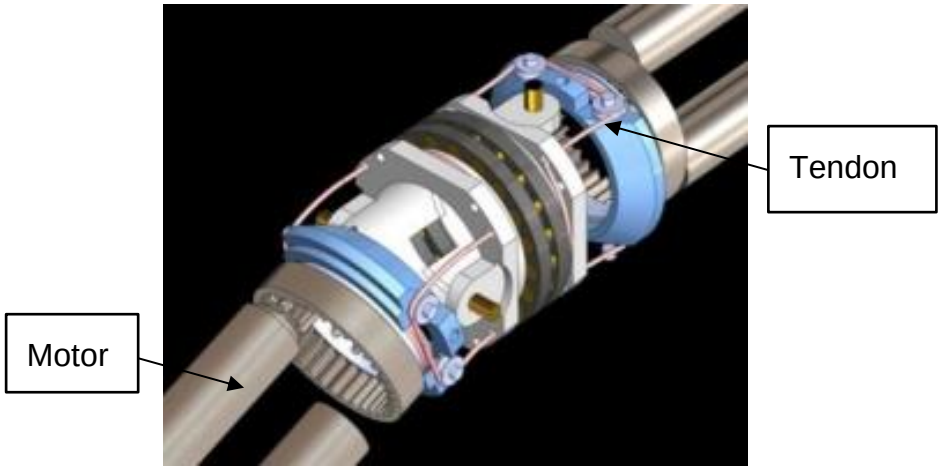

Figure 2.3 3D model of i-Snake articulated joint [21].

Kwok *et al*. [22] developed an articulated snake-like manipulator that consisted of universal joints and a series of identical links. Figure 2.4 illustrates the structure of snake-like manipulator prototype. Two micromotors are embedded in each link. The links are connected by universal joints, each providing two degrees of freedom. The advantage of this design is the independent actuation of each joint. However, it also increases the complexity of the control.

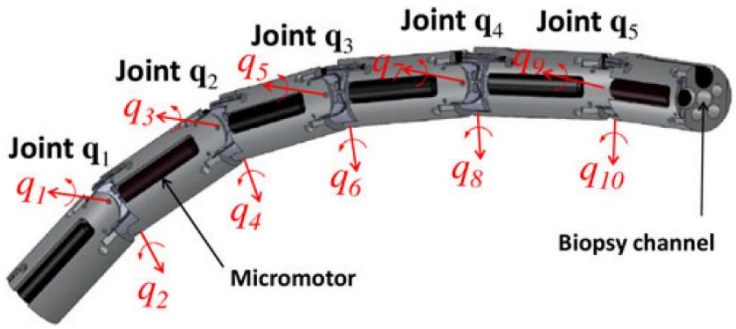

Figure 2.4 Schematic illustration of the robot showing the articulated joint structure [22]

A highly articulated robotic probe (HARP) (see Figure 2.5) that can exploit its snake-like structure to navigate in a confined environment while minimally interacting with the environment along the path was developed at Carnegie Mellon University [8] [7]. The major contribution of HARP design is the stiffness control: two concentric tubes are used to construct the HARP, and each tube can alternate between rigid and passive states. These tubes consist of rigid cylindrical links strung together by four cables, three for the outer tube and the remaining for the inner tube. When the cables are pulled toward the back of the outer tube, the links are pulled toward each other increasing friction between the links eventually causing the mechanism to become rigid [7]; when they are relaxed, the outer tube becomes limp. Hence the control of the

orientation is provided by the outer tube, and the inner tube is used to maintain the previous configuration. This feature leads to the ability to follow a curve in a three-dimensional confined environment. In comparison to the i-Snake robot, HARP is easier to control.

Figure 2.5 Highly articulated robotic probe prototype [7].

A hyper-redundant multiple degrees of freedom (DOF) active surgical forceps instrument that enables more advanced and extensive laparoscopic surgery was developed by Ikuta *et al*. [23]. The device, as shown in Figure 2.6, features decoupled ring joint mechanism that allows 2 DOFs rotation, compensation mechanism for cable elongation, and detachable gripper mechanism. The advantage of this design lies in the design of compensation mechanism. One of the major challenges in the cable-driven system is the cable elongation that causes by repeated stress. The compensation mechanism that consists of friction bar, coil spring and tension pulley was adopted to solve the problem by maintaining the constant route length of the cable.

Figure 2.6 Hyper redundant multiple DOFs active surgical forceps instrument [23].

Ishii *et al.* [24] [25] [26] designed a robotic forceps manipulator, as shown in Figure 2.7, for minimally invasive surgery. The novelty of this system is the developed screw-driven mechanism, termed double-screw-drive (DSD) mechanism. This enables omnidirectional bending motion by rotating two linkages consisted of a right-handed screw, universal joint, and a left-handed screw [24]. The manipulator has high rigidity, which would guarantee the accuracy of the movement. However, the inherent advantage of this design also creates difficulty for the manipulator to adapt to the working environment. It could potentially damage the tissue or internal organ.

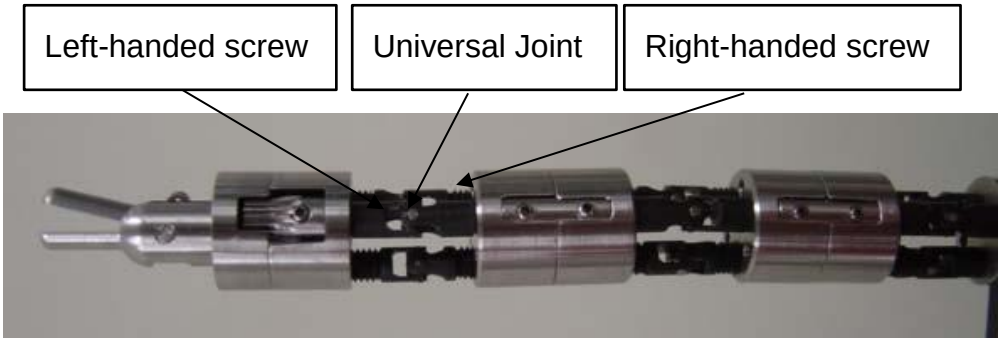

Figure 2.7 Prototype of DSD forceps manipulator [24].

2.2.2 Continuum Manipulators

In addition to the joint-type robots, there exists a type of robot that features a continuous backbone. This kind of robot, termed continuum robot, has no motioned joints, but it can realise the motion and manipulation with the help of its continuous flexible distortion [27]. Continuum robots can bend at any point along their structures, which improves their obstacle-avoiding capability when compared to joint type manipulators. Table 2.1 provides the overview of continuum manipulators describing their advantages and disadvantages.

Table 2.1 Review of Design Method for Hard Continuum Manipulator. Five design methods are reviewed in this section, and their advantages and disadvantages are listed in the table.

Design Method	Examples	Advantages	Disadvantages
Wire-Driven Spring Backbone	[28] [29]	• Spring backbone provides natural compliance	• Difficult to control
Wire-Driven Incompressible Backbone	[30] [31] [6] [32]	• Highly dexterous • More predictable behaviour	• Unable to extend or contract

	[33] [34] [35] [36]		
Screw-Driven Flexible Backbone	[37]	• Highly compliant and flexible	• Bulky and difficult for minimization
Flexure Joints	[38] [39] [40] [41]	• Simple design and easy to control	• Suffer from low repetition
Concentric Tube Backbone	[42] [43] [44] [45] [46]	• Simple and thin design • High compliance	• The need for external actuator • Lack of actively controlled bending

The Tendril robot developed by NASA's Johnson Space Centre, finds its inspiration in the biology of snakes, tentacles, and climbing plants [28]. The Tendril's backbone, as illustrated in Figure 2.8, is constructed by a series of extension and compression springs that are joined together by threaded links. The active bending is actuated by sets of antagonistic tendons that are attached to specific links, run the entire length of the backbone, and are terminated at pulleys inside the body housing structure. The spring backbone provides natural compliance. However, this also makes the design difficult to control, as control effort intended for backbone bending is lost in compression [27].

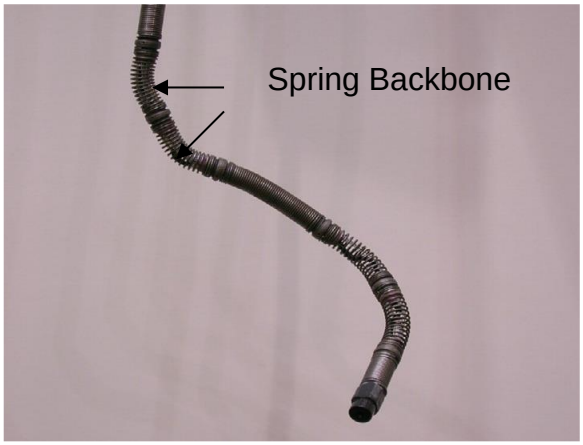

Figure 2.8 Tendril robot [28].

Hu *et al*. [29] proposed a snake-like robotic manipulator that features continuously deformable backbone. This device (see Figure 2.9) consists of five sections, and each is composed of universal joints, rivet, spring tube, drive cable and metal mesh. The novelty of this system is the implementation of the spring tube. It not only guides the cables properly along the manipulator but also bears the axial force produced by bending motion. Four cables located 90 degrees apart and divided into two pairs are used to provide 2 DOFs actuation for each section. Although the manipulator is highly compliant, it is difficult to control.

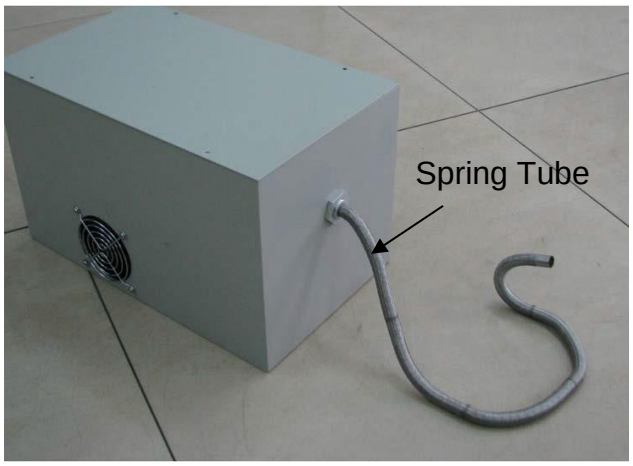

Figure 2.9 Snake-like continuum manipulator with continuously deformable backbone [29]

A simple solution to the above-mentioned problems is to replace spring backbone with a flexible incompressible rod. Gravagne *et al*. [30] developed a planar continuum robot, as illustrated in Figure 2.10, under such concept. The manipulator is composed of two sections, each with two degrees of freedom. Its central backbone is a thin elastic beam, with four cables running through the guiding holes. Two cables terminate at the midpoint, the rest two at the endpoint. The advantages of this design include large deflection and more predictable behaviour. The limitation is that this approach excludes the use of incompressible backbone, which means the manipulator is unable to contract or extend.

Figure 2.10 Continuum snake-like manipulator with incompressible flexible backbone [30]

Although incompressible backbone approach has its limitation, it has been proven to be popular and successful. In particular, Zhao *et al.* [31] proposed a Hook Joint type continuum robot, as shown in Figure 2.11, based on this approach. The external section of the device is serialised by multiple segments of parallel springs while the internal section is the backbone with multiple Hook Joints connected. External and internal sections are connected by circular thin slices. The manipulator is actuated by four cables, with every two cables forming one pair of antagonistic cables.

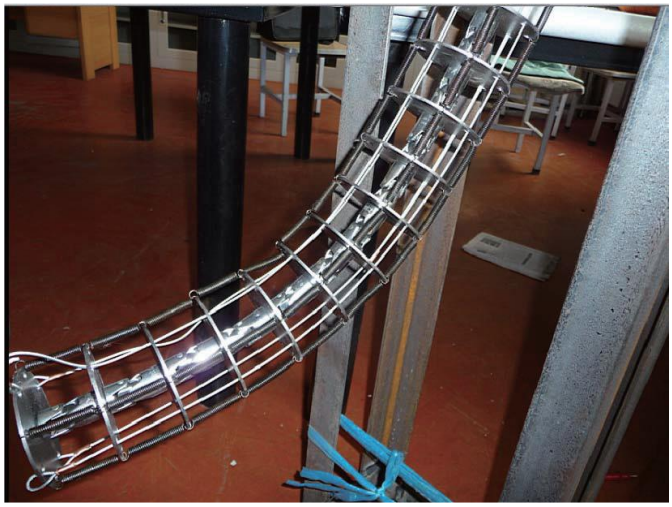

Figure 2.11 Hook Joint type continuum robot [31].

Simaan *et al.* [6] [32] [33] developed an integrated system equipped with Distal Dexterity Units (DDU) for MIS of the throat and upper airway (see Figure 2.12). Each DDU is composed of a multi-backbone snake-like unit and a detachable parallel unit attached at its tip. The snake-like unit consists of a base disk, an end disk, several spacer disks, and four super-elastic NiTi tubes. The novelty that separates DDU from other snake-like unit is the implementation of four super-elastic NiTi tubes, thus removing the dependency on small universal joints and wires. These tubes are considered as the backbones of the snake-

like unit. The central tube is the primary backbone that attached to both the base and end disks while the remaining three are the secondary backbones that attached only to the end disk and used for realizing the push-pull modes. The detachable parallel unit is capable for not only answering the need for tool detachability but also providing additional three DOFs for distal dexterity. The first prototype of a snake-like unit is shown in Figure 2.11. However, the limitation of this prototype is that it can only be bent to a continuous curve, which limits its application, especially in a space-constrained environment.

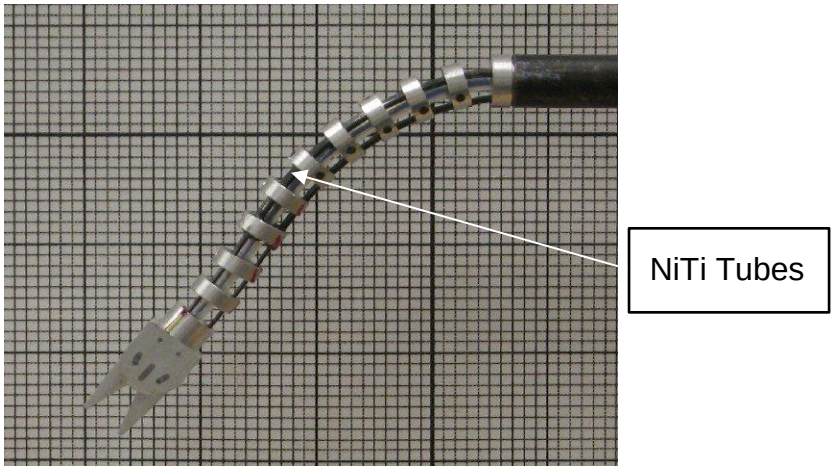

Figure 2.12 Distal Dexterity Units [32].

Insertable Robotic End-effector Platform (IREP) by Ding *et al.* [34] addresses the need for self-deploying robots that provide sufficient dexterity in single entry point, while seamlessly supporting stereo vision feedback during surgical operation procedure. This system consists of two dexterous arms and a 3 DOFs (pan, tilt and zoom) visualisation module (see Figure 2.13). Each arm comprises a 5 DOFs continuum snake-like robot, a 2 DOFs parallelogram mechanism that can deploy each continuum robot, a wire-driven distal wrist, and a gripper. It acts as a surgical tele-operated slave for bimanual manipulation. The snake-like robot is based on the work done by Simaan *et al.*[6], where a multi-backbone design is implemented for the snake-like robotic unit. The novelty of robotic slave is the integration of parallel mechanisms and snake-like continuum robots, providing the deployable mechanical architecture and enhanced dexterity to the system. However, the actuation unit that includes 21 actuators and several sub-modules causes cumbersome footprint in theatre.

Figure 2.13 IREP robot [34].

Li *et al*. [36] developed a multi-section wire-driven manipulator for minimally invasive surgery. The manipulator, as shown in Figure 2.14, comprises an elastic backbone and a number of spherical joints. Wires are going through the pilot holes and are fastened at the end of each section. Therefore, each section can be controlled independently, and basic shapes, such as “S” and “C”, can be achieved. The elastic backbone is used to constrain spherical joints bending and to minimise the side effects of friction. The disadvantage of this design is that in order to increase the dexterity of the manipulator, more sections and cables are required.

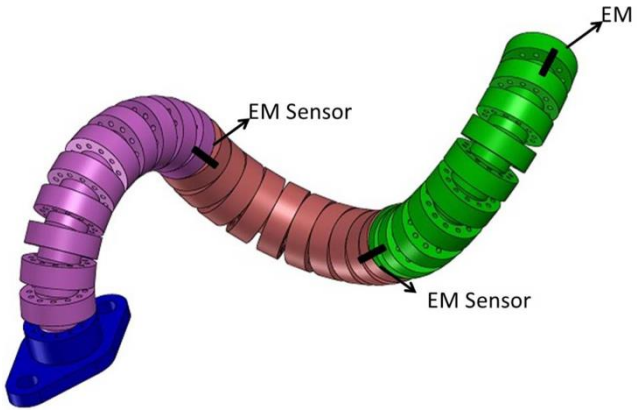

Figure 2.14 Multi-section wire-driven flexible robot [36].

Trunk-like manipulators have been studied by researchers as a form of hyper-redundant continuum manipulator. Hannan *et al*. [35] [47] developed a four-section elephant trunk manipulator (see Figure 2.15). Each section consists of four joints and is actuated by a hybrid cable and spring servo system. Although the system is highly dextrous (total of 32 degrees of freedom), it requires a large footprint.

Figure 2.15 Elephant trunk manipulator [35].

Yang *et al*. [37] proposed a novel trunk-like continuum manipulator, named ET arm. The manipulator, as shown in Figure 2.16, is composed of two sections. Each segment consists of elastic skeletons, artificial skin, and three artificial muscles. The novel artificial muscle includes a base, an actuator, couplings, a flexible rod and an end disk. Unlike traditional pneumatic muscle, the artificial muscle in this design adopts low-cost flexible rod and screw drive to create the shortening and extension of the muscle. The manipulator is flexible and highly compliant, it can be used in human-safe industry.

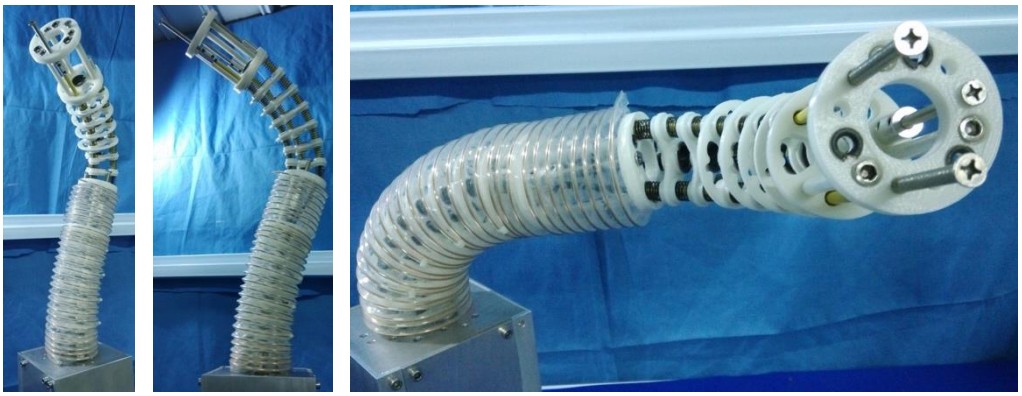

Figure 2.16 ET arm and its bending experiments [37].

Compliant mechanisms, such as flexure linkages, have been used to design simple and lightweight continuum manipulators. Successful examples include Binary Robotic Articulated Intelligent Device (BRAID) [38] [39], cable-driven dexterous manipulator for minimally invasive surgery [40], and endoscopic manipulator from Peirs *et al*. [41]. As shown in Figure 2.17, BRAID is composed of a series of parallel linkage stages. Each stage has three flexure joints, and each with shape memory alloy (SMA) binary actuators. The advantages of this design include lightweight, dexterity and deployability. The manipulator can be deployed as a continuum manipulator and collapse to a small stowed volume.

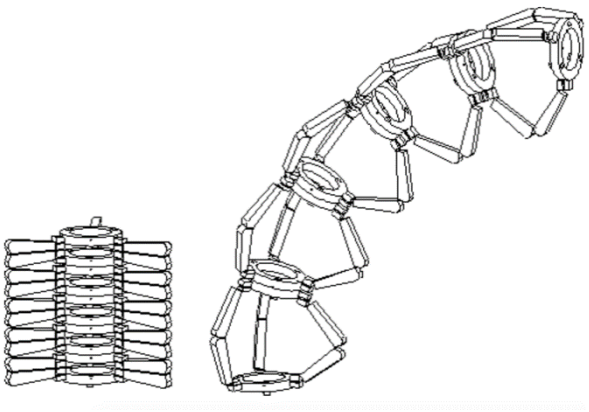

Figure 2.17 Basic element of BRAID [38].

Segreti *et al*. [40] developed a snake-like manipulator for the surgical removal of osteolysis behind total hip arthroplasties. As shown in Figure 2.18, the manipulator is constructed with of two Teflon tubes with alternating slots cut on each side. There are fourteen slots cut on each side, resulting in 27 flexure joints. Two cables are used to actuate the manipulator; thus, the binary bending can be achieved.

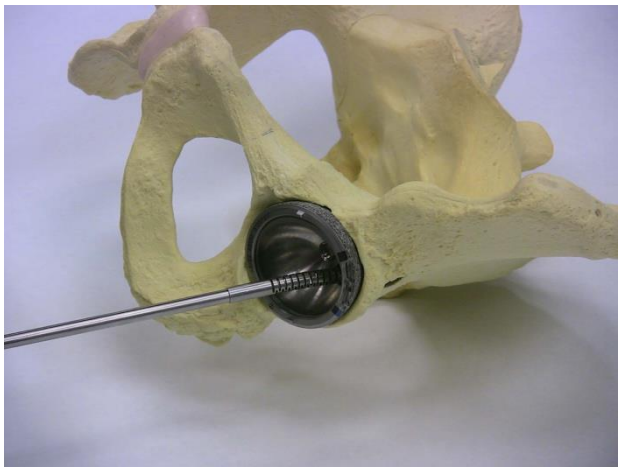

Figure 2.18 Compliant surgical manipulator [40].

Peirs *et al*. [41] developed an endoscopic manipulator with 2 DOFs. The flexible manipulator consists of a super-elastic NiTi tube which can be bent through four cables. The four cables are fixed at the tip and form two antagonistic pairs. Each antagonistic pair control one DOF. The tube is cut into a structure consisting of a series of rings connected by thin elastic joints to enhance the bending flexibility. The prototype of the device is shown in Figure 2.19. Although the flexure-based design is inherently simple and easy to control, lack of active control of individual section could limit the potential in medical applications.

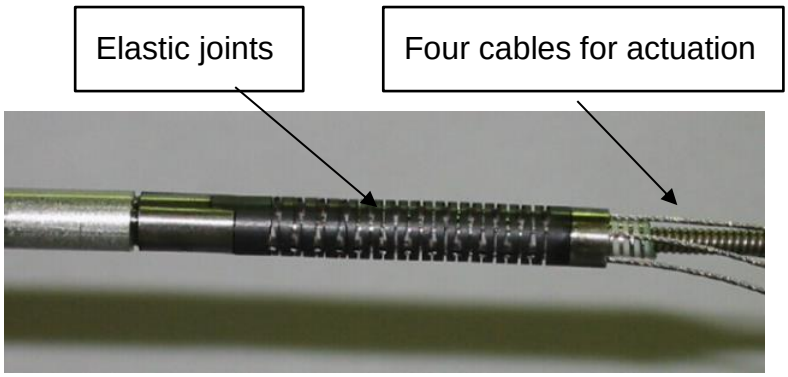

Figure 2.19 Endoscopic manipulator [41].

Another form of continuum manipulator design is based on a backbone formed by concentric tubes. The tubes are free to rotate and translate with respect to each other, as illustrated in Figure 2.20. This feature thus achieves both torsion and extension. Lock *et al*. [42] used pre-curved elastic tubes to construct a continuum manipulator. Advantages of concentric tube robots include inherently clean and thin design, which makes them ideal for medical applications. It offers a good compromise between stiffness and shape control. The concentric tube robot can be constructed with the diameter comparable to catheters, and lengths sufficient enough to reach operation target. Disadvantage includes the lack of actively controlled bending since the curvature of the tube is predetermined.

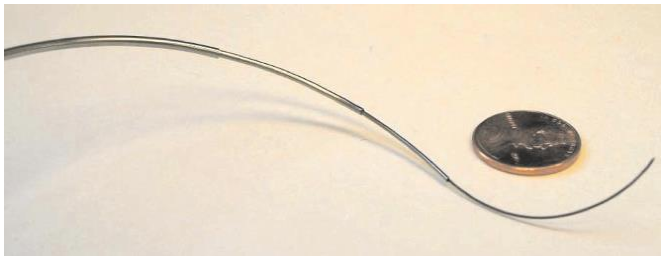

Figure 2.20 Concentric tube robot comprised of four telescoping sections that can be rotated and translated with respect to each other [42]

Webster III *et al*. [43] [44] developed an “active cannula” that consisted of three pre-curved nitinol tubes (see Figure 2.21). Su *et al*. [45] proposed an MRI-guided, piezoelectrically actuated concentric tube robot for percutaneous interventions and stereotactic surgery. The proposed robots are unique in their use of backbone to transmit bending force. Unlike wire-driven or pneumatic controlled continuum robot, the bending forces are applied through external mechanisms, such as wires or pneumatic muscles. These external mechanisms are advantageous in terms of providing actively controlled curvature; however, they also limit miniaturisation.

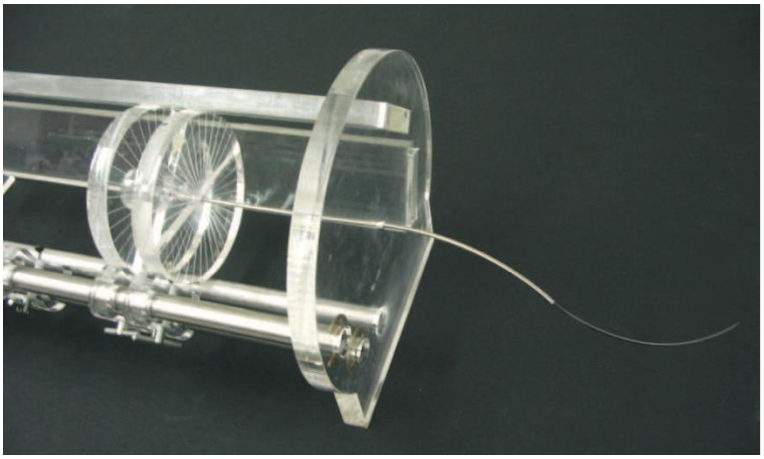

Figure 2.21 Concentric tube robot [44].

A robot with snake-like configuration was proposed by Mahvash *et al*. [46] for the use of Laparoscopic Single-site Surgery procedure recently. This hybrid snake-like robot, as shown in Figure 2.22, is composed of a robotic probe and a set of pre-curved NiTi tubes. Two pre-curved tubes with the same length, initial curve, bending stiffness, and different diameters are selected so that they can be inserted inside each other and the combination can be introduced into the port of robotic probe. It can provide both tip dexterity and stiffness required for operational tasks.

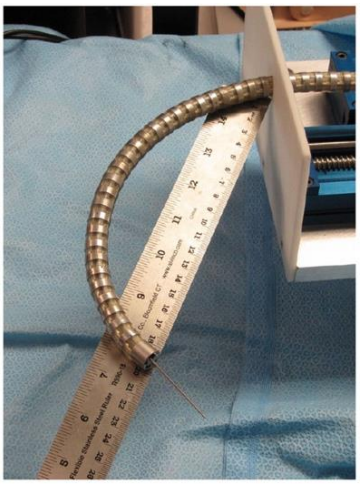

Figure 2.22 Hybrid snake-like robot [46].

2.3 Soft Manipulators

Researchers have always found in biology an inexhaustible source of inspiration for devices and machines [4] [3]. Studying how animals exploit soft materials to move in unpredictable environments can draw inspiration on emerging robotic technology in the medical application and human-safe industry. In this section, fundamentally soft and highly deformable robotic

manipulators are reviewed, as listed in Table 2.2. Soft manipulators are classified by their design methods, and the advantages and disadvantages are presented.

Table 2.2 Review of Design Method for Soft Manipulators. Four design methods are listed in the table, as well as their advantages and disadvantages.

Design Method	Examples	Advantages	Disadvantages
Tendon-Driven Octopus-Like Manipulator	[48] [49] [50] [51]	• Simple design • Easy to control	• Limited force • The need for external actuators
SMA Actuated Octopus-Like Manipulator	[52]	• Simple design • Easy to control	• Limited force
Pneumatic Actuated Trunk-Like Manipulator	[53] [54] [55]	• Actively controlled bending • Highly dexterous	• Bulky design • The need for pressure regulation • Low force generation capability
Other	[56]	• Independent control of robotic sections	• Low force performance • 2D Planar operation

Muscular hydrostats such as elephant trunks and octopus arms represent paradigmatic soft structures that can bend, extend and twist [3]. These capabilities have inspired robotic engineers to incorporate soft technology into their designs. One successful example that applied muscular hydrostats to robotic design is the soft robotic octopus arm.

Renda *et al.* [48] [49] developed a tendon-driven continuum manipulator (see Figure 2.23 and Figure 2.34) inspired by octopus arm, as well as a general steady-state theoretical model. Both manipulator and actuators were modelled. The model can be used for simulating many kinds of soft body continuum manipulators actuated by cables. According to the authors, the

developed approach is fast enough to be implemented in the embedded control of the manipulator. The manipulator is constructed by a single conical piece of silicone actuated by cables embedded in the body. Four cables are anchored at different distances between from the end through a rigid plastic disc built in the robotic arm. Thus, the manipulator can be bent and twisted by pulling the cables. The advantage of this design lies in its simplicity and being able to adapt to working environments; however, the inherent advantage comes with limited force.

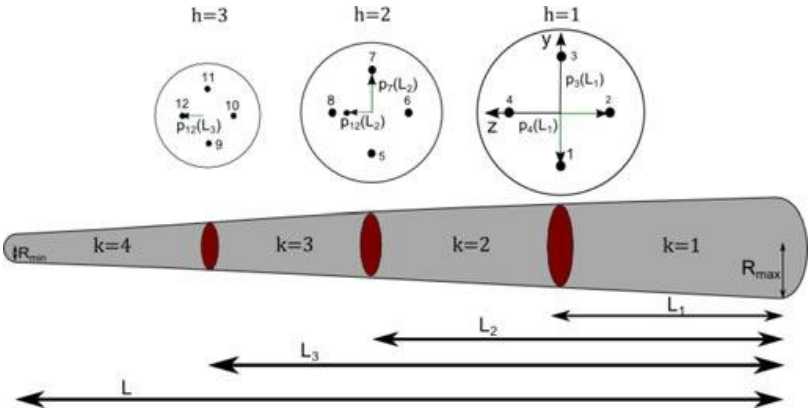

Figure 2.23 Illustration of the design of a tendon-driven octopus arm [49].

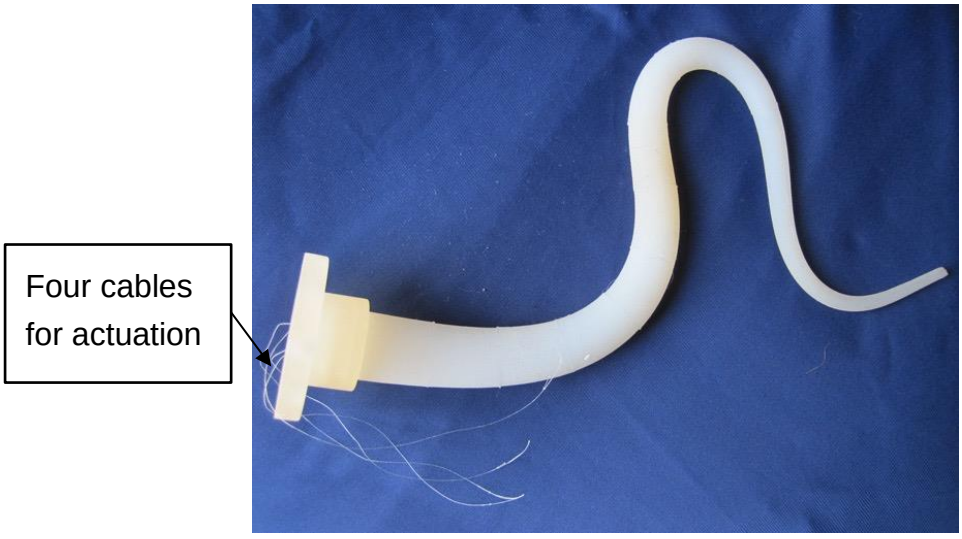

Figure 2.24 Tendon-driven soft continuum manipulator inspired by octopus arm [49].

Wang *et al*. [50] developed a cable-driven soft robotic manipulator inspired by octopus tentacle. As shown in Figure 2.25, it is made of silicone rubber and has no rigid structure inside. The soft manipulator is cone-shaped and actuated by four cables running through the structure. Since the manipulator has no rigid components, its safety and dexterity make it suitable for the medical application. However, this manipulator lacks the ability to module stiffness, which makes it difficult to operate in certain tasks.

Figure 2.25 Cable-driven soft robotic manipulator [50].

Cianchetti *et al*. [51] presented the design of an artificial muscular hydrostat for developing an octopus-like robot. The proposed robotic arm has octopus arm feature, such as the ability to elongate, to bend in all directions, and to control its stiffness. As shown in Figure 2.26, the robotic arm demonstrates the capacity to bend. The bending point is not predetermined, but automatically created thanks to the interaction of the object. Longitudinal muscles, transverse muscles and their reciprocal actions were taken into consideration in artificial muscular hydrostat design. The robotic arm consists of four longitudinal muscles and a number of transverse muscles in parallel. One of many advantages of this design is the ability to modulate stiffness. A series of small rigid components were embedded in the soft body. The longitudinal and transverse muscle groups act in an antagonistic way causing stiffness.

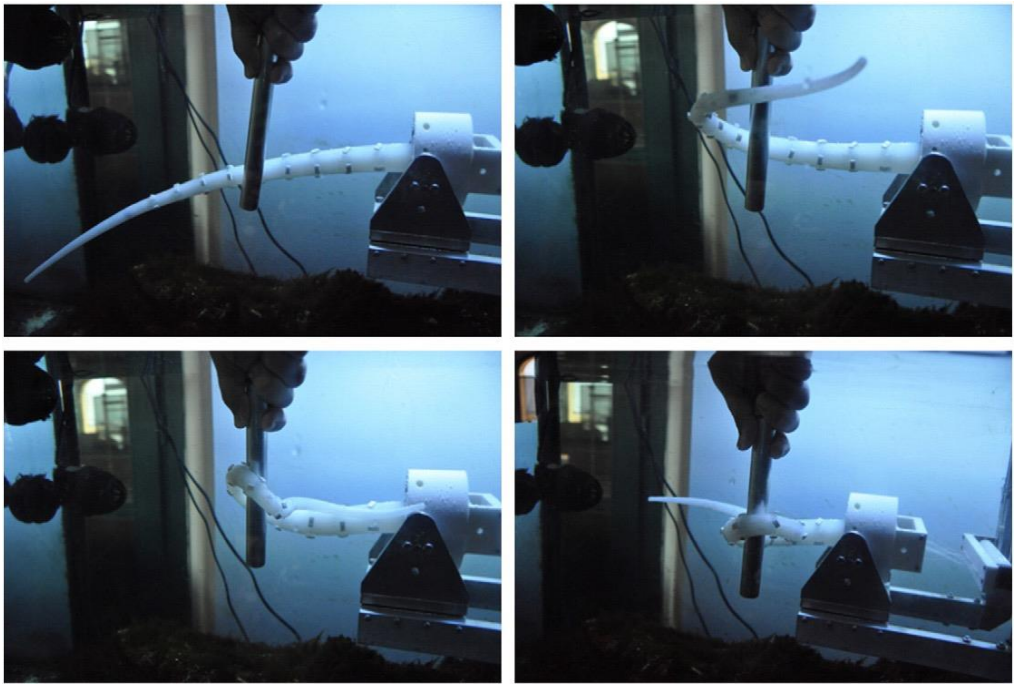

Figure 2.26 Octopus-like robotic arm in grasping action [51].

As shown in Figure 2.27, robotic octopus arm is developed by Cianchetti *et al.* [52]. It is completely soft and compliant when relaxed, but it is able to replicate the basic mechanism of the octopus's muscular hydrostat when activated. It can elongate, shorten and bend in all directions at any point along the arm. The robotic arm consists of longitudinal and transverse elements, and external structure allowing large deformations and at the same time keeping the global shape, a very thin and elastic skin, and a sinusoidal arrangement of internal fibres. This work demonstrated an example of biomimetic with an efficient translation of biology into robotics and provided the possibilities of adapting soft robotics to manipulator designs in medical applications.

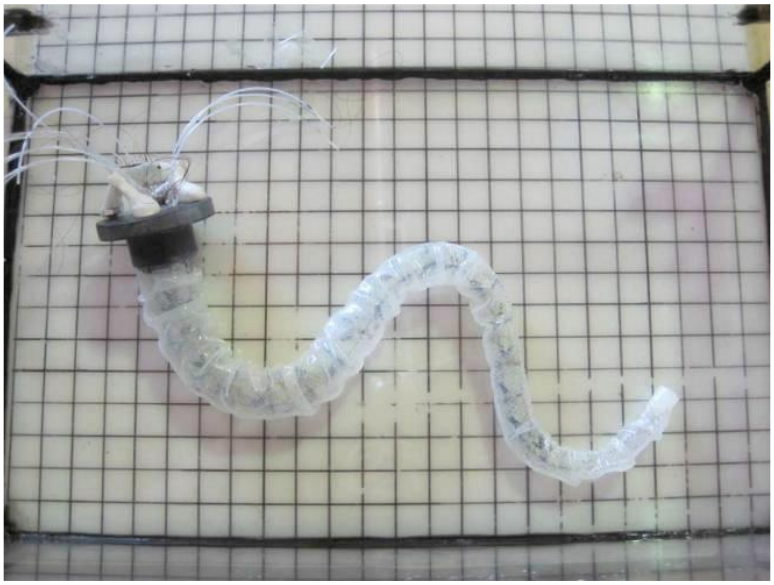

Figure 2.27 Robotic Octopus Arm composed by a braided sheath and actuated by SMA springs [52]

The incorporation of pneumatic actuation is another design approach for soft continuum manipulator. The backbone of continuum manipulator can be constructed from pneumatic actuators. Thus, a series of independently controlled sections is created. The torsion, extension and contraction can be realised by applying different pressure in various sections. Successful example includes OctArm continuum manipulator from Bartow *et al*. [27] [53]. As shown in Figure 2.28, the OctArm manipulator is inspired by biological trunks. It features three independent actuated sections. Each section is actuated by pneumatic muscles. The advantage of this design includes actively controlled the backbone, which is not provided by concentric tube design. However, the disadvantages of this design include low force generation capability, the requirement of pressure regulation equipment, and large footprint, which limit its potential in medical applications.

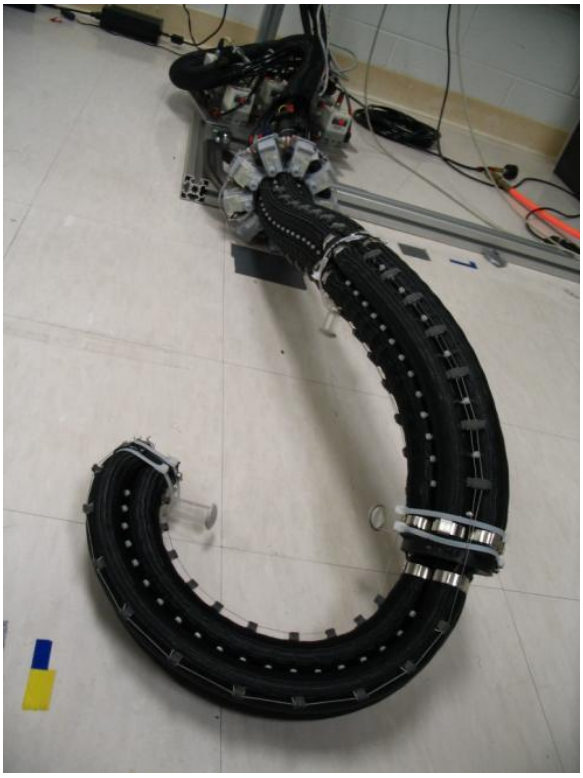

Figure 2.28 OctArm continuum manipulator [53].

An elephant trunk-like manipulator, as shown in Figure 2.29, developed by Tsukagoshi *et al*. [54] consisting of a spiral tube wound around the manipulator backbone like a coil. The novelty of this manipulator is the design of the spine. The spine of the manipulator installed in its centre aims to help the unit to be shrunk passively when the opposite side is stretched. The spine structure is composed of several blocks. Wire combination mechanism is used to connect blocks.

Figure 2.29 Bending action of Active Hose [54].

Pritts *et al.* [55] developed a soft trunk-like manipulator with two sections that each provide two-axis bending and extension. Kang *et al.* [57] developed a pneumatically actuated continuum manipulator with six sections that can

elongate, shorten, and bend at any point along the arm length. As shown in Figure 2.30, each segment is supported and actuated by four pneumatic artificial muscle that is mounted on the connection plate. Although pneumatic actuation designs are highly dexterous, they suffer from a number of shortcomings to restrict in medical applications. They need a bulky air compressor for continuous operation, which restricts mobility and makes minimization difficult.

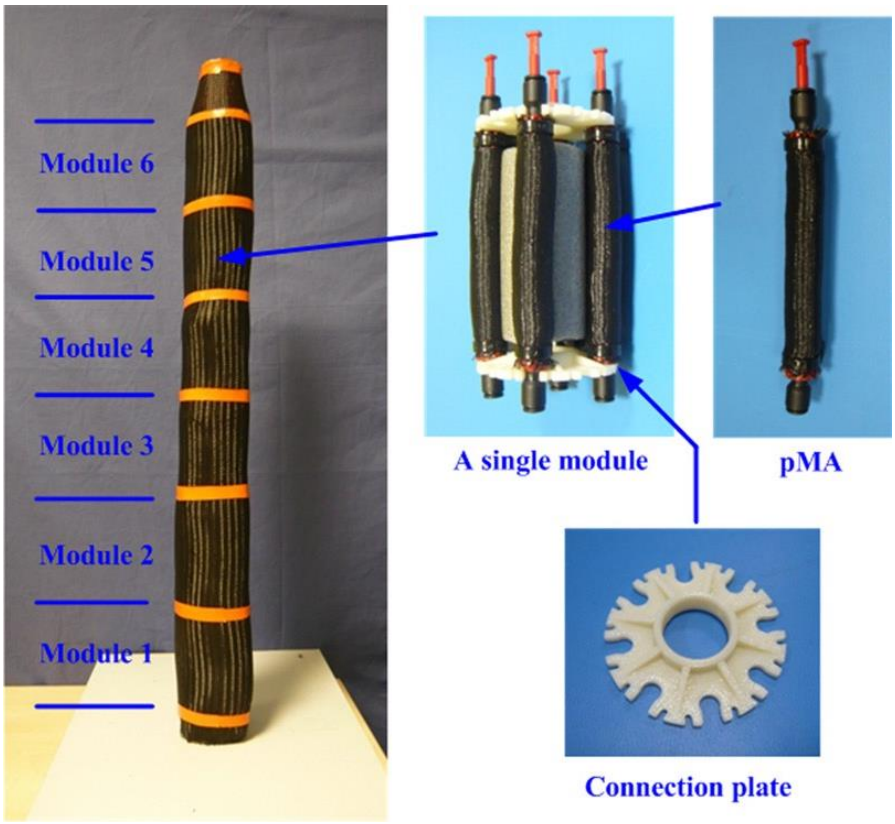

Figure 2.30 Pneumatically actuated continuum manipulator [57].

The soft grasping manipulator shown in Figure 2.31 has six bidirectional sections with cylindrical cavities and combined with a soft gripper [56]. The planar arm has seven degrees of freedom and is made of soft rubber. The planar manipulator is capable of pick-and-place operations. The advantage of this design includes independent pneumatic control of robotic grasper since the manipulator is composed of 13 custom cylindrical segments. However, the manipulator is only able to perform under low payloads and limited to a 2D planar motion.

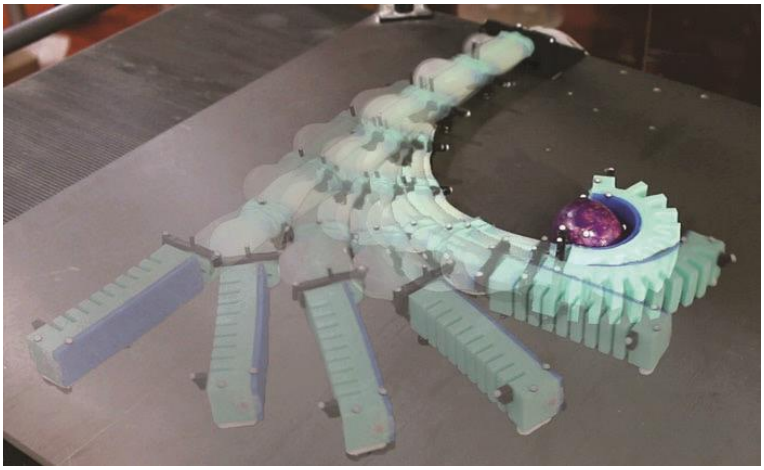

Figure 2.31 Soft grasping manipulator [56].

2.4 Controllable Stiffness Robots

The need for building robots with the capability of stiffness modulation has emerged recently. Stiffness modulation is the way for hard and soft robots to interact with the working environment effectively [9]. Softness enables dexterity and prevents the damage to the environment, whereas rigidity can transfer the forces to the environment when required. Therefore, this type of robot is particularly suitable for medical applications and human-safe industry. In this section, variable robotic platforms with capabilities of stiffness modulation are reviewed. As listed in Table 2.3, controllable stiffness robots are classified by design methods. Five design methods, i.e. antagonistic principle, friction, electro- and magneto- rheological materials, thermorheological materials, and granular materials, are presented in the table, along with their working principles.

Table 2.3 Review of design method for controllable stiffness robots. Five design methods are listed in the table, along with their working principles.

Design Method	Examples	Working Principle
Antagonistic principle	• [51] [58]	• The longitudinal and transverse muscle groups can act in an antagonistic way causing stiffness modulation.
Friction	• ShapeLock TSG HARP	• Links are pulled toward each other increasing friction between the links eventually

	• Layer Jamming Scale Jamming • Granular Jamming	causing the mechanism to become rigid. • The mechanism is composed of multiple layers of thin film, and makes use of amplified friction between the films by applying vacuum pressure. • By applying vacuum pressure, the material can transition between solid-like state and fluid-like state.
Electro- and magneto- rheological materials	• ER fluids • MR fluids	• When subjected to an external magnetic or electric field, the ER or MR particles orient and build chains in response to the particles interaction. This translates into an increased resistance to deformation [9].
Thermorheological materials	• Solder • Low melting point alloy	• Materials feature a low melting point, in which a phase change can be rapidly and reversibly obtained by thermal input

2.4.1 Antagonistic Principle-based Controllable Stiffness Robots

Variable stiffness soft robot can be achieved based on antagonistic principle. Successful examples include octopus-like robotic arm developed by Cianchetti *et al.* [51] (as reviewed in Section 2.3, the longitudinal and transverse muscle groups can act in an antagonistic way causing stiffness modulation) and a soft manipulator based on tendon-driven coupled with pneumatic-driven actuation method developed by Stilli *et al*. [58]. The proposed manipulator is composed of modules that are constructed of an internal stretchable latex bladder integrated with an outer, non-stretchable polyester fabric sleeve. Tendons connected to the distal ends of the robot modules run along the outer sleeve allowing each module to bend. As shown in Figure 2.32, the hybrid driven manipulator can modulate the stiffness by inflating the stretchable bladder and tightening the tendons at the same time.

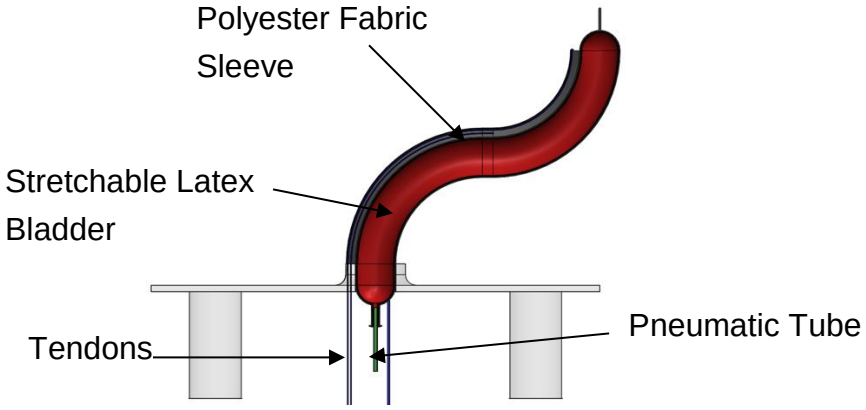

Figure 2.32 CAD drawing of a hybrid actuation scheme manipulator [58].

2.4.2 Friction-based Controllable Stiffness Robots

The friction-based method is one of the simplest ways to realise controllable stiffness for hard robots. Wires are usually used to initiate the stiffening process. When the wires are pulled toward the back, the links are pulled toward each other increasing friction between the links eventually causing the mechanism to become rigid. Successful examples include a highly articulated robotic probe (HARP) [8] [7], commercially available ShapeLock technology [59] and Tension Stiffening Guide-wire (TSG) [60]. ShapeLock technology is achieved by a series of titanium rings connected by wires, and rings lock into a set position when the connecting wires are tightened. The stiffened over-sheath allows better force transmission when compared to fully flexible platforms. Figure 2.33 shows USGI Medical's ShapeLock Endoscopic Guide and Cobra instruments.

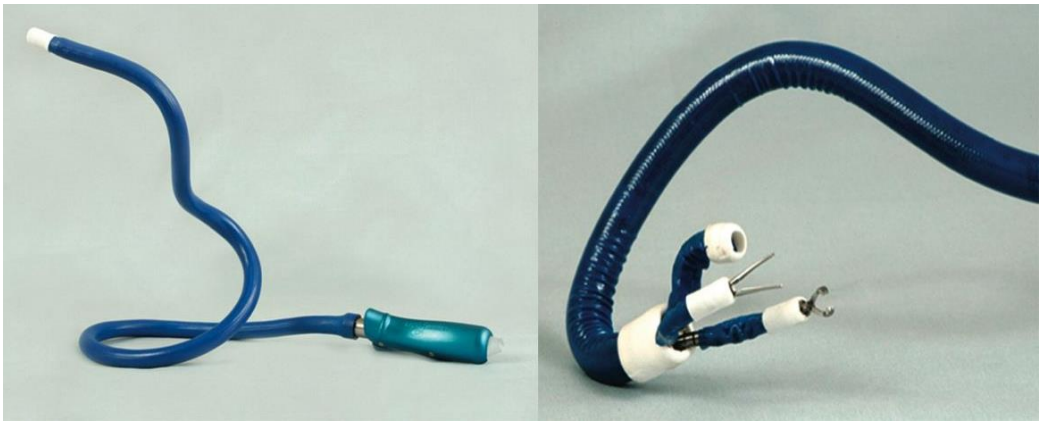

Figure 2.33 USGI Medical's ShapeLock Endoscopic Guide and ShapeLock Cobra [59]

A catheter positioning system sharing similar design concept with the HARP was proposed by Chen *et al.* [60]. This system, named Tension Stiffening Guide-wire (TSG), is capable of manoeuvring a catheter through extravascular spaces with an arbitrarily defined number of turns. It consists of

two different custom designed “guide-wires” that are made of a series of modular beads. The catheter sheath is then developed to encase the two strands of controllable stiffness guide-wires. One guide-wire has a body that can be stiffened and a distal end that can be steerable while the remaining one can only be stiffened or made flexible. Friction between different modular beads is used to stiffen the guide-wire. During the operation, two guide-wires are used in tandem: one guide-wire remains stiff while the other is kept flexible. The flexible one uses the stiff one as a reference track to move forward. Figure 2.34 shows the prototype of TSG system.

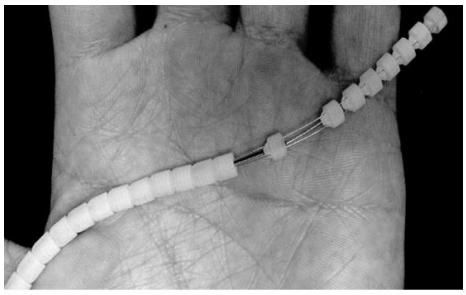

Figure 2.34 Tension-stiffening guide wire prototype [60].

Recent research has focused on layer jamming technology to achieve controllable stiffness. Kim *et al.* [61] proposed a tubular snake-like manipulator based on this approach. The layer jamming mechanism, as shown in Figure 2.35, is composed of multiple layers of thin Mylar film and makes use of amplified friction between the films by applying vacuum pressure. The layer-jamming-based manipulator has highly flexible and under-actuated properties. However, it lacks the ability to alter the stiffness of arbitrary segments.

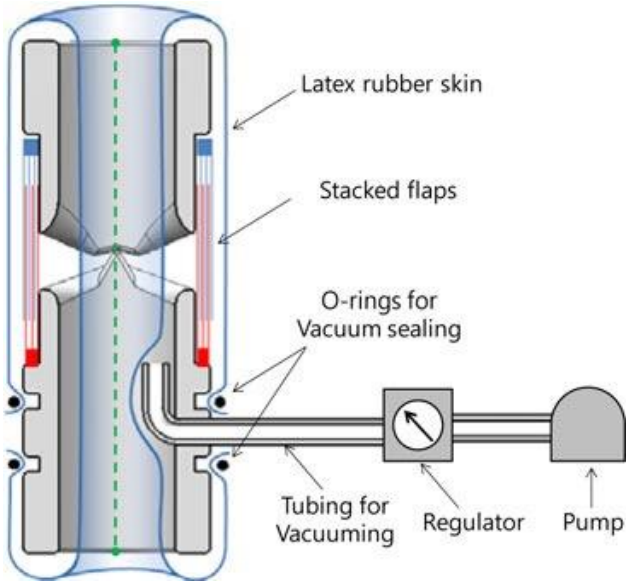

Figure 2.35 Section view of the layer jamming joint [61].

Sadati *et al*. [62] presented an idea of scale jamming inspired by fish and snake scales to control the stiffness of continuum manipulators by controlling the Coulomb friction force between rigid scales (see Figure 2.36). A low stiffness spring is used as the backbone for a set of round curved scales to maintain an initial helix formation while two thin fishing steel wires are used to control the friction force by tensioning [62]. The prototype was tested to control the bending stiffness of an STIFF-FLOP continuum manipulator.

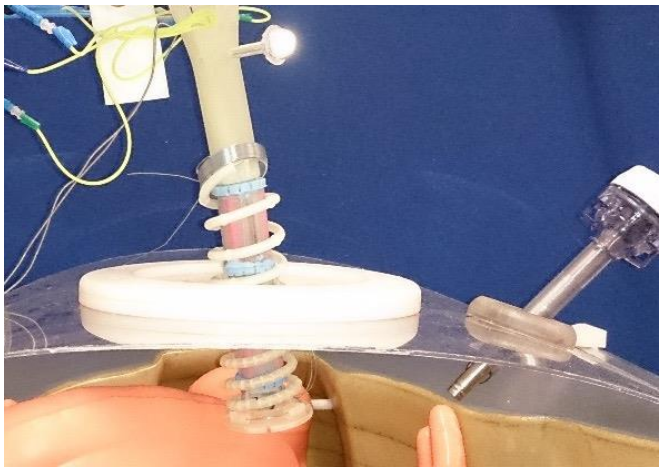

Figure 2.36 STIFF-FLOP manipulator with scale jamming for minimally invasive surgery [62].

2.4.3 Electro- and Magneto- rheological Materials-based Controllable Stiffness Robots

The growing interest in stiffness modulation has led to an increased interest in smart materials. Specifically, materials can rapidly and reversely change their stiffness. Examples include magnetorheological (MR) fluids, electrorheological (ER) fluids, thermorheological (TR) fluids, and granular materials.

MR and ER fluids are known for their capabilities to change rheological properties when magnetic or electric field is applied. When embedded in the soft structure, the same principle can be explored to increase the stiffness of the structure. Majidi *et al*. [10] presented a tuneable stiffness mechanism based on microconfined MR domains. As illustrated in Figure 2.37, when a magnetic field is applied, the fluid in the microchannels form confined magnetic domains that resist separation of the ribbons. Cao *et al*. [63] presented a theoretical study of the design of mesosturctures ER elastomers. A few studies have focused on experimental studies of stiffness change of ER fluids. This is probably due to the shortcomings of the use of ferroelectric particles, as the maximum yield stress they generate is, on average, two orders of magnitude lower [9].

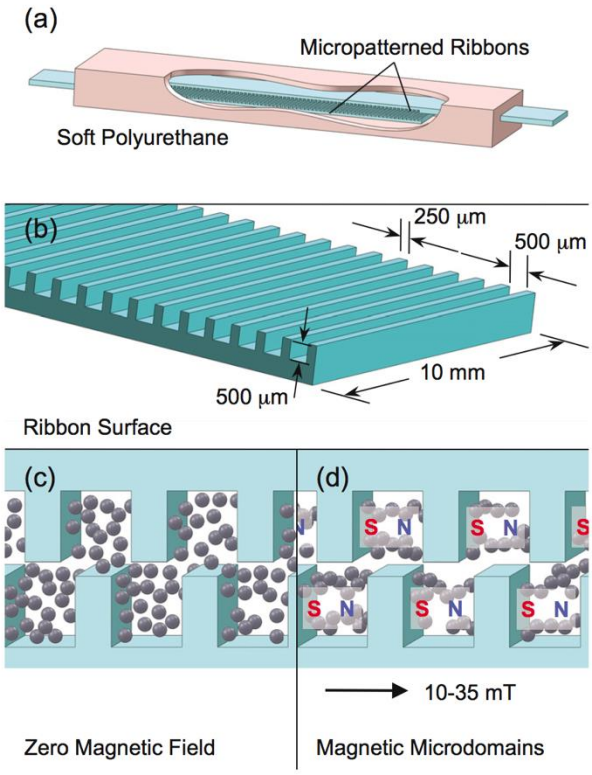

Figure 2.37 (a) An ultrasoft polyurethane elastomer is embedded with rigid, micropatterned ribbons that slide past each other. The tabs are enclosed in a chamber filled with MR fluid. (b) The surface of each ribbon is patterned with an array of aligned microchannels. (c) In the absence of magnetic field, the MR microparticles are randomly dispersed. (d) Under an external field of 10–35 mT, the microparticles form magnetic domains that are confined to the microchannels [10].

2.4.4 Thermorheological Materials-based Controllable Stiffness Robot

TR fluids are another interesting solution to realise stiffness modulation. There have been a series of attempts with wax [18], solder [12] [13], and low melting point alloy [17] [19] to create controllable stiffness elements, and subsequently implemented in the soft structures. Cheng *et al*. [12] proposed a soft mobile robot composed of solder-activated joints. A solder-based locking mechanism was developed to selectively activate individual joints without requiring additional actuators. With the help of the solder-based locking mechanism, the robot can locally modulate the stiffness to dictate the robot's global response to external loading [12]. The locking mechanism consists of a thin layer of 60Sn-40Pb solder, mixed with low melting point alloy sandwiched between two strips of copper tape. The use of low melting point alloy is to lower the melting point of 60Sn-40Pb solder (from 188℃ to 70℃). Figure 2.38 shows the locked and unlocked states of the prismatic joint.

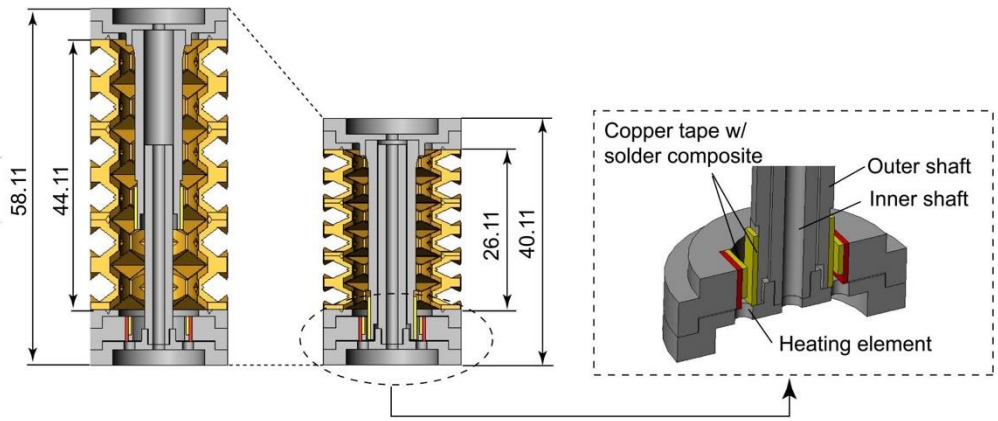

Figure 2.38 Locked and unlocked states of the prismatic joint (left) and integrated solder-based locking mechanism in the prismatic joint (right) [12].

Telleria *et al*. [13] developed a single-actuator, centimetre-scale robot (Squishbot) composed of solder-activated joints. Figure 2.39 shows one of solder-activated flexure joints for Squishbot 1. The locking mechanism consists of 60Sn-40Pb solder and low melting point alloy mixture sandwiched between u-shaped copper elements. This work demonstrates the use of TR fluids, especially solder or low melting point solder, enable a new means of achieving complex tasks with a centimetre-scale robot.

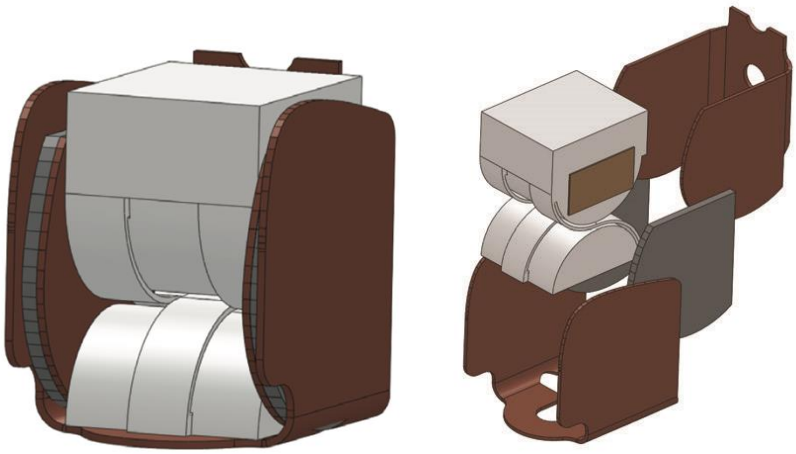

Figure 2.39 3D model of one of solder-activated joints for Squishbot 1 [13].

Wax and solder have successfully demonstrated their potentials, but higher stiffness variation can be achieved if metals are used directly instead. Specifically, the metal itself can be embedded in the soft structure. The combined mechanism can transition between rigid and soft states by controlling the phase of the metal. Schubert *et al*. [17] developed a variable stiffness device based on the combination of low melting point alloy microstructure embedded in soft poly (dimethylsiloxane), as shown in Figure 2.40. The devices tested demonstrate a relative stiffness change of > 25×

(elastic modulus is 40 MPa when low melting point alloy is solid and 1.5 MPa when low melting point alloy is liquid) and a fast transition from rigid to soft states (< 1 s) at low power (< 500 mW) [17].

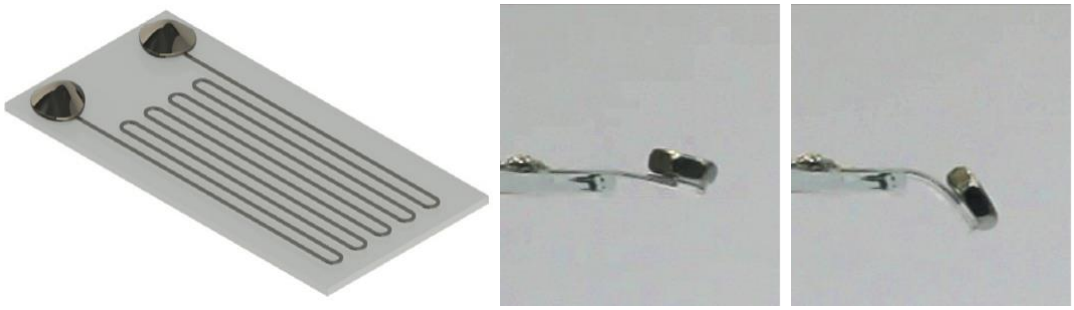

Figure 2.40 Low melting point alloy microstructure embedded in soft poly (dimethylsiloxane) [17].

Shintake *et al*. [19]developed a variable stiffness dielectric elastomer actuator (VSDEA). As shown in Figure 2.41, the device consists of a dielectric elastomer actuator and low melting point alloy embedded in the silicone substrate. The device enables functional soft robots with a simplified structure, where the dielectric elastomer actuator generates a bending actuation and the low melting point alloy provides controllable stiffness between soft and rigid states [19].

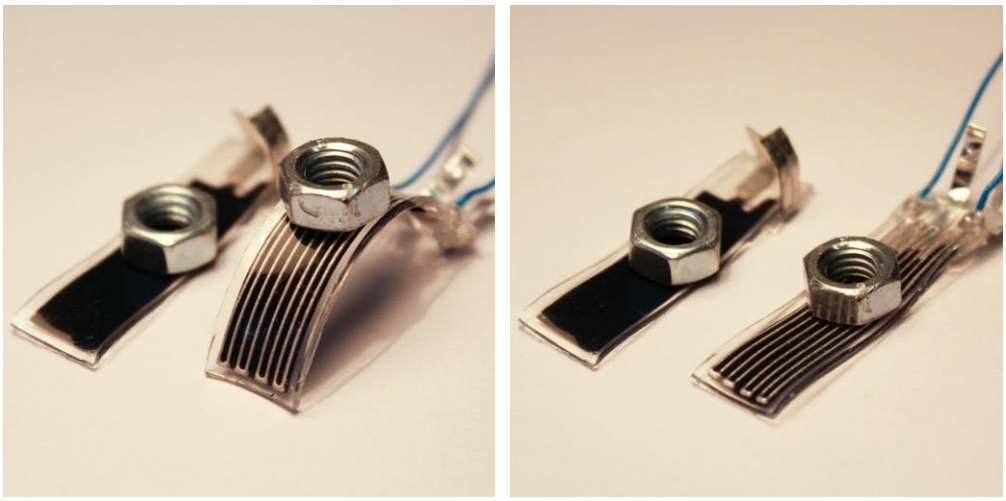

Figure 2.41 Variable stiffness dielectric elastomer actuator (VSDEA). Compared to an actuator without the LMPA, the rigidity of VSDEA is visible (LEFT). The compliance of the device is clear when the LMPA substrate is activated (RIGHT) [19].

2.4.5 Granular Materials-based Controllable Stiffness Robot

Soft robotic manipulator requires stiffness to apply intentional forces to a particular task. Jamming is a useful variable stiffness mechanism for robotic applications due to its simplicity and combination of a relatively fast activation time and capability of transitioning between fluid-like and solid-like states.

Cheng *et al*. [14] developed a highly articulated manipulator based on jamming of granular materials, as shown in Figure 2.42, the device consists of five serial controllable stiffness segments. Each section consists of coarsely ground coffee as granular materials, a low-stiffness compression spring along its length, and an outer flexible membrane. Each segment includes hard end disks for connecting airline and for guiding the tension cables, which ran along the length of the entire manipulator. The airline in each segment is connected to a solenoid valve to enable independent jamming control. Controllable stiffness is thus achieved by applying a vacuum to enclosed granular materials.

Figure 2.42 Highly articulated manipulator based on granular materials [14].

A soft robotic manipulator based on granular jamming was developed by STIFF-FLOP project [15] [16]. As shown in Figure 2.43, the manipulator is composed of a series of homogeneous modules, each consisting of a silicone matrix with a pneumatic chamber for bending and elongating, and one central channel for the integration of granular materials based stiffening mechanism. The manipulator is designed for minimally invasive surgery, where instruments are required to be flexible enough to enable insertion through body cavities without damaging tissues but that are also able to stiffen enough for applying forces to the target site. Granular materials jamming has interesting features, such as high deformability in fluid-like state and a drastic stiffness increase in the solid-like state. However, it requires a substantial volume of granular materials to achieve a significant stiffness change [9].

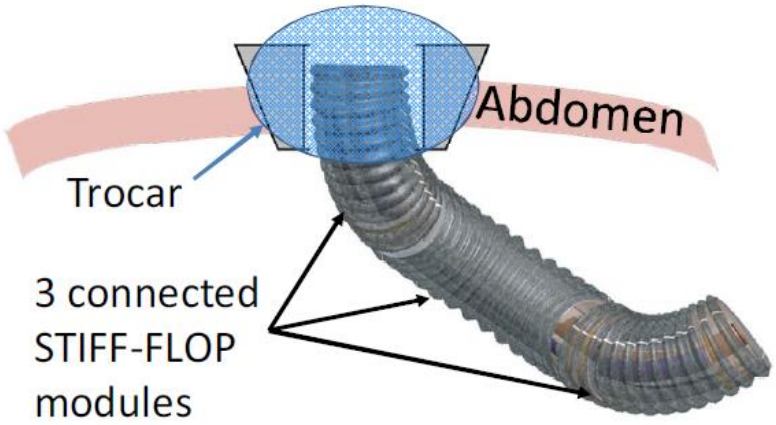

Figure 2.43 Stiff-Flop tuneable stiffness manipulator [15].

2.5 Summary

This chapter provides a thorough review of hard, soft as well as variable stiffness manipulator for medical applications and human-safe industry. A selection of the highly-cited literature was selected and categorized on the basis of their underlying materials and design methods. The investigation of these articles is playing a vital role in developing new robotic systems. It is evident hard robots are not particularly suitable for medical applications or human-safe industry for lacking the capability to negotiate with the working environment. Whereas soft robots can interact with the environments without causing any damage. However, their inherent advantage comes with limited force generation capability, which makes them vulnerable when dealing with manipulation tasks.

In order to overcome these challenges, researchers have shifted their attention to robots with the capability of stiffness modulation. The design of controllable stiffness robot is seen to have evolved into two different directions, i.e. (1) hard robot with soft capability and (2) soft robot with hard capability. A hard robot with soft capability can be realised by using the friction-based method, as demonstrated in ShapeLock [59], TSG [60] and HARP [8] [7]. However, this technology requires a large contact area that can generate sufficient friction to cause stiffness modulation. Therefore, the scalability of this approach is not particularly remarkable.

Robots based on soft materials need be able to modulate the stiffness to be effective. The possibility of altering stiffness can broaden a soft robot capability and enrich its behaviour. Five design methods that can provide a soft robot with hard capability have been summarised in this chapter, along with pros and cons. While MR and ER fluids have fast transition time and good

relative stiffness change, however, they suffer from sealing issue, environmental contamination, and low repeatability, i.e. fluids are subjected to thickening after prolonged use. TR fluids are an interesting solution to realize stiffness modulation. This chapter has reviewed several attempts on using wax, hot-melt adhesive, and low melting point alloy to create controllable stiffness elements in soft robots. However, these materials are thermally activated, which means they require additional heating elements. Their efficiency is affected by thermal input. Granular jamming has been gaining attention recently as an alternative way to achieve soft manipulator with controllable stiffness capability. However, it requires a large volume of granular materials to achieve the stiffness required. Therefore, it is challenging to scale smaller.

Although there is no clear trend to provide stiffness modulation capability for robots, the awareness of the importance of such feature is emerging in robotics community. To the best knowledge of author, there are no attempts on using TR fluids to design a snake-like manipulator with the capability of stiffness modulation. Furthermore, there are no synthesis approaches to design a controllable stiffness manipulator, as well as a systematic comparison of the performances of the designs. Therefore, this research investigates the approaches for on-demand stiffness modulation capability, incorporates current technologies into the design of a snake-like manipulator. Although variable stiffness robotics is a very recent field, this technique could potentially pave the way to new capabilities for manipulation, operation and extraction.

Chapter 3
Material Selection and Characterisation

Two different design principles (bonding between moving surfaces and exploring phase change property) are investigated as active elements in variable stiffness modules. The materials can be used as bonding between moving surfaces and through phase change from solid to liquid are investigated. This chapter presents the selection and the characterisation of the materials used in this research.

3.1 Introduction

A novel snake-like manipulator consisting of multiple homogeneous controllable stiffness modules is developed in this thesis. Two design principles (the materials can be used as bonding agents between moving surfaces and through phase change from solid to liquid), as illustrated in Figure 3.1 and Figure 3.3, are proposed to create controllable stiffness modules:

1) Bonding between surfaces: Materials bonding two surfaces together (e.g. low melting point solder and hot-melt adhesive), where the bonding strength is altered by the application of heat.

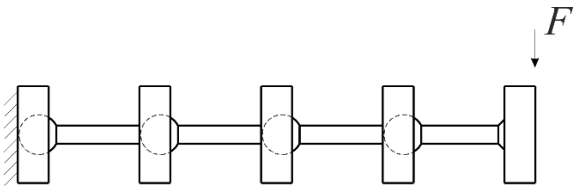

(a) Initial rigid configuration: all joints are non-activated (locking state).

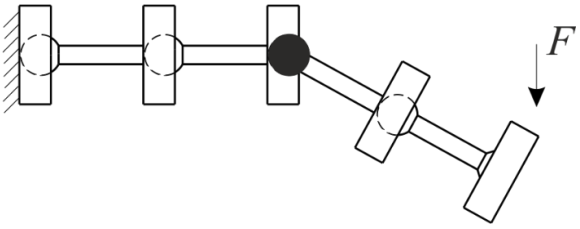

(b) Thermally activated joint in black circle to achieve stiffness modulation (unlocking state).

Figure 3.1 The design principle of the surfaces bonding approach. An external load *F* is applied at the end of the manipulator.

Revolute joint and spherical joint with bending angle 56^{o}, as shown in Figure 3.2, are designed to exploit this principle. The variable stiffness manipulator

can be constructed by a series of revolute joints or spherical joints. The joints can be locked and unlocked when required, thus the stiffness modulation feature can be realized. Detailed design and analysis are provided in Section 4.2.1.

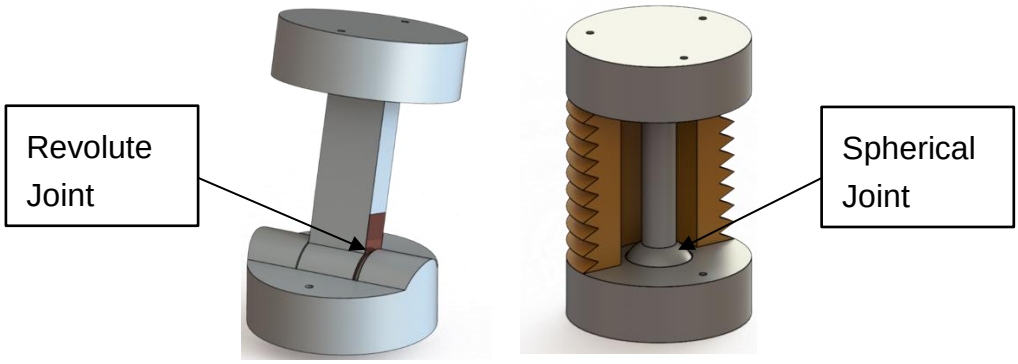

Figure 3.2 Illustration of the revolute joint (a) and spherical joint (b).

2) Phase change property: Materials can be changed from a rigid solid state to a liquid-like state (e.g. low melting point alloy or granular materials) by the application of heat or vacuum pressure.

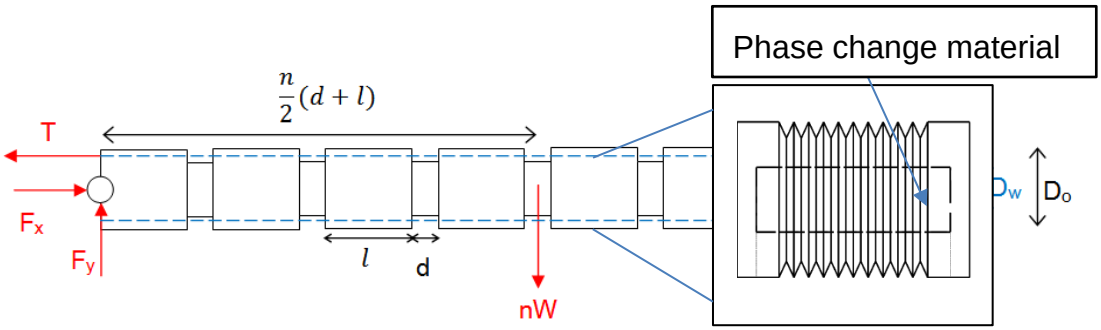

Figure 3.3 A manipulator consisted of multiple variable stiffness single modules.

Figure 3.3 shows a snake-like manipulator consisting of multiple variable stiffness continuum modules. The soft continuum module, as shown in Figure 3.4, is designed to accommodate the phase change material (fusible alloy or granular material). Detailed design and analysis are presented in Section 4.2.2.

The variable stiffness manipulator is consisted of multiple soft modules. The stiffness modulation feature is realised by the controllable stiffness element of each module. The state of the phase change material can be altered by the application of the heat or vacuum pressure.

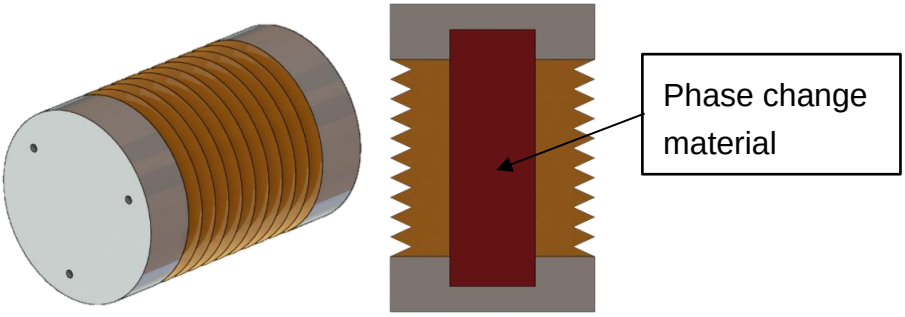

Figure 3.4 Soft continuum module is designed to accommodate the phase change material.

In this chapter, three thermorheological (TR) fluids, i) low melting point solder, ii) hot-melt adhesive, iii) low melting point alloy and iv) granular materials are investigated including:

1) The ease at which materials enters the rigid state or soft state (i.e. response time between solidus temperature and liquidus temperature);
2) The stiffness/strength of the system in rigid state;
3) The stiffness/strength of the system in soft state;
4) The cyclic repeatability of these metrics.

The material properties, as illustrated in Table 3.1, are characterised in this chapter.

Table 3.1 Proposed Materials and Their Experimental Characterisation.

Design Principle	**Materials**	**Experimental Characterisation**
Bonding between Surfaces	Low Melting Point Solder (LMPS)	• Solidus temperature • Temperature-dependent of bonding strength • Repeatability
	Hot-melt Adhesive (HMA)	• Solidus temperature • Temperature-dependent of bonding strength • Adherend-dependent of bonding strength • Repeatability
Phase Change Materials	Low Melting Point Alloy (LMPA)	• Solidus temperature • Elastic modulus

	Granular Material (GM)	• Elastic modulus under different vacuum pressure

The main body of the proposed modules is constructed by two different types of the silicone materials. The properties of the silicone materials are investigated in the end.

3.2 Low Melting Point Solder (LMPS)

LMPS has been increasingly used in the recent development of small-scale robots [12, 13, 64]. The idea is to use LMPS to form the rigid bond between interfaces when the solder temperature is below the melting point. The bond can be easily separated through thermal input. LMPS is utilized in the development of hard-jointed manipulator with soft capability. The proposed manipulator consists of multiple homogeneous modules. Each module is composed of thermally activated lockable joints (revolute joints or spherical joints) and soft structures. The compliance is achieved through the use of the soft structures. LMPS is used to design the locking mechanism that can be employed by robot joints. The joints can be selectively locked and unlocked, therefore modulating global stiffness of the manipulator. The concept is illustrated in Figure 3.1.

3.2.1 Material Selection

The most common solder for electrical and electronics applications is 63% Sn, 37% Pb. The use of 63% Sn, 37% Pb solder for thermally activated lockable joints has been proven to be successful in [12, 13], where solder and low-temperature alloy mixture was used to design thermally-activated locking mechanism for small-scale robot joints. Due to the high melting point temperature (188°C), a low melting point alloy (Chip Quik) is used to lower the melting point. However, there are several problems regarding solder and low-temperature alloy mixture. First, there is no quantitative method to mix two materials (i.e. the ratio between solder and Chip Quik is unknown), the melting point is different for different batches. Second, the shear strength of the mixture was found to be too weak to be used in the design of the lockable mechanism. Therefore, solder with low melting point temperature needs to be considered. Candidate materials are listed in Table 3.2.

When selecting candidate solder materials, several criteria need to be considered. First, solder with low melting point temperature is desirable. The

melting point determines the overall power consumption. It should be as low as possible to minimise power and to avoid the damage of single module as well as working environment. Secondly, it is necessary to select a solder with non-hazardous composition. Alloys containing Mercury or Cadmium do not meet this requirement due to their known health effects [64]. Of the materials listed in Table 3.2, 32.5% Bi, 51.0% In, 16.5% Sn (Field's metal) is the lowest melting point (62 °C) that meets both requirements. Therefore, it was selected to design locking mechanism that can be employed by the joint.

Table 3.2 Melting Points for a Selection of Low Melting Point Solders [65].

Composition or Common Name	Melting Point (°C)
40.3% Bi, 22.2% Pb, 10.7% Sn, 17.7% Cd, 8.1% In, 1.1 % TI	41.5 °C
44.7% Bi, 22.6% Pb, 19.1% In, 5.3% Cd, 8.3% Sn (Cerrolow 117)	47.2 °C
49% Bi, 18% Pb, 21% In, 12% Sn (Cerrolow 136)	58 °C
32.5% Bi, 51.0% In, 16.5% Sn (Field's metal)	62 °C
50.0% Bi, 25.0% Pb, 12.5% Sn, 12.5% Cd (Wood's metal)	71 °C
42.5% Bi, 37.7% Pb, 11.3% Sn, 8.5 % Cd (Cerrosafe)	74 °C
50.0% Bi, 28.0% Pb, 22.0 % Sn (Rose's metal)	98 °C

3.2.2 Experimental Characterisation

3.2.2.1 Solidus Temperature

In order to understand the temperature at which the solder becomes solidified, solidus temperature needs to be determined. Since this property is not provided by the manufacture, the simplest way to determine solidus temperature is through experiments. Figure 3.5 illustrates the experimental setup used to establish solidus temperature of LMPS. Solder-coated copper tapes and resistance wires were prepared for the experiments. Resistance wires were wound and closely attached to the copper taper. Solder was initially heated by the resistance wires behind the copper tape when the temperature reached the melting point. A copper wire was then used to poke the solder to determine when it solidified, a k-type thermocouple was attached

to the surface to record the temperature. Five trials were conducted, and the average solidus temperature for low melting point solder is 60.2°C.

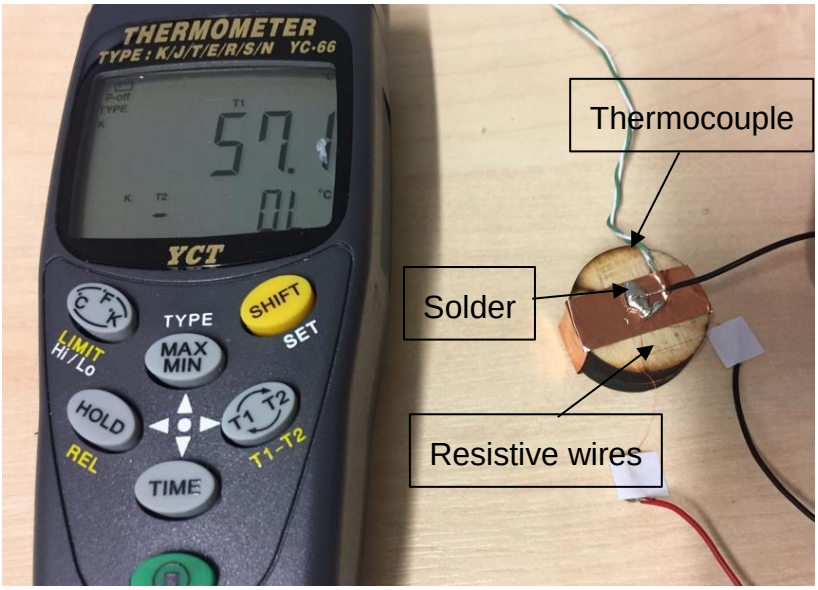

Figure 3.5 Experimental setup used to measure the solidus temperature of LMPS.

3.2.2.2 Temperature-dependent of Bonding Strength

After the bond has been formed, the bonding strength between LMPS and copper tapes could be influenced by the temperature. As the temperature reaches to the melting point, LMPS is becoming liquefied. The bond can be easily separated. To understand the temperature influence on bonding strength of LMPS, temperature-dependent bonding strength experiments were conducted.

The test rig, as shown in Figure 3.6, consists of a heating element (Lite6, e3d-online.com), a temperature controller, a k-type thermocouple, LMPS-coated copper tapes, and a wooden cylinder, and wooden plates. The direction of the separation of the wooden plates is illustrated in the figure. Specifically, LMPS-coated copper types were initially glued on the wooden cylinder and plate. The wooden cylinder with solder-coated copper tape was manually placed above the cope tape, LMPS was heated by the heating element above the melting point to form the bond. When the bond returned to room temperature, top wooden plate was placed above the bottom plate through the cylinder. Then they were clamped on the Instron test machine. Then the heater was activated again, and the temperature was adjusted accordingly. The force that breaks the bond was recorded by Instron test machine when two plates were pulled apart. The bonding area was measured after the plates were separated.

Bonding strength was evaluated as the ratio between breaking force and bonding area.

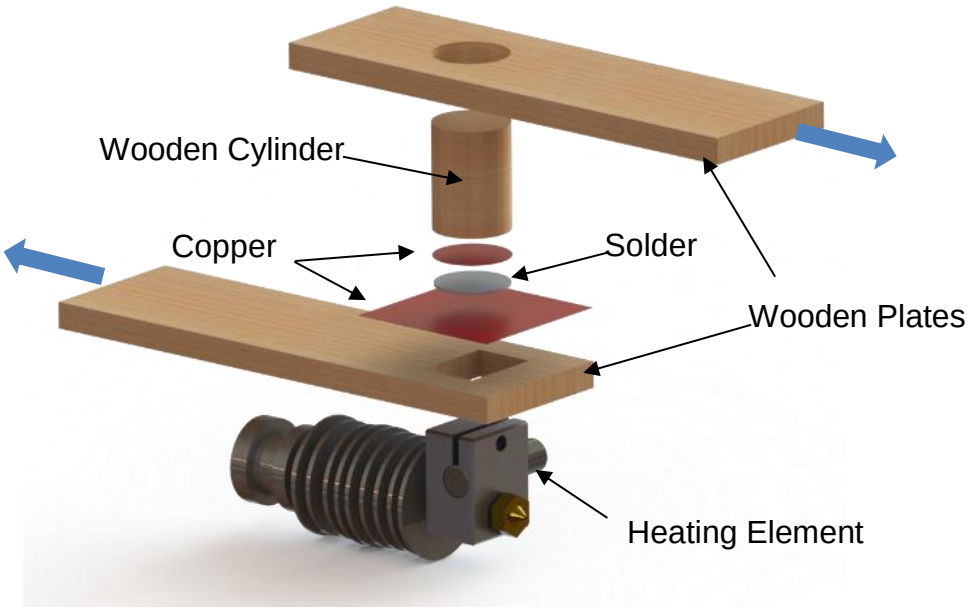

Figure 3.6 CAD model of test rig for temperature-dependent of bonding strength test.

Experimental setup for temperature-dependent of bonding strength test is shown in Figure 3.7. The direction of the separation of the wooden plates is illustrated in the figure. K-type thermocouple and temperature controller are illustrated in the graph. Three trials were conducted.

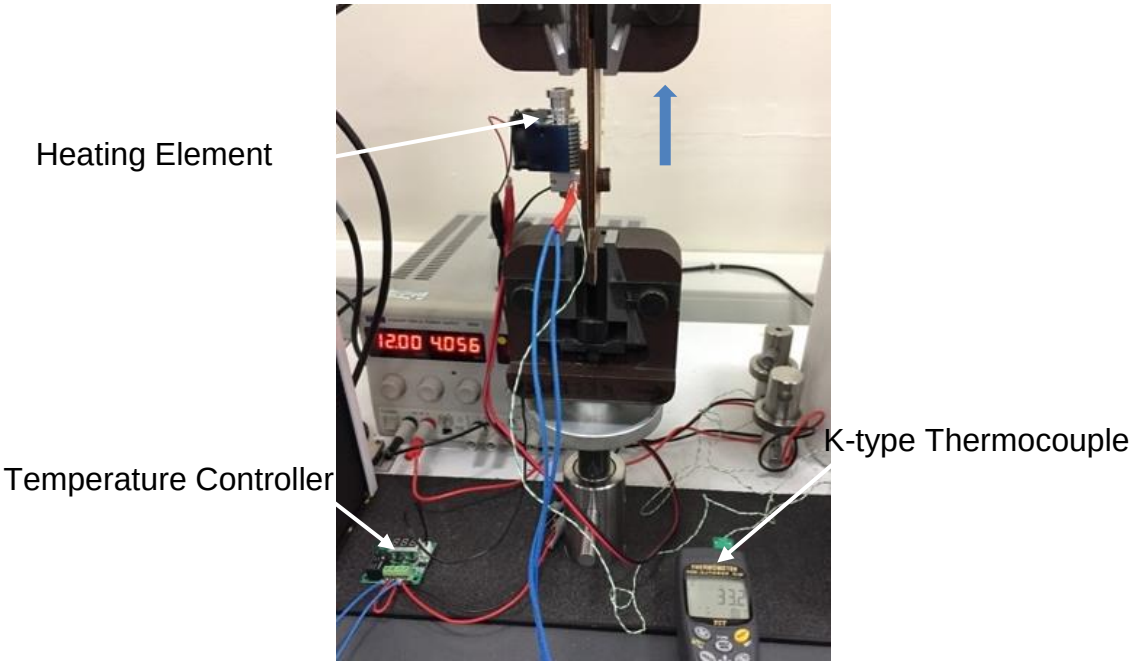

Figure 3.7 Experimental setup for temperature-dependent of bonding strength test.

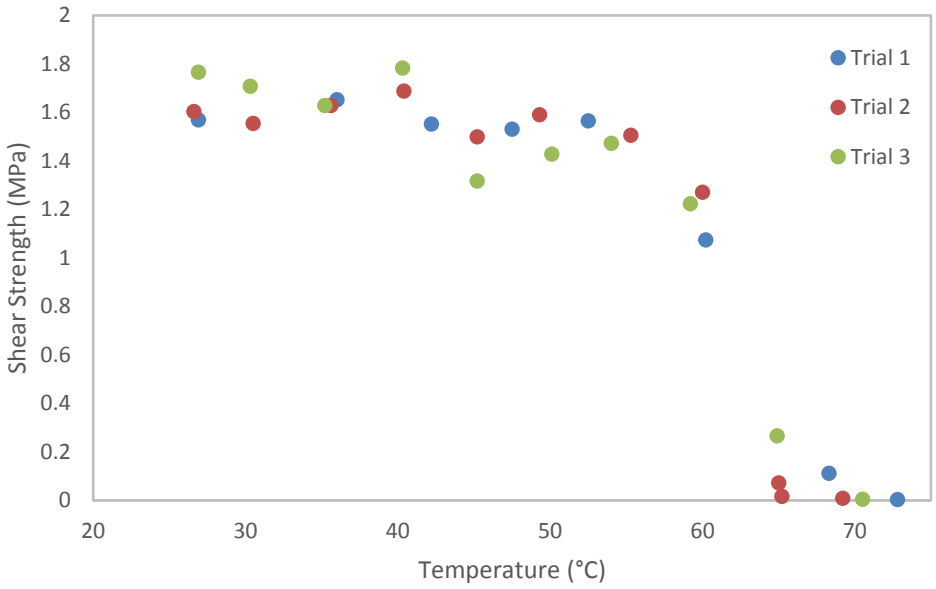

Figure 3.8 Test results of shear strength (MPa) at different temperature. Three trials were conducted.

The result, as plotted in Figure 3.8, shows that when the temperature is below the melting point (62 °C), it has limited effect on the bonding strength of LMPS. However, when the temperature is above the melting point, bonding strength reduces dramatically. For example, the bonding strength is as high as 1.65 MPa at room temperature. When the temperature reaches ~50 °C, the bonding strength is reduced only by 8.32%. When the temperature is above 62 °C, bonding strength decreases by 94.2%.

3.2.2.3 Repeatability

LMPS can transition between solid-like state and fluid-like state. However, repeated transition may affect the bonding strength between LMPS and interfaces. To evaluate the repeatability of LMPS, repeated locking and unlocking experiments were conducted.

The test rig, as shown in Figure 3.9, was used to mimic the locking and unlocking motion of the lockable mechanism. It is composed of a resistive heater, copper tapes, LMPS, a wooden cylinder, and wooden plates. The rotational motion of the joint was simulated by rotating the wooden cylinder. The circular motion of the cylinder is illustrated as a blue curved arrow in Figure 3.9. LMPS was first heated by resistive heater behind the copper tape to activate the joint, then wooden cylinder was rotated to mimic the motion of the joint. Each repetition contains one cycle of locking-rotating-unlocking motion. When the bond was cooled down to room temperature, two wooden plates were pulled apart by Instron test machine. The direction of the

separation is illustrated as black arrows in Figure 3.9 and Figure 3.10. Shear force was recorded by the Instron machine. Shear strength of each repetition was evaluated as the ratio between shear breaking force and the bonding area. Experimental setup for repeatability test of LMPS is shown in Figure 3.10. Three trials were carried out, each trial consists of 80 repetitions. Shear strength was evaluated after 20, 40, 60 and 80 repetitions.

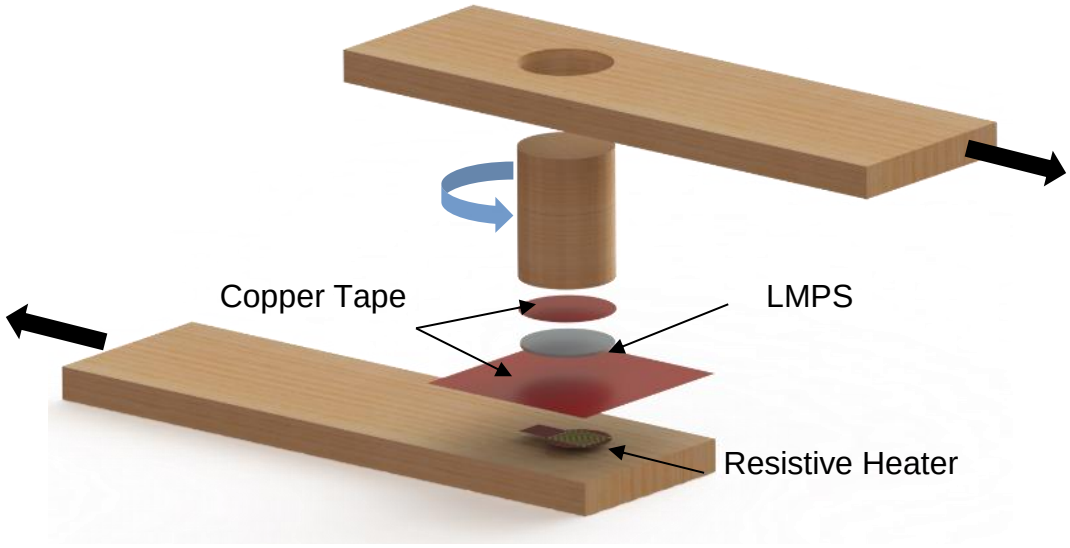

Figure 3.9 CAD model of test rig that used to simulate the rotational motion of the joint. The circular motion of the cylinder is illustrated as a blue curved arrow. The direction of the separation of the wooden plates are illustrated as black arrows.

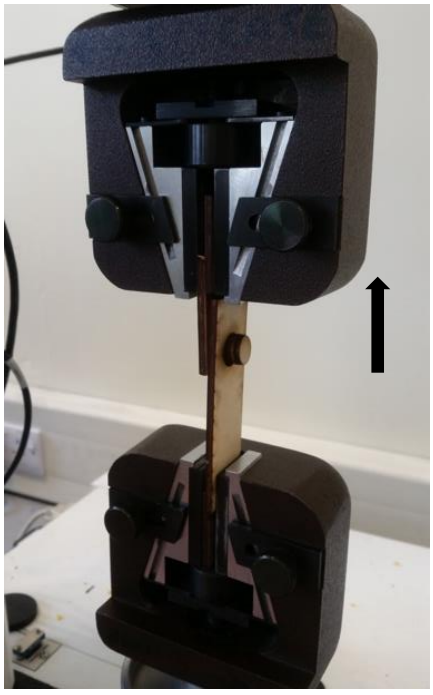

Figure 3.10 Experimental setup for repeatability test of LMPS**.**

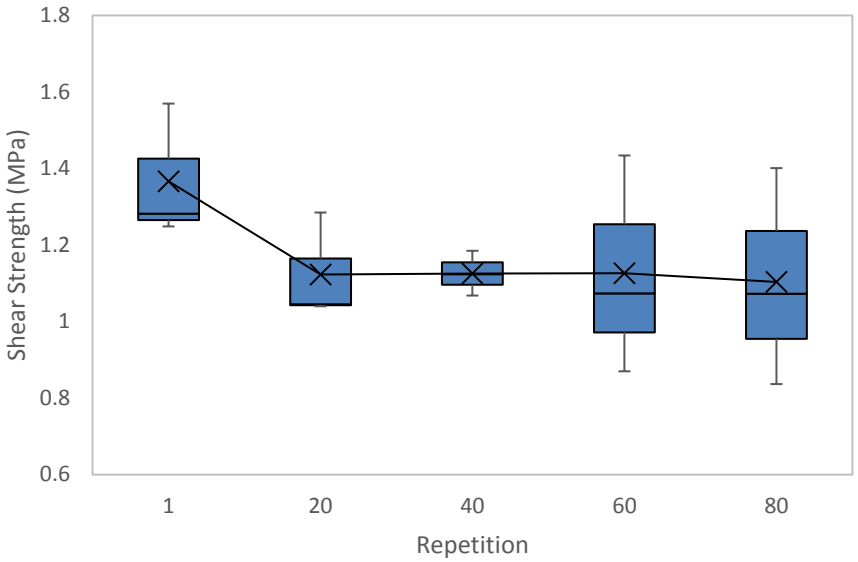

Figure 3.11 Shear strength of LMPS over repetitions.

Figure 3.11 shows experimental results for shear strength of LMPS over repetitions. Shear strength steadily decreases over the repetitions. Specifically, after 20 repetitions, shear strength is reduced by 17.8%, maintains steady between 20 to 60 repetitions, decreases by 19.2% after 80 repetitions. A likely explanation for the decrease of the shear strength is the circular motion of the wooden cylinder, with the mass of the bonding materials being lost over the repetitions. When designing lockable module that employs LMPS as the locking mechanism, the material could be sealed in a confined space to improve the repeatability.

3.3 Hot-Melt Adhesive (HMA)

Another approach to design controllable stiffness mechanism is based on thermoplastic adhesives. HMA, also known as hot glue, is the most common form of thermoplastic adhesives. HMA is capable of being repeatedly softened by increasing temperature and solidified by decreasing temperature to form strong bonds between varieties of materials. When the temperature is below the melting point, interfaces are bonded firmly by a hot-melt adhesive. It can also be easily detached by increasing the temperature of HMA.

3.3.1 Material Selection

When seeking candidate materials, the low-temperature melting point is mostly desirable. Low-temperature glue stick with melting point 75 °C was therefore selected for HMA-based controllable stiffness mechanism.

3.3.2 Experimental Characterisation

3.3.2.1 Solidus Temperature

Solidus temperature of HMA was determined experimentally. The experimental setup was equivalent to the tests conducted on LMPS (as shown in Figure 3.5). A small piece of HMA was initially melted by the resistive wires placed behind the copper tape. A wire was then used to prod the HMA to determine when it solidified, a k-type thermocouple was attached to the surface of the taper to record the temperature change. Five trials were conducted, the average solidus temperature of HMA is 50.8 °C.

3.3.2.2 Temperature-dependent of Bonding Strength

After the bond has been formed, the bonding strength can be dramatically influenced by the temperature [66, 67]. To evaluate the temperature influence on bonding strength of HMA, temperature-dependent of bonding strength experiments were conducted. Experimental setup and test rig were equivalent to the LMPS test. The bond was initially formed and cooled down to room temperature. The wooden plates were then clamped on the test machine. The bond was separated from room temperature to 70 °C, the shear force was recorded accordingly. Afterwards, the bonding area was measured, and shear strength was calculated as the ratio between shear force and the bonding area.

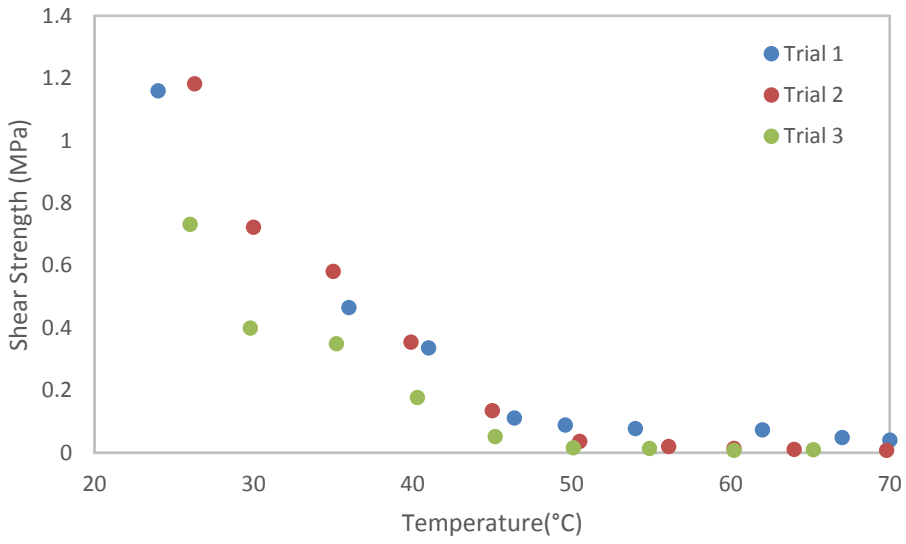

Figure 3.12 Shear strength of HMA at different temperature.

The result, as shown in Figure 3.12, illustrates the bonding strength of HMA between copper tapes exponentially decreases as the temperature increases. For example, the shear strength is as high as 1.1 MPa at room temperature,

as the temperature increases to 70 °C, it is reduced to 0.007 MPa. By simply reheating the bond, the interfaces can be easily detached from one to another. This characteristic can be exploited by the single module to achieve the design locking mechanism. It is also important to point out that the bonding strength is varied at the different temperature. By varying the external force, separation of the bond can happen before the melting point temperature is reached. Therefore, minimising the response time can be realised.

3.3.2.3 Adherend-dependent of Bonding Strength

The bonding strength of HMA varies between materials of adherends. To understand the difference, direct shear tests of HMA between different types of adherends were conducted. Several adherends materials, such as aluminium, stainless steel, copper, plastic, wood, and glass could be considered. However, when seeking candidate adherends, two additional criteria apply. First, light weight material is desirable. Second, the material should be easy to use in the process of fabrication. Therefore, plastic (VeroWhitePlus), aluminium, and copper were investigated.

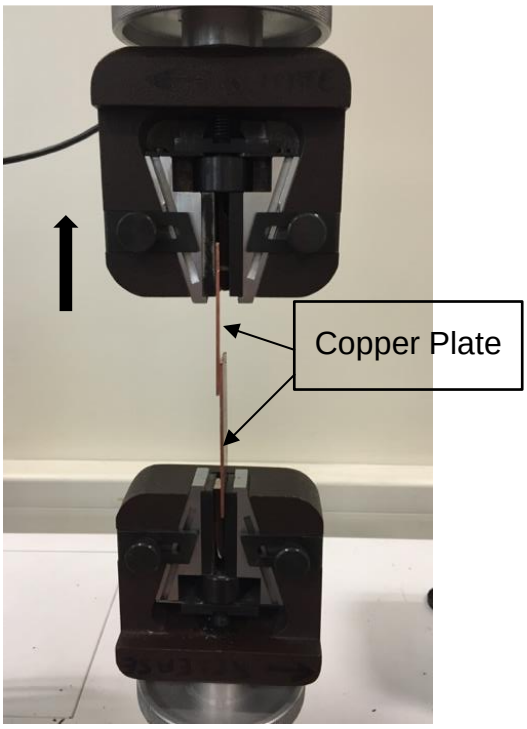

Figure 3.13 Experimental setup for adherend-dependent of bonding strength test. Two copper plates were glued together by HMA.

Two separate plates (80 mm x 30 mm) made of candidate adherends were first prepared. The surfaces of the plates were pre-treated to form effective bonds. The HMA was supplied manually by a hand-held hot glue gun. Once the bond was formed, two separate pieces were then clamped on Instron test machine. When the bond returned to room temperature, two plates were

pulled apart, the shear force needed to break the bond was recorded accordingly. The experimental setup for adherend-dependent of bonding strength test was shown in Figure 3.13, the direction of the separation of the plates is illustrated as a blue arrow.

Table 3.3 details the numerical results for the shear strength between HMA and candidate adherends at room temperature. Five trials were conducted for each adherend. The bonding area was measured after the separation of plates. Shear strength was calculated as the ratio between shear force and the bonding area. Note that shear strength between HMA and aluminium is similar to the shear strength between HMA and copper. However thermal conductivity of copper (401 W/mK) is significantly greater than aluminium (205 W/mK), copper was therefore selected as adherend for HMA.

Table 3.3 Shear strength between HMA and candidate materials.

Materials	**Shear Strength (MPa)**
Aluminium	1.0562±0.1770
Copper	1.0496±0.2443
Plastic	0.1846±0.0373

3.3.2.4 Repeatability

HMA-based locking mechanism should be able to withstand multiple cycles before failure occurs. To understand the importance of cycling, repeated locking-unlocking cycles tests were conducted. Three trials were carried out, each trial contains 80 repetitions. The test rig (see Figure 3.9) and experimental protocol were equivalent to the LMPS test. The result is plotted in Figure 3.14. The shear strength of HMA is as high as 1.0713 MPa after the first separation. It decreases by 16% after 20 repetitions, by 24% after 80 repetitions. The decrease of shear strength of the HMA over repetition is likely explained by the loss of the mass of bonding material. In comparison to the test results shown in [67], in which the author used HMA to construct a climbing robot, the bonding strength reduced by 50% after 25 repetitions. Due to the difference of design principal and test rig, oxidative degradation and complete separation happen in the case of [67]. Whereas for our repeatability test, there was no complete separation during the trial. Therefore, the difference of the decrease of bonding strength of HMA can be explained.

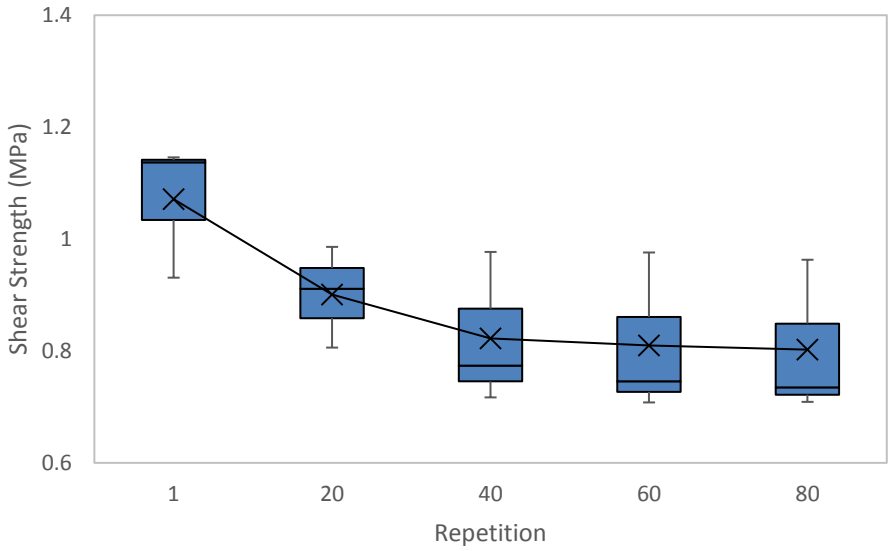

Figure 3.14 Shear strength of HMA over repetitions.

3.4 Low Melting Point Alloy (LMPA)

The phase change materials are alternative solution to create controllable stiffness module. They are capable of transforming between fluid-like state by increasing the temperature above the melting point and solid-like state by cooling. LMPA, as one of commonly used phase change materials, is proposed to design controllable stiffness mechanism for the single module. The idea is to design a soft silicone structure embedded with LMPA, the stiffness of the module is controlled by the state of the alloy.

3.4.1 Material Selection

Low melting point and inexpensive cost are considered as criteria to seek the candidate alloy for proof of concept design. Table 3.4 lists a selection of LMPA. Lens alloy is one of an interesting range of bismuth-based alloys to which the element indium is added to give a substantially lower melting point. It is easily melted and having extremely stable characteristics [68]. However, alloys containing Mercury or Cadmium do not meet this requirement due to their known health effects. Of the alloys listed in Table 3.4, Lens 136 (bendalloy.co.uk) has the lowest melting point meets both requirements. Therefore, it was selected to design controllable stiffness mechanism that can be exploited by the single module.

Table 3.4 Melting Points for a Selection of Low Melting Point Alloys [65].

Composition or Common name	Melting Point
44.7% Bi, 22.6% Pb, 19.1 % In, 8.3% Sn, 5.3% Cd (Lens 117)	47 °*C*
49% Bi, 21% In, 18% Pb, 12% Sn (Lens 136)	58 °*C*
32.5% Bi, 51.0% In, 16.5% Sn (Field's metal)	71 °C
50.0% Bi, 25.0% Pb, 12.5% Sn, 12.5% Cd (Wood's metal)	74 °C
50.0% Bi, 28.0% Pb, 22.0 % Sn (Rose's metal)	98 °C

3.4.2 Experimental Characterisation

3.4.2.1 Solidus Temperature

Solidus temperature of LMPA was determined experimentally. The experimental setup was equivalent to the LMPS test. A small piece of LMPA was initially melted by the resistive wires placed behind the copper tape. A copper wire was then used to prod the alloy to determine when it solidified, a k-type thermocouple was attached to the surface to record the temperature. Five trials were conducted, the average solidus temperature is 56.7 °C.

3.4.2.2 Elastic Modulus

Due to the use of soft silicone materials, the proposed LMPA-based single module has a highly compressible structure. The stiffness of the single module can be characterised as elastic modulus in axial direction. In order to understand the rigidity of the module, the elastic modulus of LMPA needs to be determined first. This property was identified in the compression tests.

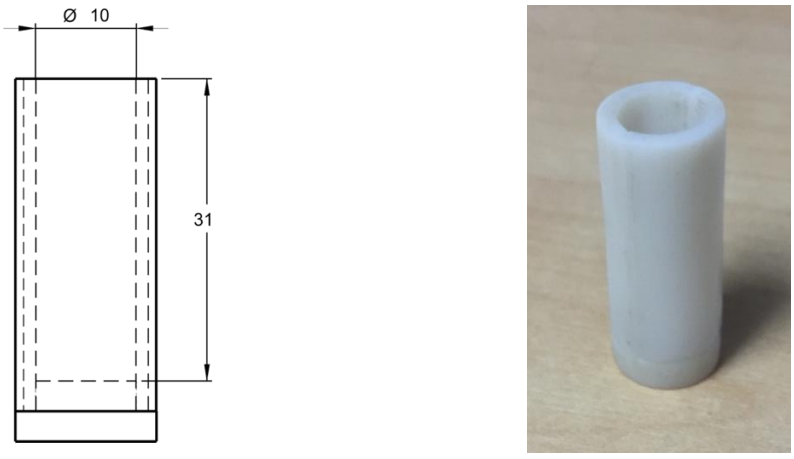

Figure 3.15 Dimension and the prototype of the mould for casting cylindrical specimen.

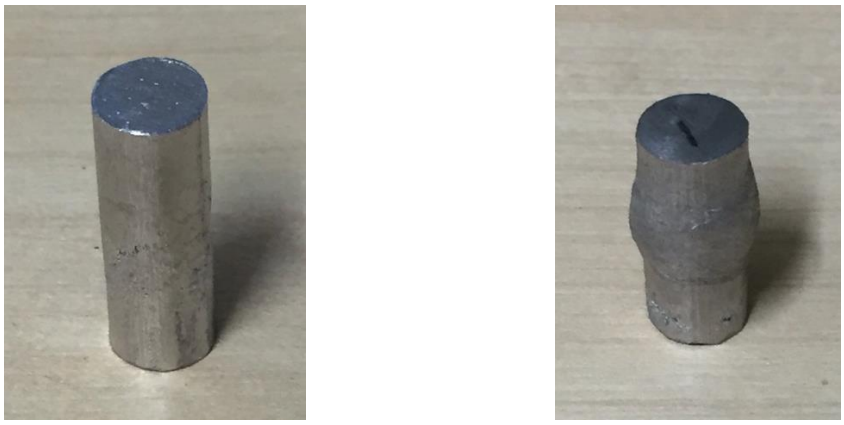

Figure 3.16 Cylindrical specimen before (LEFT) and after (RIGHT) compression test.

The ratio of initial length to diameter (L_0/D) has the significant influence on the test results [69]. Medium-length specimens are typically used for determining the general compressive strength properties of metallic materials [70]. Medium cylinder specimens ($2 \leq L_0/D \leq 8$) were therefore used for the compression tests. The melted alloy was cast into 3D printed mould with a diameter of 10 mm and a height of 31 mm. Figure 3.15 illustrates the dimension and the components of the mould. The compression speed of 2 min/min was maintained constant throughout the test. Before and after tested specimen were illustrated in Figure 3.16. Five samples were tested at room temperature. The average length of the specimen was 30.61 mm, the average diameter was 10.285 mm. Therefore, the medium specimen ($L_0/D = 2.98$) requirement was met.

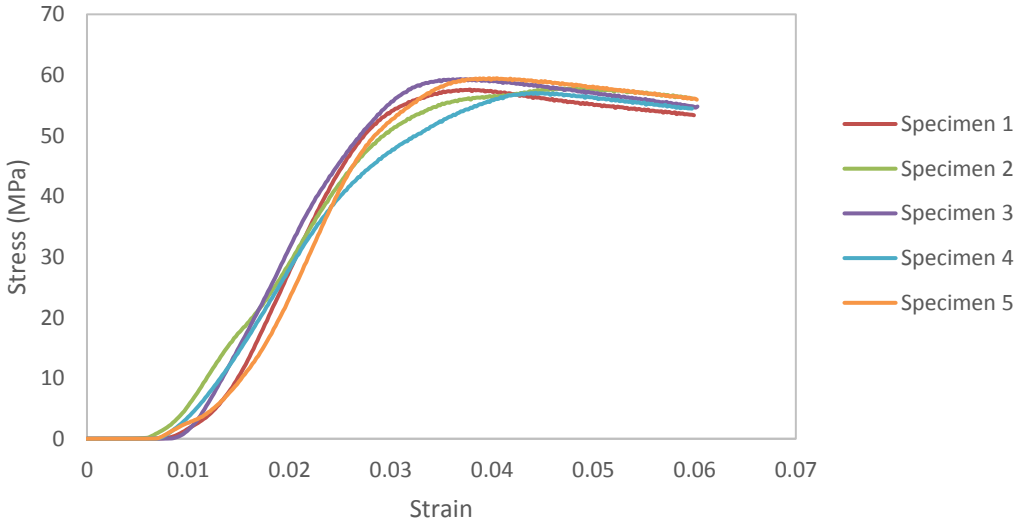

Figure 3.17 Stress-strain curves of LMPA from compression tests.

Figure 3.17 shows stress-strain curves of low melting point alloys. The elastic modulus was determined based on the stress-strain graph where the curve is almost linear. The compression test was conducted for a short duration to limit the temperature growth on the samples. Average experimental elastic modulus of selected LMPA is calculated as 2884.96±401.03 MPa.

3.5 Granular Materials (GM)

Granular materials have recently been drawn attention to the field of soft robotics. They are also known to exhibit reversible transition behaviour. In recent robotic applications, granular materials were adopted as a simple mechanism to achieve controllable stiffness components [14]. The stiffness can be modulated by applying vacuum pressure to granular materials, which cause materials to push against each other, creating a rigid structure. Once the pressure is released, the material assembly becomes soft. The concept is illustrated in Figure 3.18.

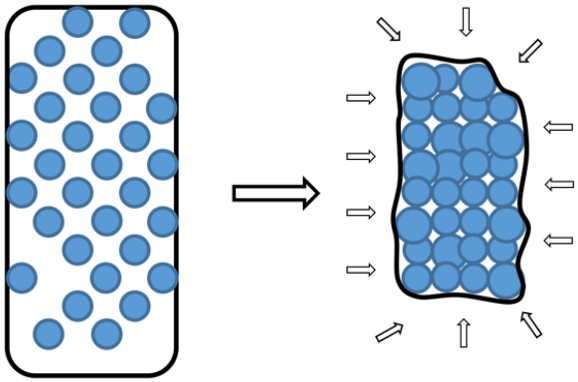

Figure 3.18 A schematic of a controllable stiffness mechanism consists of granular material contained in a flexible membrane.

3.5.1 Material Selection

Compression tests were conducted by Cheng et al. [14] [71] to investigate the mechanical properties of several lightweight granular materials. The tested materials include coarsely ground coffee, finely ground coffee, sawdust, diatomaceous earth, hollow glass spheres and solid glass spheres. Of all the materials studied, ground coffee produced the most desirable combination of high strength-to-weight ratio and large absolute strength [14]. Furthermore, in Cheng's PhD thesis [71], where a total number of 25 granular materials were evaluated. Ground coffee yielded a favourable combination of exhibiting high strength and low density. Therefore, coarsely ground coffee was selected as granular media in this work.

3.5.2 Elastic Modulus

Compression tests were conducted on coarsely ground coffee to evaluate the elastic modulus under different vacuum pressure. Cylindrical test samples, with average diameter and height of 13 mm and 32.24 mm, respectively, were prepared for the compression tests. As shown in Figure 3.19, the sample consists of coarsely ground coffee beans containing in a latex membrane. 1.5 mm inside diameter tube is used as vacuum pipe, and the connection between the tube and membrane was sealed with Parafilm. The experiments were conducted five times, at the compression speed of 5mm/min. The experimental setup for the compression test was presented in Figure 3.20.

Figure 3.19 Specimen for compression test. The test sample consists a latex membrane and coarsely ground coffee.

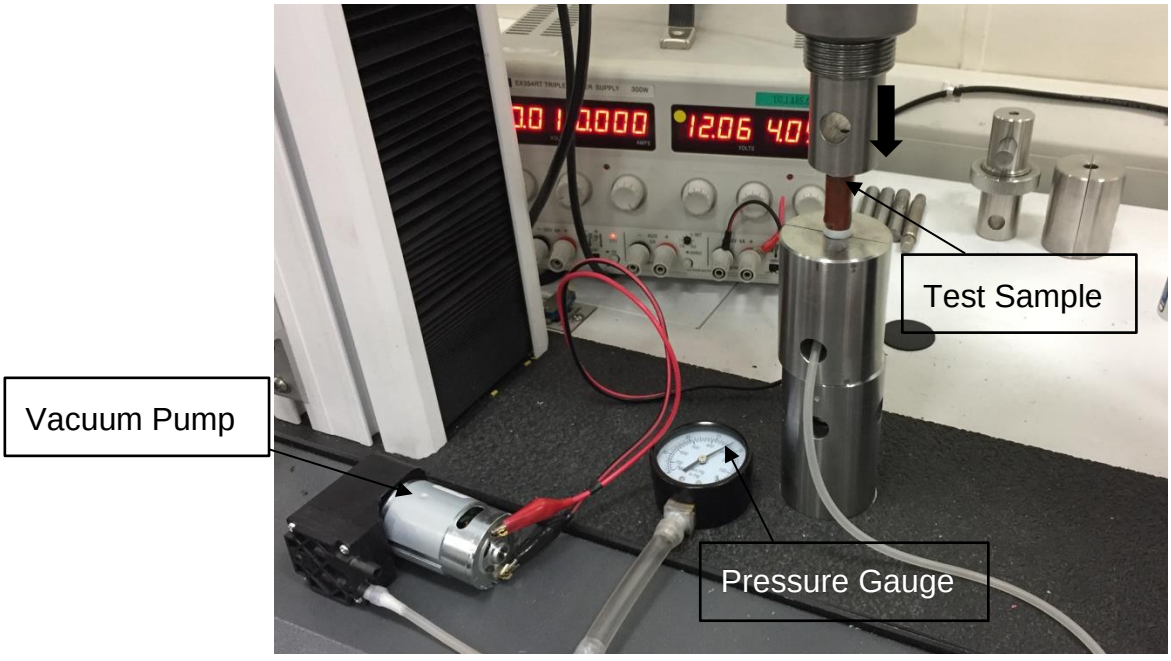

Figure 3.20 Experimental setup for compression test. Vacuum pump, pressure gauge and test sample are illustrated in the figure.

Figure 3.21 shows the stress-strain curves of the granular material under three different pressure, i.e. atmospheric pressure, 100 mmHg, and 180 mmHg. Figure 3.22 shows the calculated elastic modulus of the tested sample at three different pressure levels. The elastic modulus of the granular material was calculated as 0.1192±0.0010 MPa at atmospheric pressure. The number reaches to 0.2683±0.0428 MPa at 100 mmHg pressure and 0.3967±0.009 MPa at full vacuum pressure (180 mmHg).

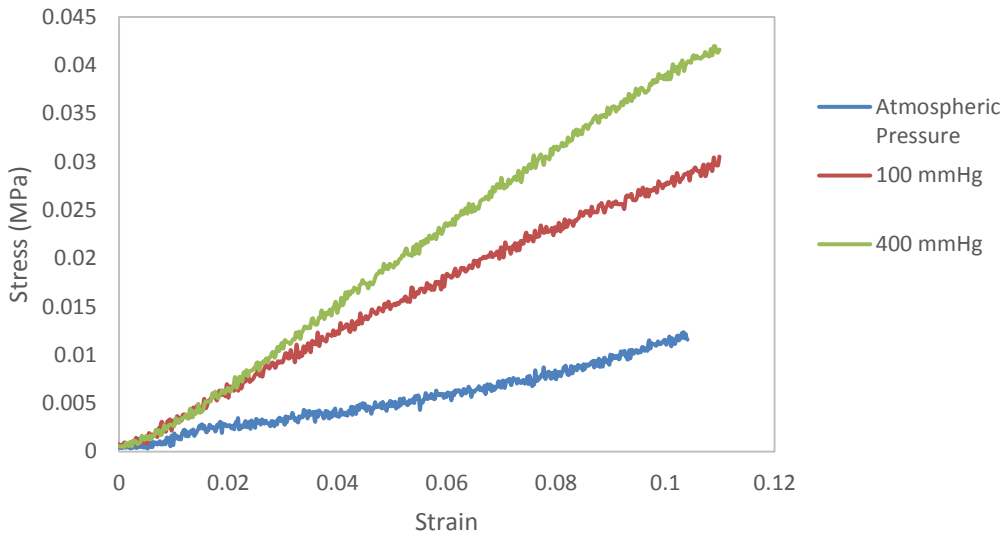

Figure 3.21 Stress vs strain of granular material at three different vacuum pressure.

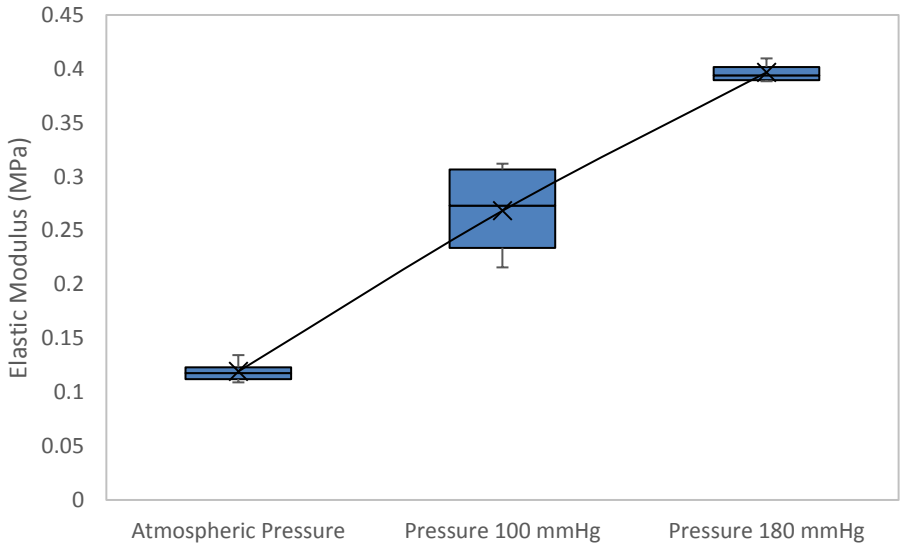

Figure 3.22 Elastic modulus of the tested sample at different vacuum pressure level. The numbers were calculated based on stress-strain curves obtained from compression tests.

3.6 Silicone Materials

Silicone rubbers were used for the fabrication of soft structures of the single modules. They are widely used in the development of soft robots. It is generally non-reactive, stable, and resistant to extreme environments and temperatures from -55 °C to +300 °C while still maintaining its function [72]. Two types of silicone rubber, i.e. Ecoflex 0030 and Dragon Skin 30, were selected for the fabrication of the soft structures due to high flexibility and high Shore hardness, respectively. For non-granular devices, the silicone materials can also be used as heat sinks to isolate the heat flow out of the devices.

The mechanical behaviour of silicone material is known to be strain rate dependent. In this section, the strain range of the proposed single modules was estimated in SolidWorks Simulation. The angular speed of the device was proposed. The strain rate dependent behaviour of the silicone material was investigated. Experiments were conducted to obtain the stress-strain behaviours of the silicone rubbers. The data is used to model the silicone materials in SolidWorks Simulation study.

3.6.1 Strain Range of the Silicone Materials

In order to understand the strain range for the silicone materials testing, initial estimation was conducted in SolidWorks. Due to the complex silicone bellows-like structures used in this study, a detailed FEA simulation was provided in Chapter 4 to validate the initial estimation.

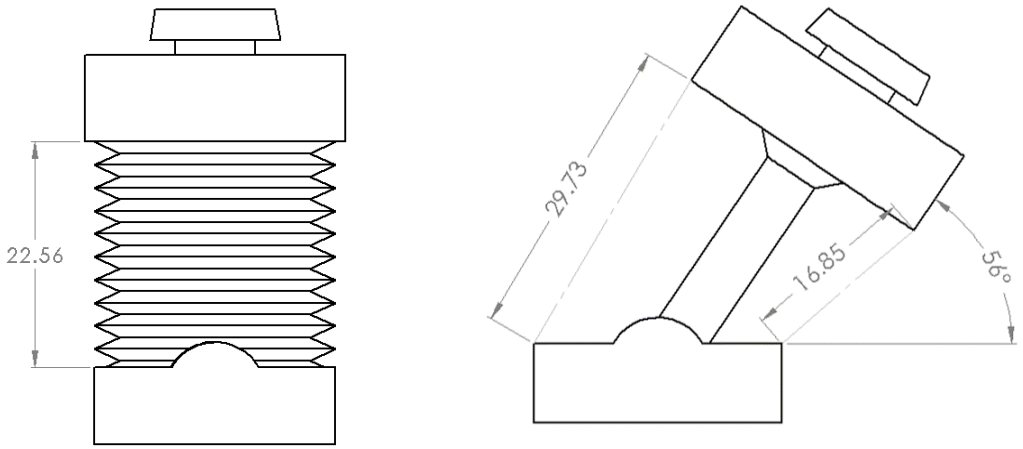

Figure 3.23 2D drawing of a single module. (a) Initial configuration. (b) When the single module is bent 56º.

A 2d drawing of a single module is presented in Figure 3.23. Detailed design will be provided in Chapter 4. The initial height of the bellows-like structure

was measured in SolidWorks ($L_0 = 22.56\,mm$). When a single module was bent to 56º, the distances between top and bottom cap were changed to 29.73 mm and 16.85 mm, respectively (as illustrated in Figure 3.23). Therefore, the strain change of the bellows-like structure can be calculated.

$$\varepsilon_1 = \frac{L_1 - L_0}{L_0} = \frac{29.73 - 22.56}{22.56} = 0.3178 \quad (3.1)$$

$$\varepsilon_2 = \frac{L_2 - L_0}{L_0} = \frac{22.56 - 16.85}{22.56} = 0.2531 \quad (3.2)$$

The maximum strain change for the surface bonding module is estimated as 0.3178. However, when the phase change module is subjected to the bending angle 56º, the strain change of the bellows-like structure is likely greater than 0.3178. (Since there is no rigid joint to restrain the movement of the silicone structure). Therefore, the strain range for silicone materials testing was selected between 0 and 0.5. The estimation in this selection will be validated through FEA simulation in Chapter 4.

3.6.2 Mechanical Properties Testing

Two formulations of silicone rubber (Ecoflex 0030 and Dragon Skin 30) were prepared for the test. Both material consist of liquid A and B part. They were mixed in a 1:1 weight ratio. For this test series, a total of 10 specimens were produced, 5 of each silicone material.

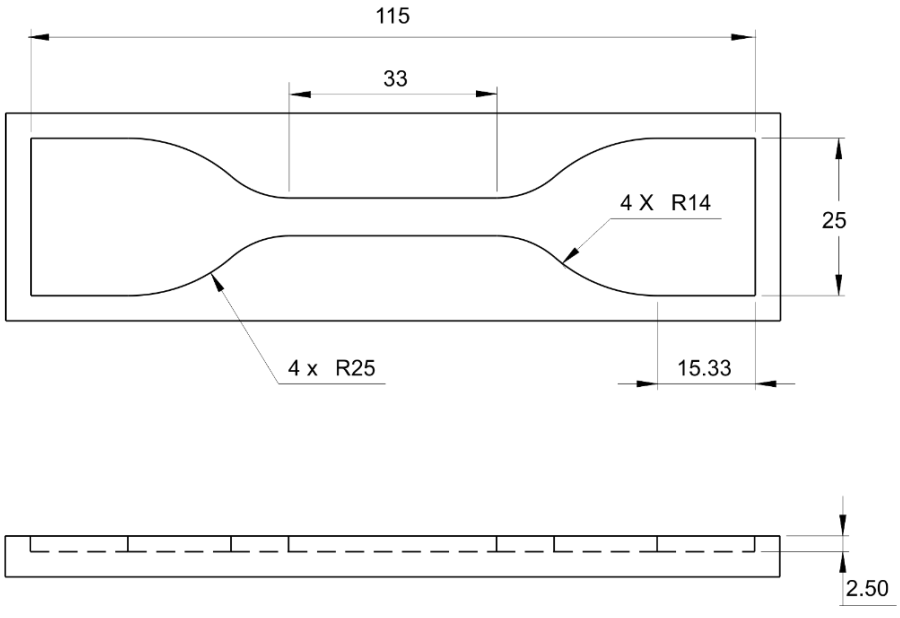

Figure 3.24 2D drawings of the mould used for the fabrication of the specimen for uniaxial tensile tests.

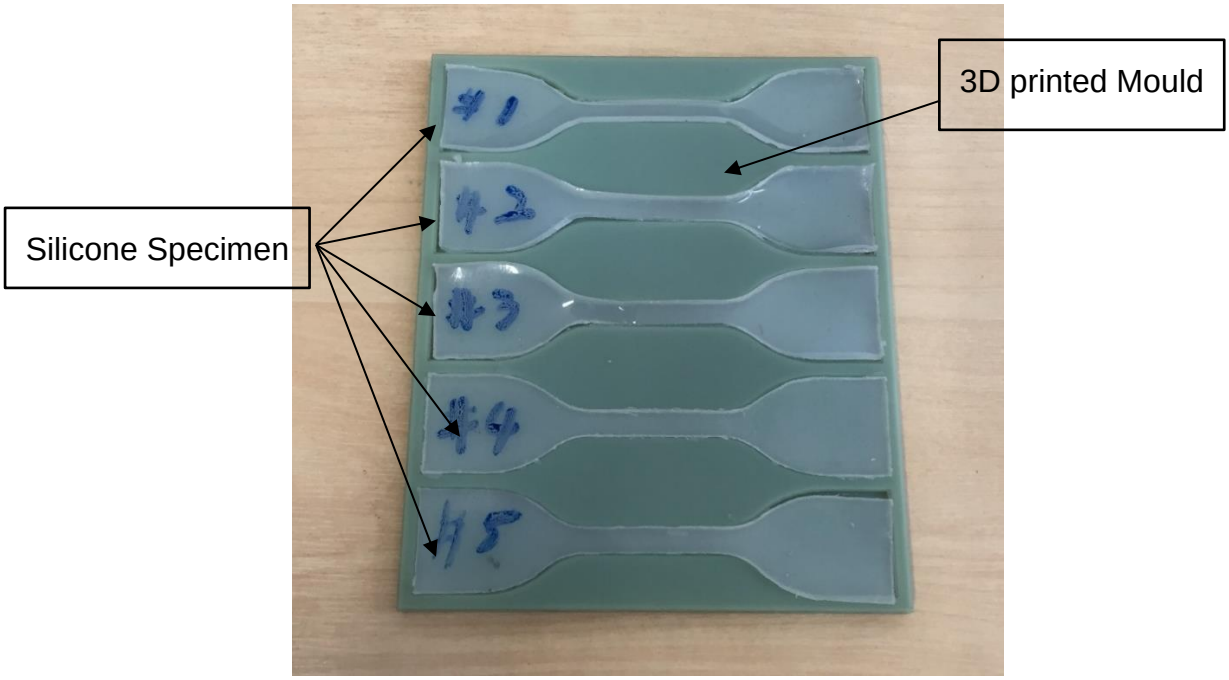

Figure 3.25 The prototype of the mould used for the fabrication of the silicone rubber and five specimens after curing.

The 2D drawings of the mould used for the fabrication of the specimen is shown in Figure 3.24. The mould was made by 3D printer followed by ASTM D412 standard [73]. The mixed materials were poured into the mould and then placed into the vacuum chamber to remove the trapped air bubbles. The testing samples were cured at the room temperature, which was 4 hours for the Ecoflex 0030 [74] and 16 hours for the Dragon Skin 30 [74]. The prototype of the mould and the cured silicone specimens were illustrated in Figure 3.25.

The uniaxial tensile test is a standardised approach for determining the mechanical properties of materials. The strain rate dependent behaviour of the silicone materials was first investigated. To the best of author's knowledge, there is no design requirement regarding angular/bending velocity of a snake-arm manipulator for the restricted environment and human-safe application. Assuming each joint can achieve angular velocity 0.6 rad/s, the time required to rotate to the designed bending angle 56° can be estimated below:

$$t = \frac{\theta}{\omega} = \frac{\frac{56 \times 2\pi}{360}}{0.6} \approx 1.6s \tag{3.3}$$

The maximum strain change was estimated in Section 3.6.1; thus, the strain rate of the proposed design can be calculated as:

$$\varepsilon(t) = \frac{0.3178}{1.6} \approx 0.2\ s^{-1} \tag{3.4}$$

In order to achieve the designed strain rate, test speed 100 mm/min, 200 mm/min, 300 mm/min, 400 mm/min, and 500mm/min was selected. Based on the test results generated by Mecmesin testing machine (see Figure 3.26), strain rate of each testing speed was calculated. The result shows that the strain rate of 500 mm/min testing speed for Ecoflex 0030 and Dragon Skin 30 (0.1891 s^{-1} and 0.1987 s^{-1}, respectively) are closed to achieve the designed strain rate 0.2 s^{-1}.

Final tensile testing was conducted on 5 silicone stripes, using a Mecmesin tensile testing machine with a 10 N load cell, at speed 500 mm/min, where the top and bottom parts of the samples were clamped using force grips. The experimental setup is shown in Figure 3.26. The pulling direction is illustrated in the figure as a blue arrow.

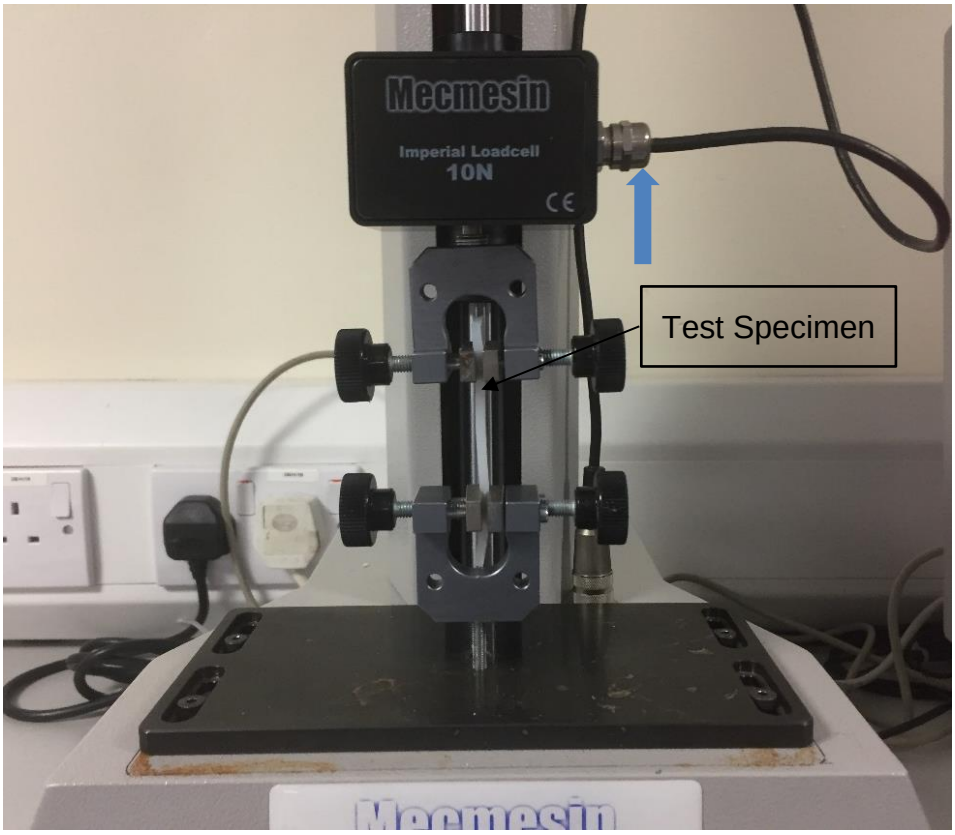

Figure 3.26 Experimental setup for standardised uniaxial tensile test of silicone rubber.

The test results are illustrated in Figure 3.27 and Figure 3.28. Five trials were conducted. The average stress and strain values were plotted in the figure. Experimental data obtained from testing speed 500 mm/min were therefore used to conduct the hyperelastic models to represent accurate material behaviours.

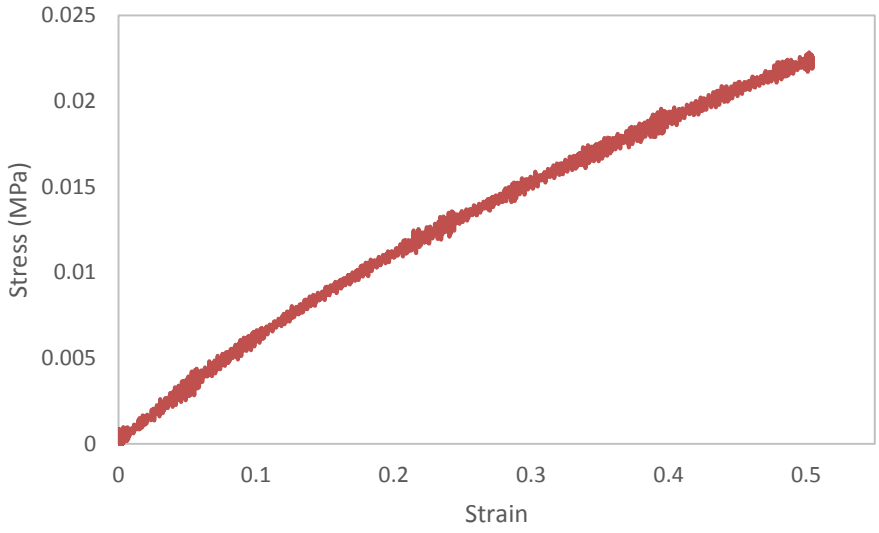

Figure 3.27 Stress vs strain curves of Ecoflex 0030. The test samples were subjected to the test speed 500mm/s.

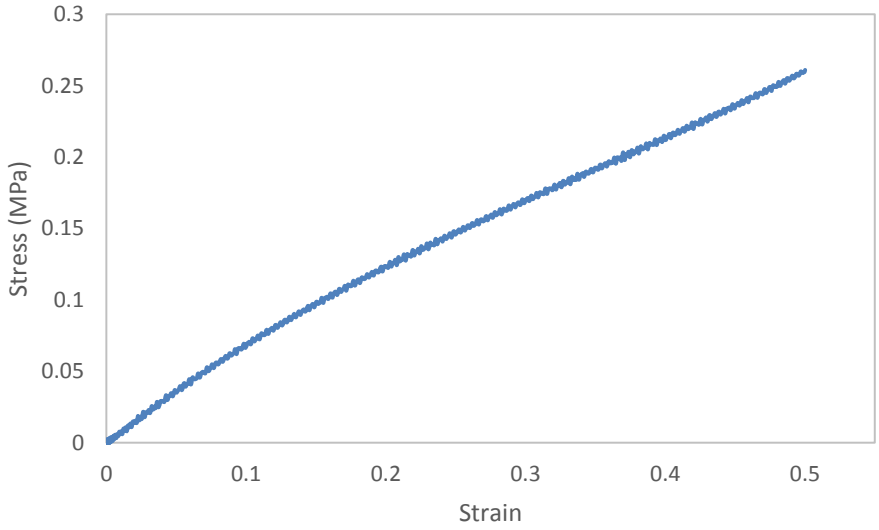

Figure 3.28 Stress vs strain curves of Dragon Skin 30. The test samples were subjected to the test speed 500mm/s.

3.6.3 Hyperelastic Material Models

The stress-strain relationship of silicone rubbers can be described as non-linear, isotropic, incompressible and generally independent of strain rate [72]. They are capable of undergoing large deformation, can be applied in various applications. However, this requires an accurate representation of material behaviours. Unfortunately, the only data which are available from manufacture are limited to tensile strength, cure time and Shore hardness. This has made impossible to model material in linear Finite Element Analysis, which requires a constitutive material law to describe the material. Hyperelastic material

models provide the means to describe the stress-strain behaviour of these materials [75].

Hyperelastic models representing the mechanical behaviour of the silicone rubber materials can be expressed in terms of strain energy potential *W* [76]. The strain energy potential *W* can be either a function of the principal stretch ratios λ_i, or a function of the strain invariants I_i [77].

$$W = W(\lambda_1, \lambda_2, \lambda_3) \tag{3.5}$$

Or

$$W = W(I_1, I_2, I_3) \tag{3.6}$$

There are stretch ratios λ_1, λ_2 and λ_3, which provide a measure of the deformation. The stretch ratio [77] is defined as,

$$\lambda = \frac{L}{L_0} = 1 + \varepsilon_E \tag{3.7}$$

Where ε_E is the engineering strain. Incompressible elastomer experienced a stretch ratio λ_i in the direction of elongation and zero stress in other directions during tensile test. Therefore, the stretch ratios for incompressible material are given by,

$$\lambda_1 = \lambda \tag{3.8}$$

$$\lambda_2 = \lambda_3 = \frac{1}{\sqrt{\lambda}} \tag{3.9}$$

The three strain invariants are defined as bellow,

$$I_1 = \lambda_1^2 + \lambda_2^2 + \lambda_3^2 \tag{3.10}$$

$$I_2 = \lambda_1^2\lambda_2^2 + \lambda_2^2\lambda_3^2 + \lambda_3^2\lambda_1^2 \tag{3.11}$$

$$I_3 = \lambda_1^2\lambda_2^2\lambda_3^2 \tag{3.12}$$

For incompressible elastomer,

$$I_3 = \lambda_1^2\lambda_2^2\lambda_3^2 = 1 \tag{3.13}$$

Several hyperelastic material models, such as Neo-Hookean, 3-term Mooney-Rivlin model, 5-term Mooney-Rivlin model, 3-term Yeoh model, 2-term Ogden model, and Arruda-Boyce model were used in this study (see Table 3.5) to describe the strain energy. The experimental tensile test data were substituted into each of the models to determine the hyperelastic parameters. The sum of square errors (*sse*) was used as one of the indicators to determine the most appropriate model for silicone rubber materials [78].

Table 3.5 Incompressible Hyperelastic Strain Energy Functions [78] Used in this Research.

Hyperelastic Model	Incompressible Strain Energy Function
Neo-Hookean	$W = C_{10}(I_1 - 3)$
3-term Mooney-Rivlin	$W = C_{10}(I_1 - 3) + C_{01}(I_2 - 3) + C_{11}(I_1 - 3)(I_2 - 3)$
5-term Mooney-Rivlin	$W = C_{10}(I_1 - 3) + C_{01}(I_2 - 3) + C_{11}(I_1 - 3)(I_2 - 3) + C_{20}(I_1 - 3)^2 + C_{30}(I_1 - 3)^3$
3-term Yeoh	$W = C_{10}(I_1 - 3) + C_{20}(I_2 - 3)^2 + C_{30}(I_3 - 3)^3$
2-term Ogden	$W = \sum_{i=1}^{2} \frac{u_i}{\alpha_i}(\lambda_1^{\alpha_i} + \lambda_2^{\alpha_i} + \lambda_3^{\alpha_i} - 3)$
Arruda-Boyce	$W = \mu \sum_{i=1}^{5} \frac{c_i}{\lambda_L^{2i-2}}(I_1^i - 3^i), c_1 = \frac{1}{2}, c_2 = \frac{1}{20}, c_3 = \frac{11}{1050}, c_4 = \frac{19}{7050}, c_5 = \frac{519}{673750}$

3.6.4 Test Results

Experimental data, as shown in Figure 3.29 and Figure 3.30, were fitted to the hyperelastic models to determine the parameters for hyperelastic models. The results are listed in Table 3.6.

Table 3.6 Parameters of Hyperelastic Models for Ecoflex 0030 and Dragon Skin 30**.**

Hyperelastic Model	Parameters	Ecoflex 0030	Dragon Skin 30
Neo-Hookean	C_{10}	0.0107	0.1210
	sse	2.1359e-04	0.0088
3-term Mooney-Rivlin	C_{10}	0.0056	0.0194
	C_{01}	0.0063	0.1150
	C_{11}	9.7302e-04	0.0318
	sse	3.6610e-06	0.0010
5-term Mooney-Rivlin	C_{10}	0.0041	0.1436
	C_{10}	0.0079	-0.0180

	C_{11}	0.0194	-0.0731
	C_{20}	-0.0074	0.0758
	C_{30}	-0.0108	-0.0605
	sse	2.7106e-06	5.2669e-05
3-term Yeoh	C_{10}	0.0109	0.1202
	C_{20}	2.2204e-14	2.2204e-14
	C_{30}	-4.2446e-04	0.0018
	sse	8.5719e-05	0.0073
2-term Ogden	μ_1	-0.0020	-220.7030
	α_1	-6.9180	-0.0023
	μ_2	0.0211	0.0015
	α_2	1.6224	9.8271
	sse	3.0485e-06	3.9064e-04
Arruda-Boyce	μ	0.0214	0.2307
	λ_m	8.0448e+03	3.8583
	sse	2.1359e-04	0.0084

The MATLAB algorithm (Appendix A) was used to conduct curve fitting of the tensile data. Based on the sum of square (*sse*) values listed in Table 3.6, 5 term Mooney-Rivlin model provided the best fitting. Therefore, 5 term Mooney-Rivlin model was selected to characterise the material properties of Ecoflex 0030 and Dragon Skin 30 in SolidWorks Simulation.

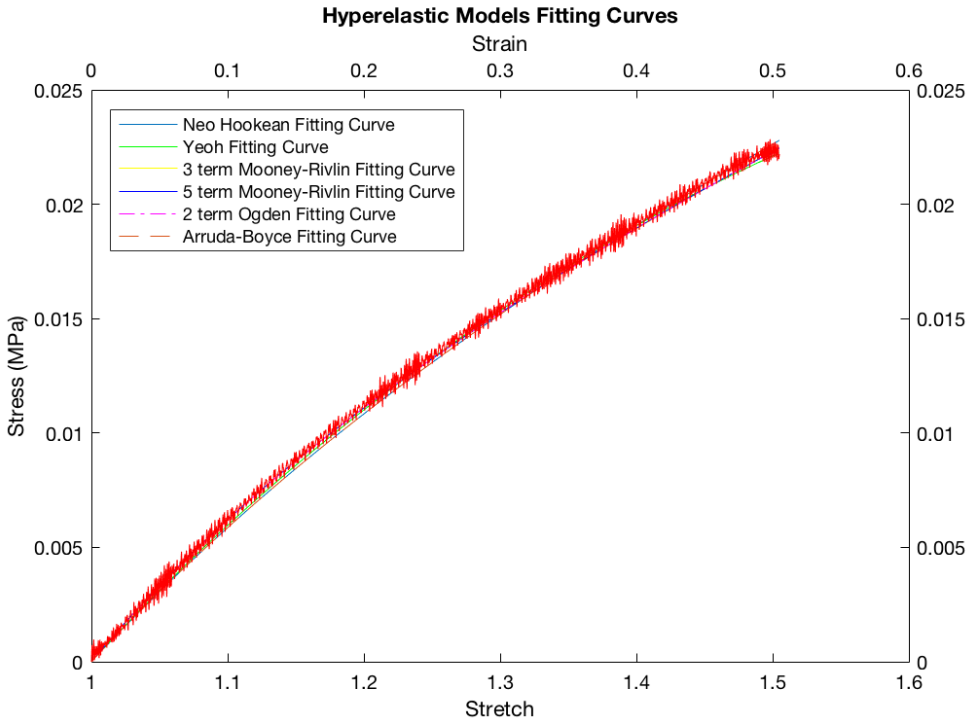

Figure 3.29 Stress-strain curve from uniaxial tensile test of Ecoflex 0030 and hyperelastic model fitting curves.

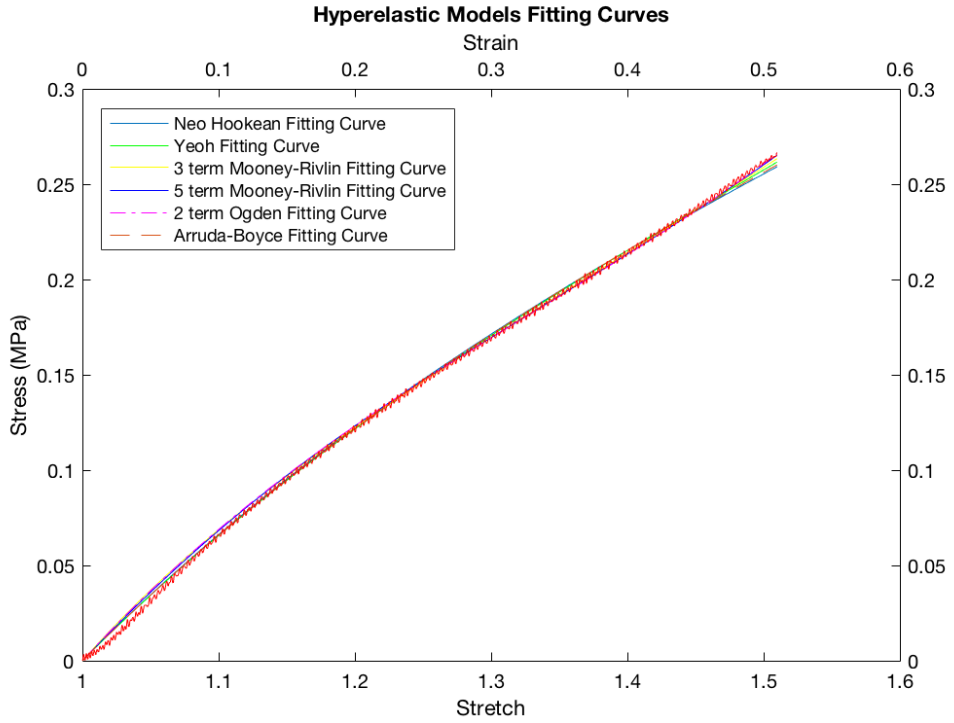

Figure 3.30 Stress-strain curve from uniaxial tensile test of Dragon Skin 30 and hyperelastic model fitting curves.

3.7 Summary

This chapter presents the experimental characterisation of materials used in this research. Four materials, i.e. low melting point solder, hot-melt adhesive, low melting point alloy and granular material, were investigated with the emphasis on the selection and the characterisation of material properties. Hyperelastic models of two formations of silicone rubber (Ecoflex 0030 and Dragon Skin 30) were developed, and the parameters of the models were calculated in the end. The results were summarised in Table 3.7. This chapter provides a systematic approach on how to experimental characterise the properties of the materials. They are the foundations of this research.

Table 3.7 Summary of Materials Selection and Experimental Characterisation results.

Materials	**Selection**	**Results**
LMPS	Field's Metal	• Solidus temperature: 60.2°C. • Temperature influence on bonding strength: Limited • Repeatability: Good
HMA	Low Melting Glue Stick	• Solidus temperature: 50.8 °C • Temperature influence on bonding strength: Significant • Adherent selection: Copper • Repeatability: Weak
LMPA	Lens 136	• Solidus temperature: 56.7°C • Elastic modulus: 2884.96±401.03 MPa
GM	Coarsely ground coffee	• Elastic modulus: 0.1192±0.0010 MPa (atmospheric pressure) 0.2683±0.0428 MPa (100 mmHg) 0.3967±0.009 MPa (180 mmHg)
Silicone Rubber	• Ecoflex 0030 • Dragon Skin 30	• Curve fitting model: 5-term Mooney-Rivlin model

Chapter 4
Design and Analysis of Single Module

This chapter presents the design and analysis of the single module. The module has the capability of modulating stiffness when required. Four materials that were selected and experimentally characterised in Chapter 3 are used to realise the controllable stiffness feature of the single module. Theoretical models and FEA simulations for each design are developed with the emphasis on the bonding torque and bending stiffness. The FEA simulations in this thesis were conducted in SolidWorks Simulation. Thermal models are developed. Furthermore, theoretical response time was estimated at the end.

4.1 Introduction

This chapter aims to develop controllable stiffness modules for tendon-driven self-supporting snake-like manipulator. Three wires are passed down the length of the snake-like manipulator to steer the tip. Stiffness modulation of the snake-like manipulator will be achieved through altering physical properties of the materials at each module.

Two design principles, as illustrated in Table 4.1, are proposed to create controllable stiffness modules:

Table 4.1 Proposed Materials and Design Principles.

Design Principles	**Proposed Materials**
Bonding between surfaces	• Low melting point solder (LMPS) • Hot-melt adhesive (HMA)
Phase change materials	• Low melting point alloy (LMPA) • Granular material (GM)

The materials characterised in Chapter 3 need to be incorporated into a module to be exploited by a snake-like manipulator. This chapter details the mechanical design of the single modules. Theoretical models of the bonding torque and FEA simulations on the bending stiffness of each modules are developed. Thermal models are presented as well.

4.2 Design and Analysis of Surface Bonding Modules

4.2.1 Mechanical Design of Single Modules

The proposed surface bonding module consists of a soft silicone structure and a thermally activated locking mechanism mounted on a rigid joint. Significant compliance is achieved through soft silicone structure. LMPS and HMA are used to design the locking mechanism that can be employed by the rigid joint. One degree of freedom revolute joint and spherical joint are developed in this research. The joint can be selectively locked and unlocked, therefore modulating the stiffness of the module. Details of the design are described below.

4.2.1.1 Revolute Joint

One degree of freedom revolute joint was developed in the initial study to prove the design concept. Figure 4.1 illustrates a CAD model of the revolute joint that employs LMPS- and HMA-based locking mechanism. The dimensions are illustrated in the figure. The module consists of a silicone bellows-like structure, a thermally activated locking mechanism, and a rigid revolute joint. It can be steered by two tendons; the guided tendon hole is shown in Figure 4.1.

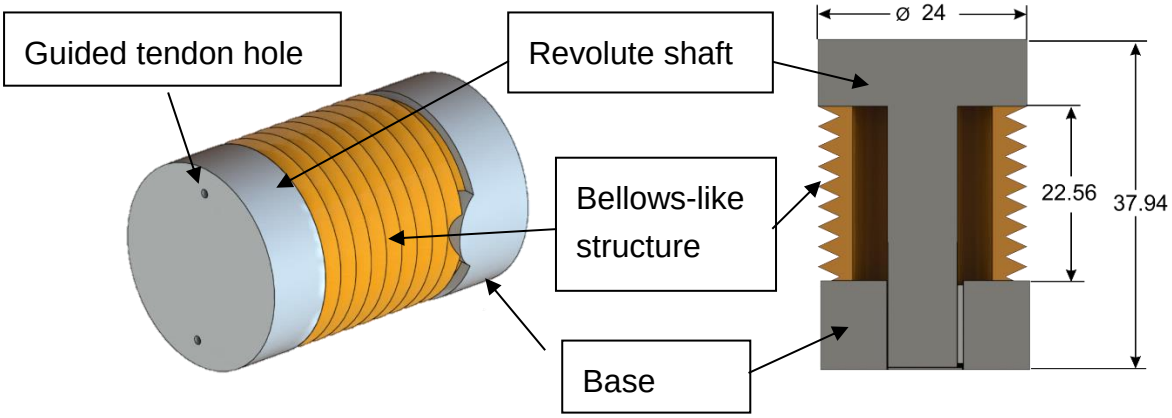

Figure 4.1 CAD model of LMPS- and HMA-based single module. The components and dimension of the module is illustrated in the figure.

The locking mechanism, as shown in Figure 4.2, is composed of a layer of bonding material (LMPS or HMA) sandwiched between two copper tapes. The heating element is placed behind the copper tape. Resistance wires were used to activate the bonding materials. They were wound and closely attached to a copper tape. The silicone bellows-like structure can be used to isolate the heat and prevent potential damage to the working environment. The prototype is presented in Figure 4.3.

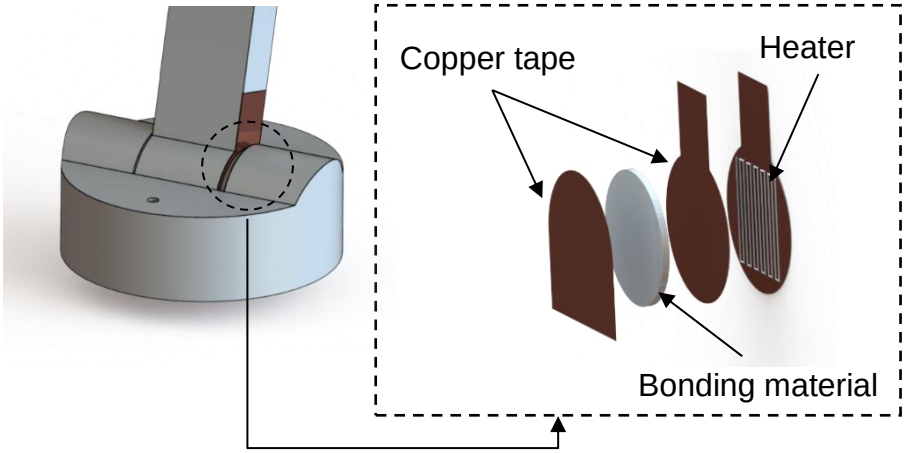

Figure 4.2 CAD model of thermally activated lockable mechanism. The bonding material in the figure represents LMPS or HMA.

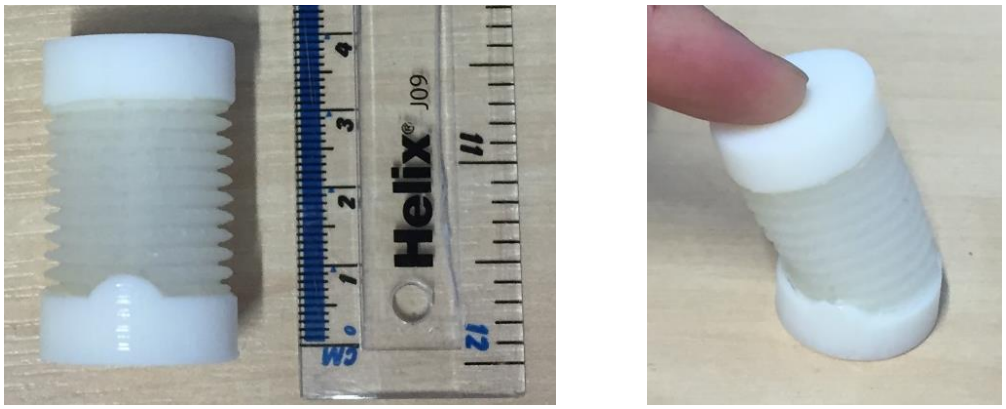

Figure 4.3 The prototype of LMPS- and HMA-based single module.

The rigid revolute shaft (see Figure 4.1) is inserted into the base through a snap-fit method, resulting in an angle range of 56º. Snap-fit design is among the most rapid and easy assembly methods. It eliminates the separate fasteners to simplify manufacturing costs [79, 80]. Ball and socket snap-fit method was used to design the revolute joint, as shown in Figure 4.4 and Figure 4.5. D_G represents the diameter of the ball section and D_k is the opening diameter of the socket.

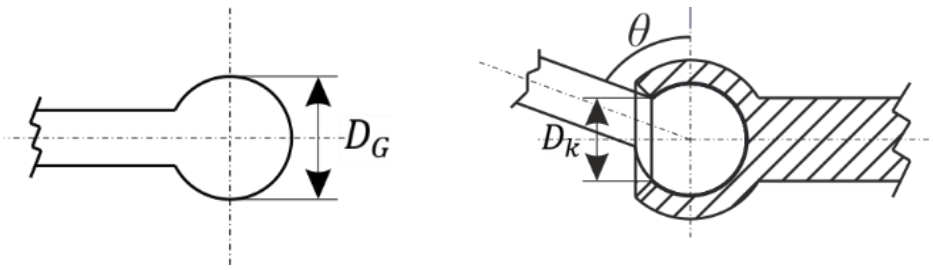

Figure 4.4 Ball and socket snap-fit design.

For the ball section to push into the socket, the undercut depth *H* must be overcome by expanding the hub of the socket. Because of the diameter change, the hub of the socket is deformed as follow.

$$\varepsilon_{elongation} = \frac{D_G - D_k}{D_k} \cdot 100\% = \frac{H}{D_k} \cdot 100\% \qquad 4.1$$

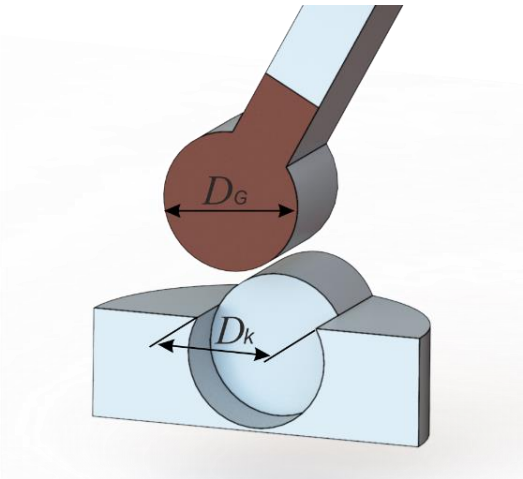

Figure 4.5 Illustration of the diameter of ball section $\mathrm{D_G}$ and the diameter of the socket $\mathrm{D_k}$ in the first prototype of the single module.

Assuming the diameter of the ball section D_G is 10 mm, elongation of the material (VeroWhitePlus) can be obtained from manufacturer ($\varepsilon_{elongation} = 10\%\sim25\%$), the opening diameter of the socket can be obtained from the equation,

$$D_k = \frac{D_G}{\varepsilon_{elongation} + 1} = 8\sim9.09\ \mathrm{mm} \qquad 4.2$$

The simplest way to determine the opening diameter of the socket D_k is through experiments. The experimental setup was shown in Figure 4.6.

Four rigid revolute joints with bending angle 54°, 56°, 58° and 60° were 3D printed to determine the optimal opening diameter of the socket D_k. A hand-held scale was used to record the force that separates the ball section from the socket. Five trials were conducted on each joint. The results are presented in Table 4.2. Without causing any damage to the rigid joints, the largest pull-out force was found to be 81.7±12.3 N. Therefore, the optimal opening diameter of the socket was selected to be 8.72 mm.

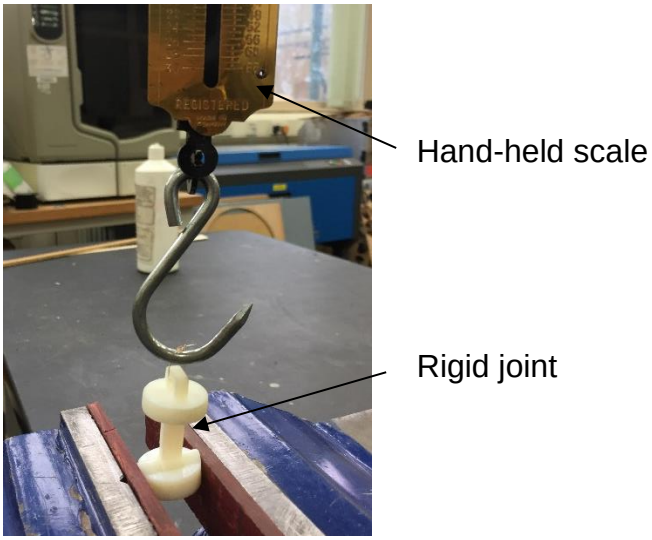

Figure 4.6 Experimental setup for determining optimal opening diameter of the socket.

Table 4.2 Numerical Results of Optimal Opening Diameter Experiments.

Bending Angle (θ)	**Diameter** D_k (mm)	**Pull-out Force** F_2 (N)	**Joint Damage**
54°	8.89	48.8±2.5	NO
56°	8.72	81.7±12.3	NO
58°	8.58	83.5±6.1	YES
60°	8.36	94.7±19.9	YES

4.2.1.2 Spherical Joint

The revolute joint of the single module has been successfully validated through a series of experiments (see Chapter 6). The concept of using LMPS and HMA in the development of controllable stiffness element has been demonstrated. However, one degree of freedom revolute joint inherently lacks dexterity, a spherical joint that can employ LMPS- and HMA-based locking mechanism is developed under this context.

CAD model of the single module, as shown in Figure 4.7, is composed of a rigid spherical joint, a thermally activated locking mechanism and a silicone bellows-like structure. The bonding material (LMPS or HMA) is sandwiched between two copper tapes. Each copper tapes are glued on the surfaces of the spherical joint. The resistive wires are used to activate the bonding material. They are wound and attached to a copper tape. Figure 4.8 presents the prototype of the single module.

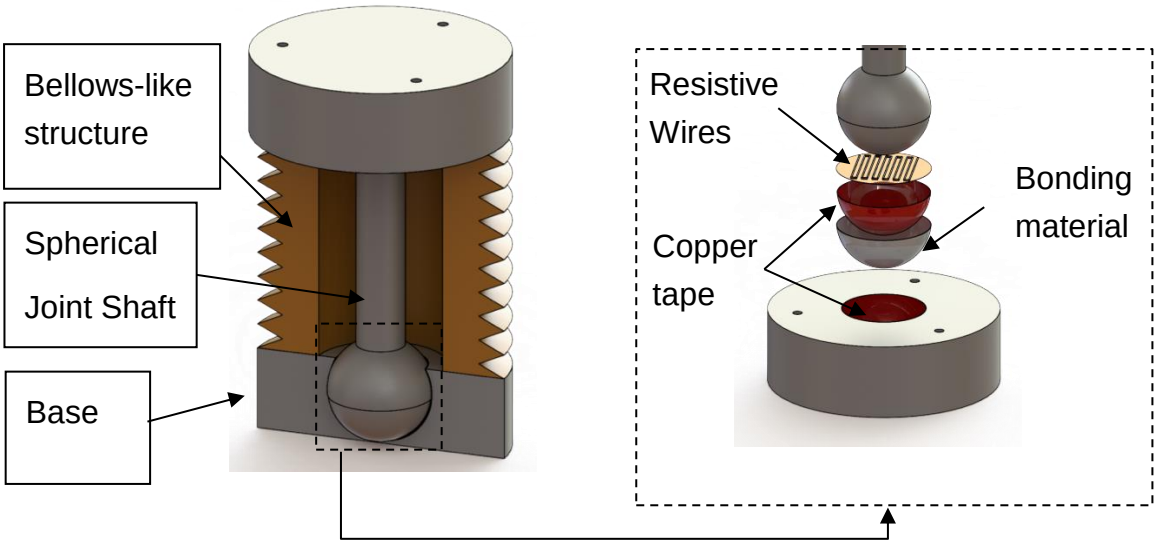

Figure 4.7 CAD model of LMPS- and HMA-based single module is shown on the LEFT. The locking mechanism is illustrated on the RIGHT.

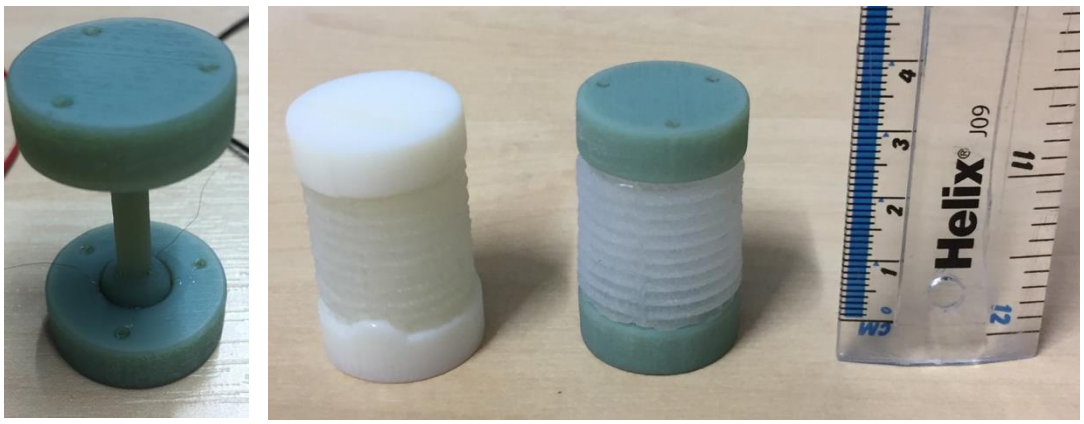

(a) (b)

Figure 4.8 The prototype of the single module consists of the spherical joint. (a) Spherical joint. (b) Fully assembled prototype. Revolute joint-based module is shown on the left, the spherical joint-based single module is shown in the middle.

4.2.2 Analysis of Surface Bonding Single Modules

4.2.2.1 Bonding Torque

1) Revolute Joint: The proposed single module can be used to construct a snake-like manipulator. Thanks to the LMPS- and HMA-based locking mechanism, the manipulator is capable of controlling the stiffness of the selected segments. To determine the torque required to lock the manipulator at an arbitrary position, an extreme configuration was considered. Such extreme configuration occurs when the manipulator is placed in the cantilevered position.

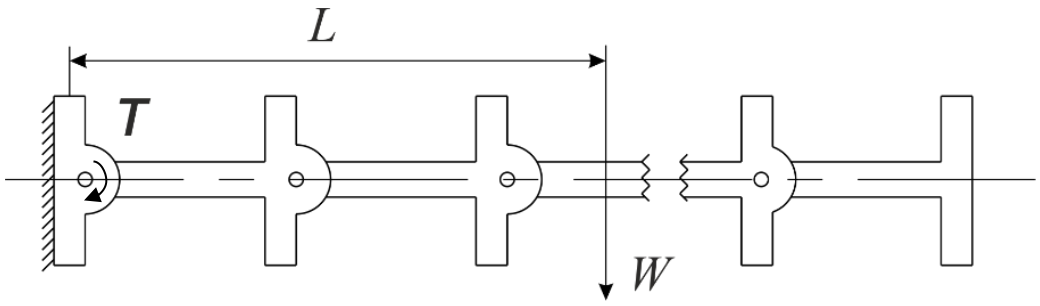

Figure 4.9 Robotic manipulator consists of rigid joint in the cantilevered configuration.

The largest torque is imposed on the area of proximal joint, as shown in Figure 4.9. Equation shows the relation between torque (*T*) and weight (*W*) of the manipulator via distance (*L*) between fix end and weight centre.

$$T = W \cdot L \tag{4.3}$$

For LMPS- and HMA-based locking mechanism, shear torsional model is applied. In order for manipulator to be placed in the cantilevered position, shear bonding torque (T_{lock}) that LMPS or HMA can offer should be larger than the torque imposed by the weight of the manipulator.

$$T_{lock} > T = W \cdot L \tag{4.4}$$

Figure 4.10 represents the bonding area on the locking mechanism of the first prototype of the single module. The locking force (F_{lock}) that the bonding material provides can be calculated by the shear strength (τ) of the bonding material and bonding area (*A*). Shear strength of LMPS and HMA are obtained from the Chapter 3.

$$dF_{lock} = \tau \cdot dA \tag{4.5}$$

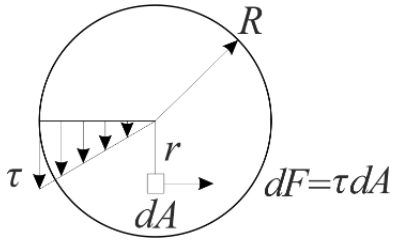

Figure 4.10 Simplified shear torsional model (revolute joint)**.**

The shear strength on the differential elements (dA) generates a moment around the centre of bonding area.

$$dM = r(\tau \cdot dA) \tag{4.6}$$

All these differential moments are equal to the applied bonding torque,

$$\int_A dM = \int_A r(\tau \cdot dA) = T_{lock} \tag{4.7}$$

Where T_{lock} can be obtained by integral in a polar coordinate system.

$$dA = rdrd\theta \tag{4.8}$$

$$T_{lock} = \tau \int_0^{2\pi} \int_0^R r^2 drd\theta = \frac{2\pi}{3}\tau R^3 \tag{4.9}$$

Where *R* is the radius of the bonding area. Given the length and weight of the manipulator, the torque that required to lock the manipulator at arbitrary position can be calculated. Therefore, the minimal radius of the bonding area can be estimated.

2) Spherical Joint: For spherical joint, shear bonding torque is calculated on the spherical surface. Figure 4.11 illustrates simplified torsional model.

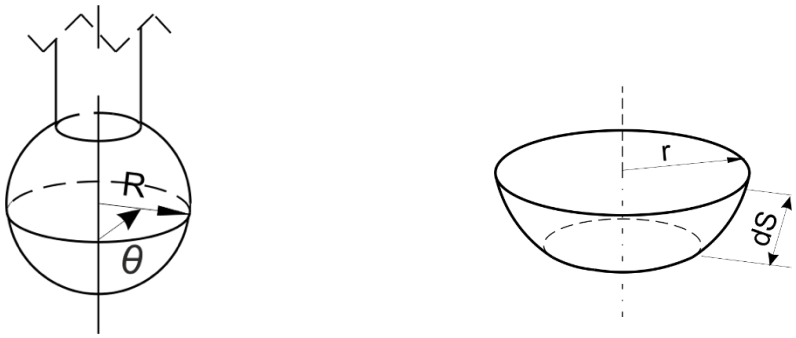

Figure 4.11 Shear torsional model (spherical joint). Bonding area is illustrated on the right.

Shear bonding area element can be calculated as,

$$dA = 2\pi r dS \tag{4.10}$$

where R is the radius of the sphere, *r* ($r = R\sin\theta$) is the radius of the cross-sectional area, and dS represents the arc element ($dS = Rd\theta$).

Shear bonding torque can be written as a function of shear strength of the material τ and rotation angle θ,

$$T_{lock} = 2\pi R^3 \tau \int_0^{\theta} \sin\theta^2 \, d\theta \tag{4.11}$$

This model provides the insight on the design of the radius of the sphere. Shear strength of LMPS ($\tau_{solder} = 1.3666\,\mathrm{MPa}$) and HMA ($\tau_{adhesive} = 1.0713\,\mathrm{MPa}$) have been determined through a series of experiments in Chapter 3. The radius of the bonding area and the radius of the sphere were purposely overdesigned. These parameters are validated through experiments to determine how much weights the manipulator can support

before failure occurs. Numerical results of the shear bonding torque that LMPS and HMA can provide are presented in Table 4.3.

Table 4.3 Numerical Results of Shear Bonding Torque Calculation.

	LMPS-based Module	**HMA-based Module**
Bonding Torque of Revolute Joint (Nmm)	336.75	240.46
Bonding Torque of Spherical Joint (Nmm)	454.73	356.47

4.2.2.2 FEA Simulation on Strain Range

Strain range estimation (see Chapter 3) was first validated in SolidWorks Simulation. The material properties of Ecoflex 0030 were characterised in Chapter 3. 5-term Mooney-Rivlin was selected to model Ecoflex 0030 material, with parameters 0.0041, 0.0079, 0.0194, -0.0074, and -0.0108 (see Figure 4.12). The material properties of the plastic material (VeroWhitePlus) can be found in reference [81].

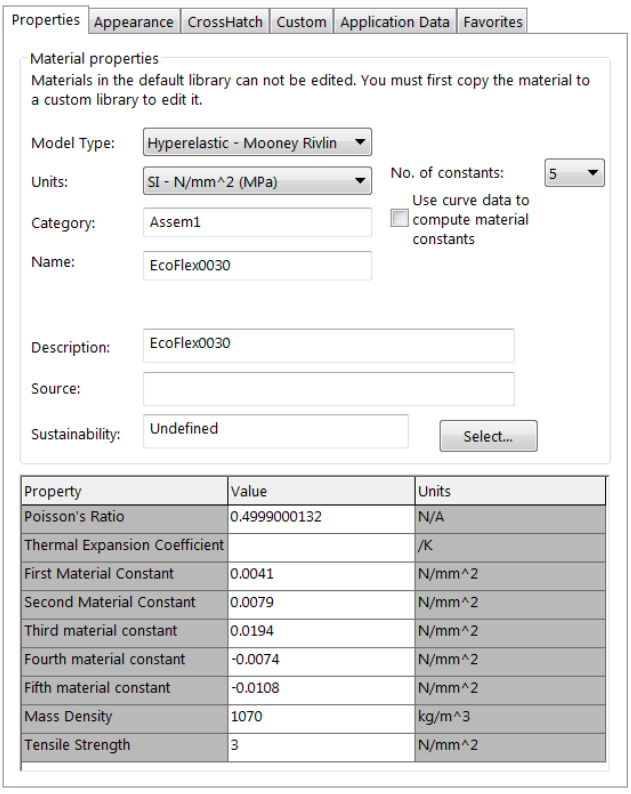

Figure 4.12 Material property of Ecoflex 0030 in SolidWorks.

The single module was cantilevered, the external load was applied to the end-effector of the module. The direction of the force, as shown in Figure 4.13, is parallel to the surface of the end-effector. The simulation result, as illustrated in Figure 4.13, demonstrated the maximum strain is 0.4042 when the surface bonding module is subjected to a bending angle 56^{o}. The maximum strain is within the range of the selected tensile testing strain range (between 0 and 0.5). Therefore, the test is valid.

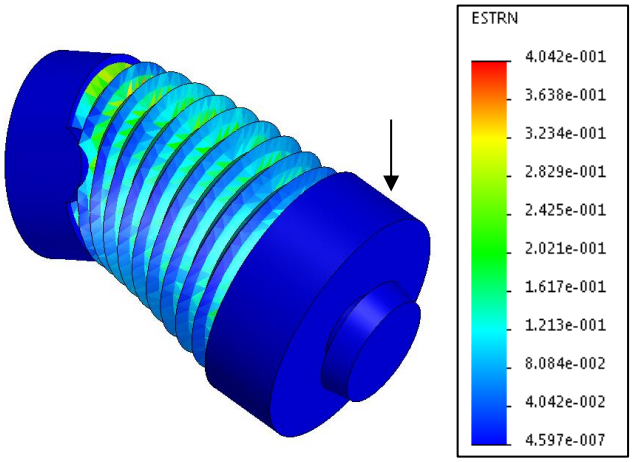

Figure 4.13 Strain range of surface bonding module. Maximum strain is illustrated on the right.

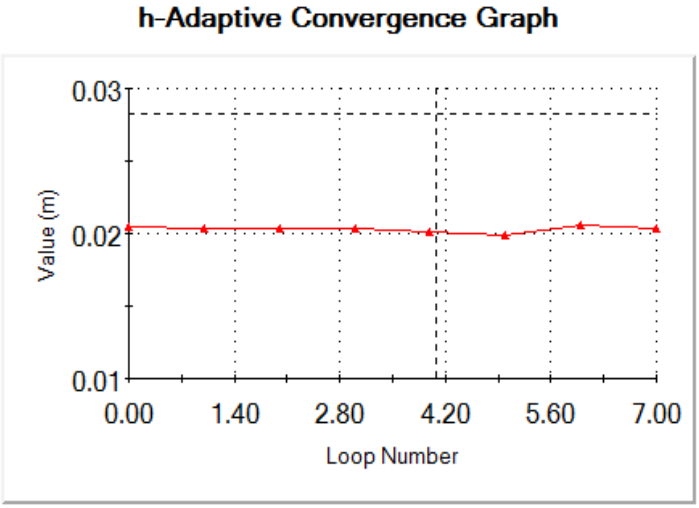

Figure 4.14 Mesh convergence study of the strain range simulation. Maximum resultant displacement is plotted in the figure.

Mesh convergence study was conducted in SolidWorks Simulation. With more elements in the mesh, the solution is more accurate. As with more elements, there are more nodes available for calculating response. However, finding the practical limit where further refinements add no benefit to the solution can be time-consuming. SolidWorks provides h-adaptive option to make the mesh convergence process a little less tedious. Automatic h-adaptive method runs

the study multiple times (loop number). Refines the mesh in critical areas in each loop, reruns the study, until either the target accuracy is achieved or the max specified loops are run. The convergence study result, as demonstrated in Figure 4.14, justifies the accuracy of the simulation results in Figure 4.13.

4.2.2.3 FEA Simulation on Bending Stiffness

Bending stiffness is an important criterion for understanding the force that the single module can support in the thickness direction. It is used in this thesis to evaluate and compare the stiffness change of each design approach.

The bending stiffness is given by,

$$K = \frac{F}{\delta} \tag{4.12}$$

Where *F* is the force applied at the end, and δ is the deflection of the single module.

The following assumptions are made for the simulation of the stiffness of the module: i) When a module is in the locking state, LMPS and HMA design approaches can achieve a complete shape lock. (Complete shape lock is defined as: The bonding materials do not contribute to the deflection of the module. The shaft is assumed to be bonded to the base). ii) When the module is unlocked, the bonding strength that the material can provide is assumed to be zero. The coefficient of friction between shaft and base is assumed to 0.3.

The dimension of the module was given in Section 4.2, the properties of the plastic material (VeroWhitePlus) was provided in reference [81]. 5-term Mooney-Rivlin was used to model the Ecoflex 0030 material. Surface bonding modules (revolute joint and spherical joint) were cantilevered in the simulations. An external load was applied to the end-effector, the direction of the force was illustrated in the Figure 4.15, Figure 4.17, Figure 4.19 and Figure 4.21. The modules were simulated in rigid state as well as in soft state. Mesh convergence studies were conducted by using h-adaptive method provided by SolidWorks. Simulation results on the bending stiffness of the surface bonding modules are provided in Figure 4.16, Figure 4.18, Figure 4.20 and Figure 4.22.

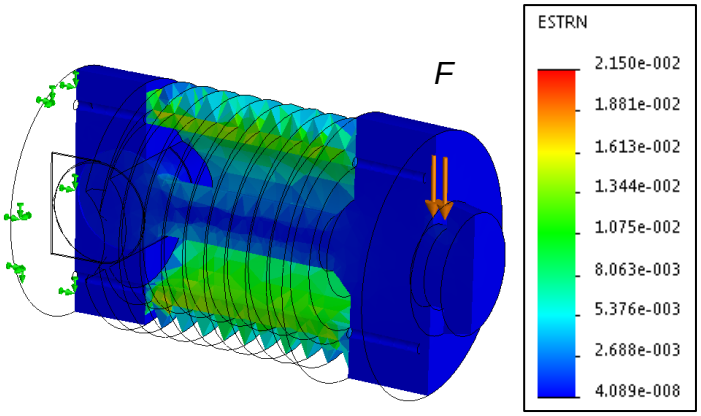

Figure 4.15 FEA model of revolute joint in rigid state. The equivalent strain is shown on the right.

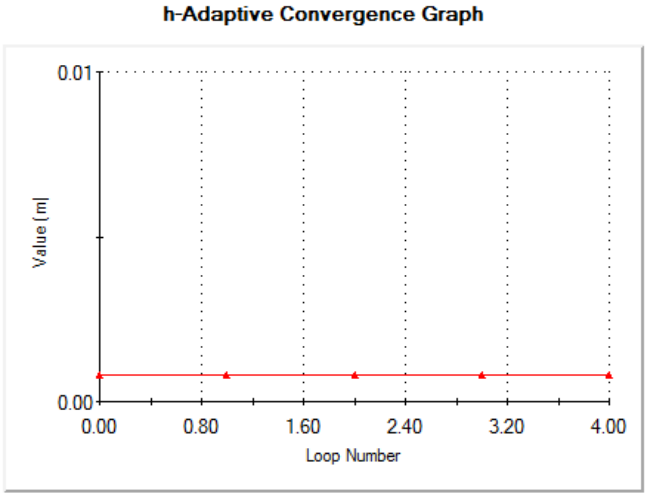

Figure 4.16 Mesh convergence study of revolute joint in rigid state. Maximum resultant displacement is plotted in the figure.

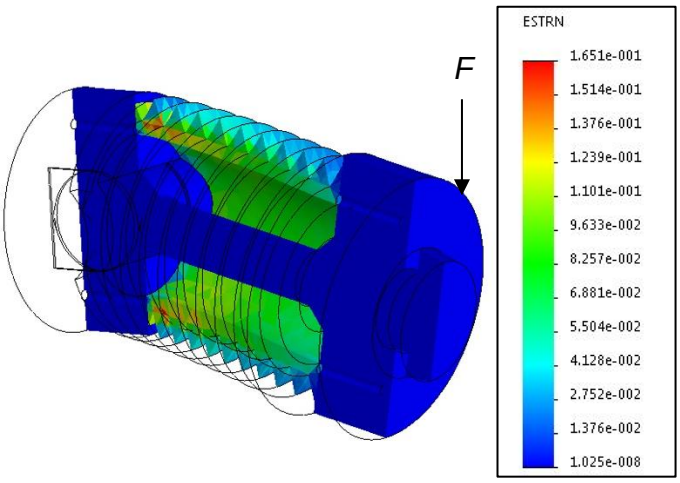

Figure 4.17 FEA model of revolute joint in soft state. The equivalent strain is shown on the right.

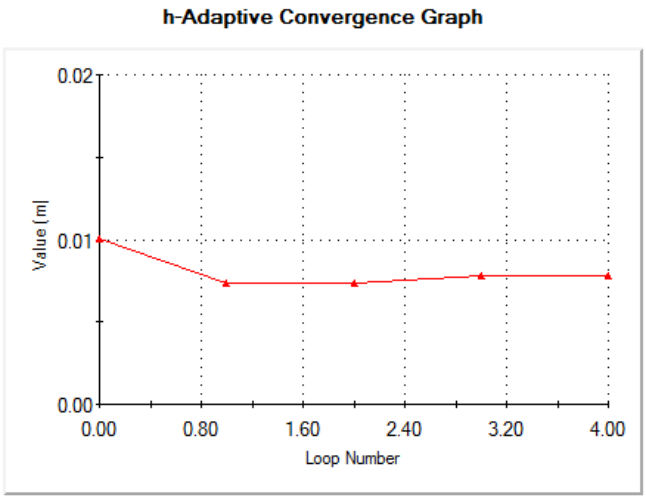

Figure 4.18 Mesh convergence study. Maximum resultant displacement is plotted in the figure.

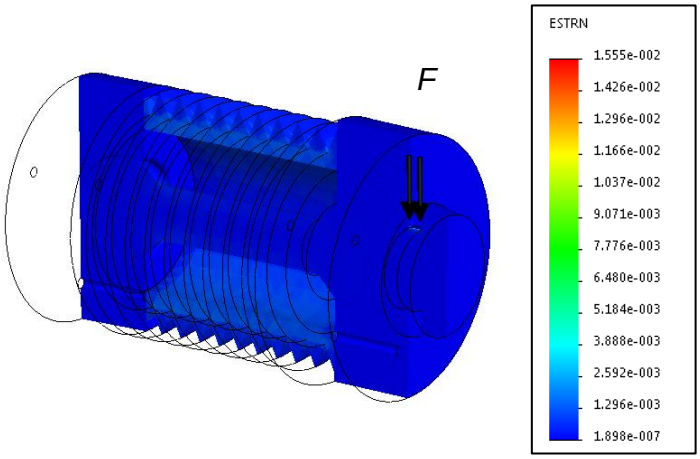

Figure 4.19 FEA model of spherical joint in rigid state. The equivalent strain is shown on the right.

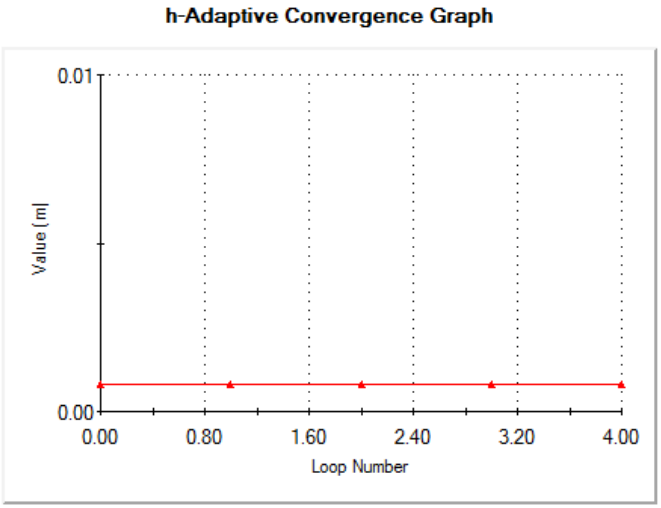

Figure 4.20 Mesh convergence study of spherical joint in right state. Maximum resultant displacement is plotted in the figure.

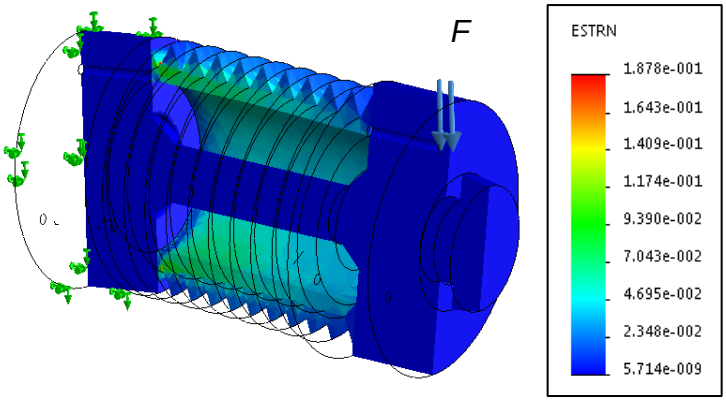

Figure 4.21 FEA model of spherical joint in soft state. The equivalent strain is shown on the right.

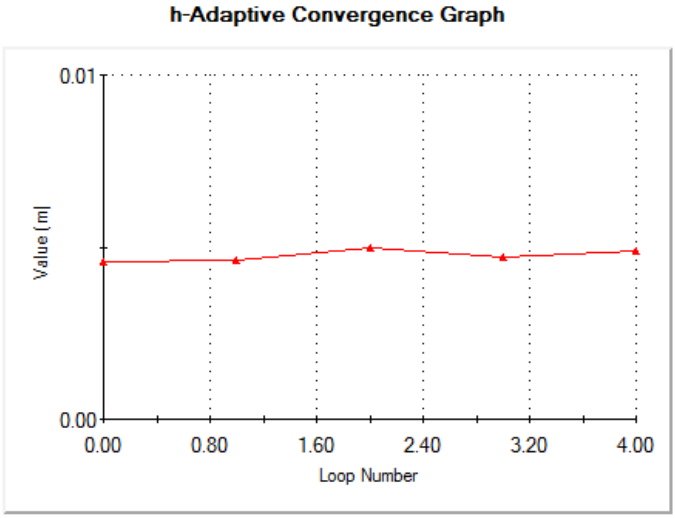

Figure 4.22 Mesh convergence study of spherical joint in soft state. Maximum resultant displacement is plotted in the figure.

The external loads used in the simulations, the displacement results, the maximum strain and the calculated bending stiffness are presented in the Table 4.4.

The results show the maximum equivalent strain for surface bonding modules fall into the tensile testing strain range, the simulations are therefore valid. The theoretical simulations suggest the spherical joint in rigid state has greater bending stiffness than the rational joint. This is due to the difference of cross-sectional area between revolute and spherical joint. Thermally activated spherical joint has greater stiffness change than its counterpart. The simulation results will be validated through experiments in Chapter 6.

Table 4.4 Theoretical Calculation of Bending Stiffness for the surface bonding modules in rigid and soft state.

	Load (N)	**Displacement** (mm)	**Max Strain**	**Bending Stiffness** (N/mm)
Revolute Joint (Rigid)	5.880	0.6742	2.150e-002	8.7214
Revolute Joint (Soft)	0.196	7.291	1.651e-001	0.0269
Spherical Joint (Rigid)	5.880	0.6561	1.555e-002	8.9620
Spherical Joint (Soft)	0.098	5.744	1.878e-001	0.0171

4.3 Design and Analysis of Phase Change Modules

4.3.1 Mechanical Design of Single Module

LMPA and GM are used to develop the phase change single module. The idea is to design soft silicone structure to contain the proposed materials. Since LMPA and GM can transition between solid-like state and fluid-like state, the stiffness of the module is controlled by the state of the embedded materials.

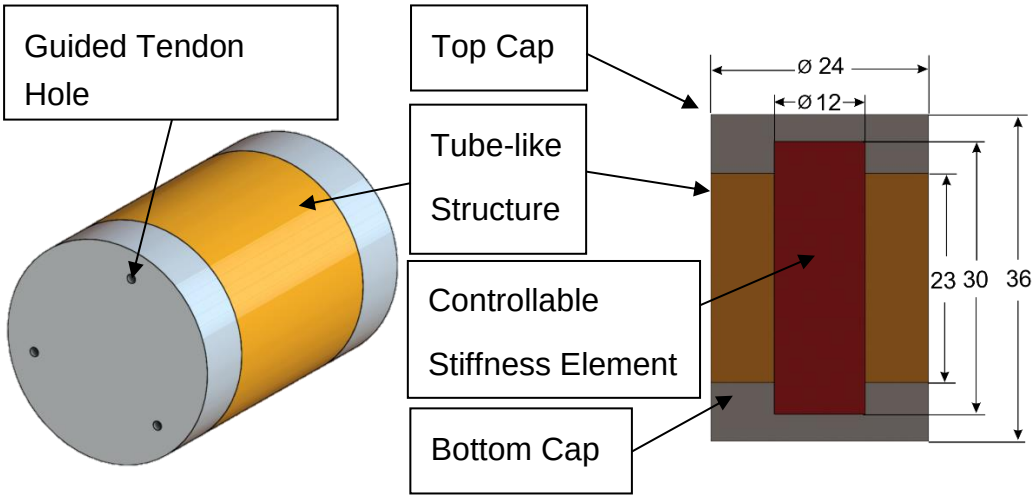

Figure 4.23 CAD model of LMPA- and GM-based single module.

Figure 4.23 shows a CAD model of the single module that was embedded with LMPA or GM. The module is composed of a silicone structure and a

controllable stiffness element. Specifically, the silicone structure consists of three components, top cap, tube-like structure and bottom cap. The tube-like structure was cast out of soft silicone rubber material (Ecoflex 00-30, Smooth on Inc.) to provide compliance of the module. Ecoflex 00-30 was selected due to its high flexibility and the level of softness. The top cap and bottom cap, on the other hand, were fabricated by hard silicone rubber material (Dragon Skin 30, Smooth on Inc.) to provide the rigidity and stability for LMPA or GM during bending. Three tendons are used to steer the module, the guided tendon hole is shown in Figure 4.23. The prototype of the single module is shown in Figure 4.24.

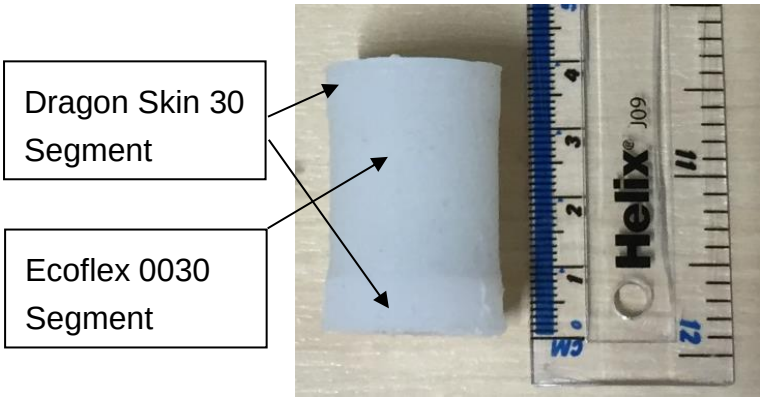

Figure 4.24 The prototype of the single module that embedded with LMPA- or GM-based controllable stiffness element.

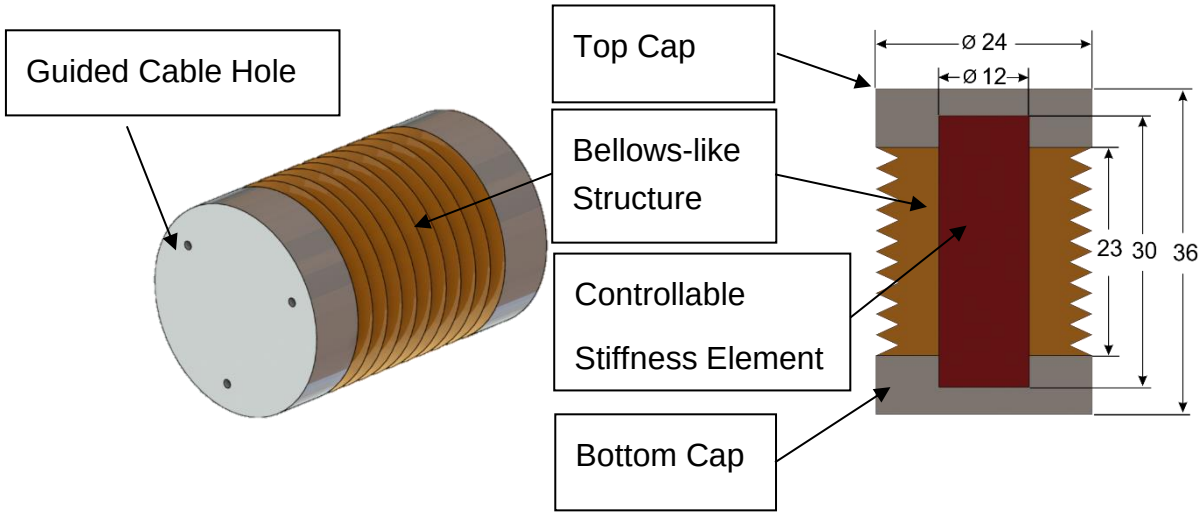

Figure 4.25 CAD model of the single module that embedded with LMPA- or GM-based controllable stiffness element.

The silicone structure should be designed as flexible as possible to maximise the stiffness increase between solid-like state and liquid-like state. Design modification was made to replace a tube-like structure with a bellows-like structure. As shown in Figure 4.25, the modified module consists of top cap,

bellows-like structure, controllable stiffness element and bottom cap. The top and bottom caps were made of Dragon Skin 30, and the bellows-like structure was cast out of Ecoflex 0030. The prototype of the single module is presented in Figure 4.26. LMPA-based single module is shown on the left, GM-based single module is presented on the right.

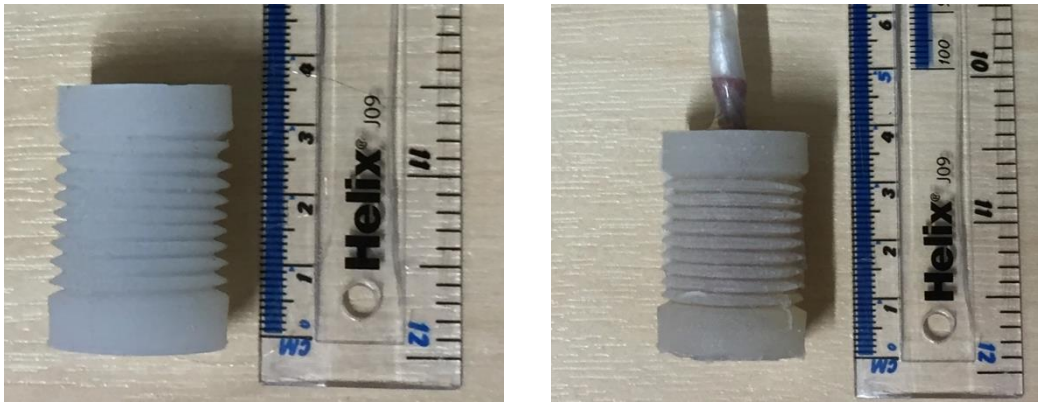

Figure 4.26 The prototype of the single module. LMPA-based single module is shown on the left, GM-based single module is presented on the right.

The modified design was compared with the original design through FEA simulations in SolidWorks. The space occupied by LMPA or GM is assumed to be empty in the simulation. 5-term Mooney-Rivlin was used to model the Ecoflex 0030 and Dragon Skin 30 materials. A series of simulations were carried out for the bending of the single module under different forces. The single modules were cantilevered in the simulations, the direction of the external load was illustrated in the figure. The comparison results are shown in Figure 4.27.

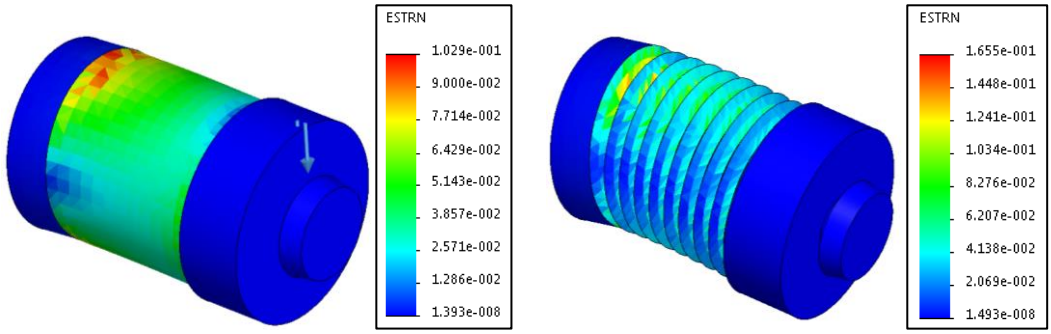

Tube-like Design 0.196N Bending Bellows-like Design 0.196N Bending

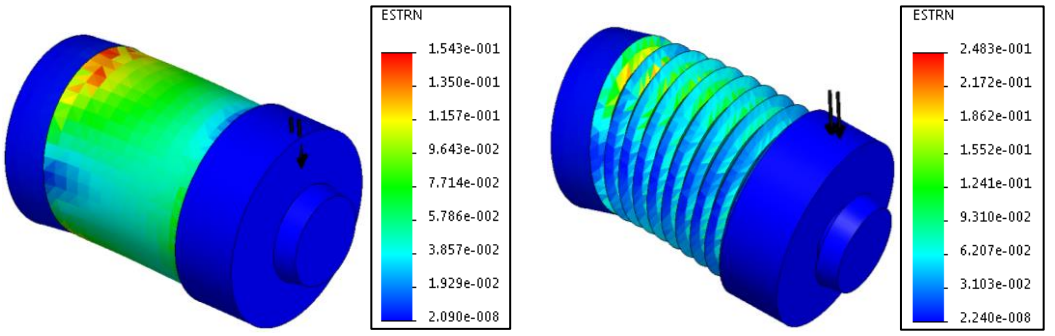

Tube-like Design 0.294N Bending Bellows-like Design 0.294N Bending

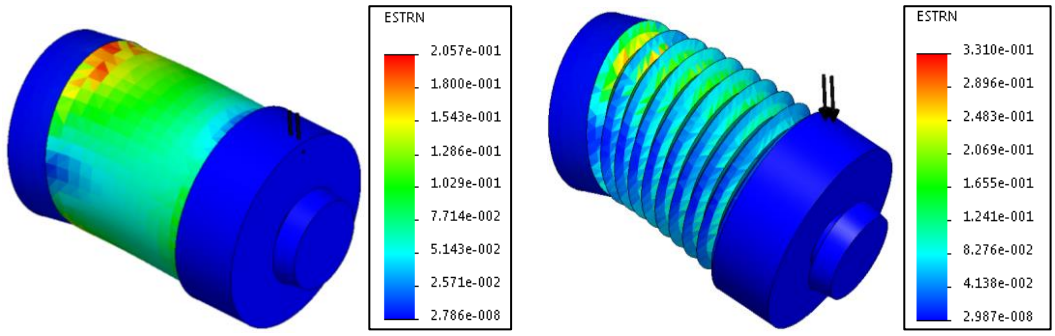

Tube-like Design 0.392N Bending Bellows-like Design 0.392N Bending

Figure 4.27 FEA simulation of the bending of single module under different forces.

The results demonstrate that when two designs subject to the same external load, the bellows-like design has greater magnitude of strain than the tube-like design. One can predict when LMPA or GM in the liquid-like state, the bellows-like design is more flexible than the tube-like design. Therefore, the bellows-like design is used for the construction of the single module.

4.3.2 Design Optimization of the Bellows-like Structure

Design parameters of the bellows-like structure, as illustrated in Figure 4.28 (b), include outer diameter of the bellows-like structure (D=24mm), the inner diameter (d=12mm), the diameter of the guided cable hole, the smallest distance between the cable hole and bellows-like structure (b=1.2mm and c=1mm), and the number of the pitch. The smallest distance between cable hole and bellows-like structure was too small to be altered. Outer diameter was designed as the same diameter of surface bonding modules. Inner diameter was selected to sufficiently contain the controllable stiffness element. Therefore, the number of the bellows (pitch) was selected to be optimized. Design optimisation of the bellows-like structure was carried out in SolidWorks Simulation. The material bellows-like structure was selected as Ecoflex 0030, the top and bottom cap was used as Dragon Skin 30 material. External load (F) was applied on the end effector of the single module, parallel to the top

surface of the module. The direction of the force was illustrated in Figure 4.29 (a). The simulation result is shown in Figure 4.29 (a). The experimental setup and bending angle illustration are presented in Figure 4.29 (b). The numerical optimisation result, as presented in Table 4.5, shows that as the number of the bellows increases, the bending angle increases as well. However, as the number of the bellows increases, the distance of the pitch decreases. This will impose the difficulty of 3D printing the mould and casting the silicone bellows-like structure. Due to the consideration between maximising the number of the bellows and the difficulty of manufacture, the total number of bellows was selected to be 10.

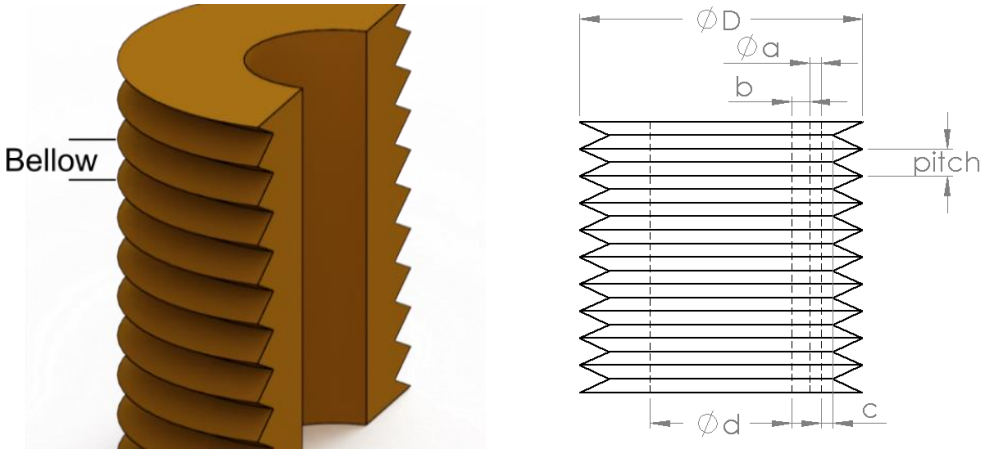

(a) (b)

Figure 4.28 Illustration of the bellows-like structure. (a) 3D model of the bellows-like structure. (b) Design parameters of the bellows-like structure.

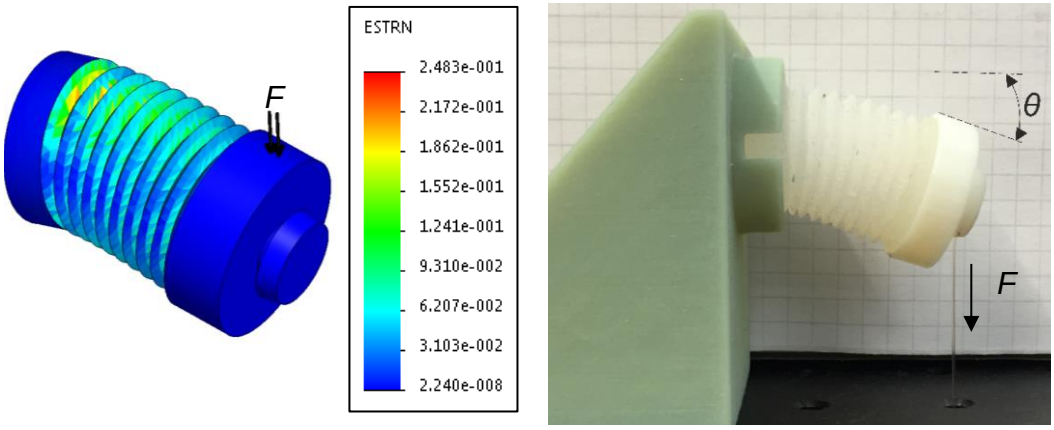

(a) (b)

Figure 4.29 (a) FEA simulation result (number of bellows 10). (b) Experimental setup and bending angle illustration (number of bellows 10).

Table 4.5 Optimization Results of Total Number of Bellows.

Number of Bellows	FEA Results	Experimental Results
8	25.31°	24.18±0.71°
9	25.55°	24.78±0.39°
10	25.78°	25.57±0.41°
11	25.93°	27.01±0.23°
12	26.20°	27.94±0.23°

4.3.3 Analysis of Bending Stiffness for Phase Change Single Module

4.3.3.1 Strain Range

Strain range estimation (see Chapter 3) was validated in SolidWorks Simulation. The material properties of the silicone materials were characterised in Chapter 3. 5-term Mooney-Rivlin was selected to model the material properties of Ecoflex 0030 (see Figure 4.12) and Dragon Skin 30 (see Figure 4.30).

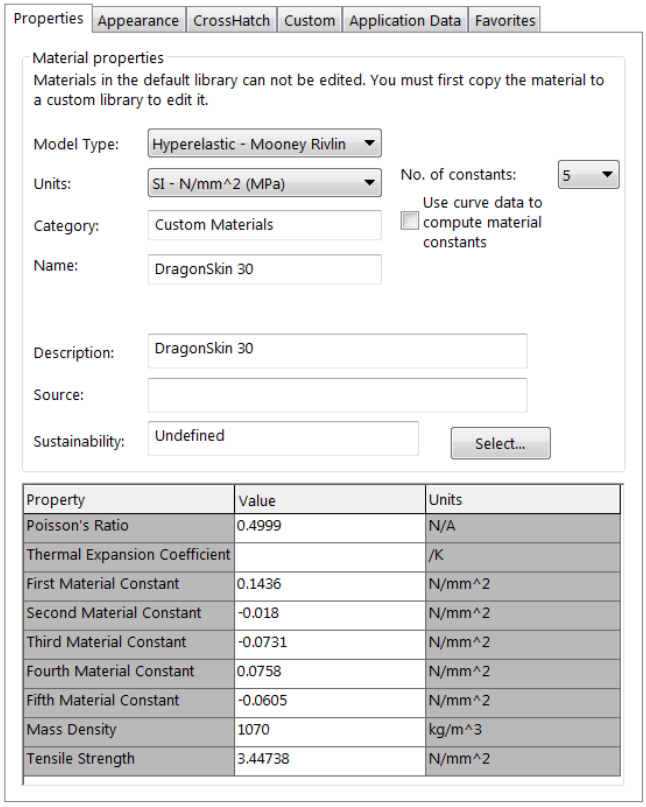

Figure 4.30 Material property of Dragon Skin 30 in SolidWorks.

The single module was cantilevered, the external load was applied to the end-effector of the module. The direction of the force is shown in Figure 4.31. The simulation result demonstrates the maximum strain is 0.4763 when the surface bonding module is subjected to a bending angle 56º. The maximum strain is within the range of the selected tensile testing strain range (between 0 and 0.5). Therefore, the tensile test is valid.

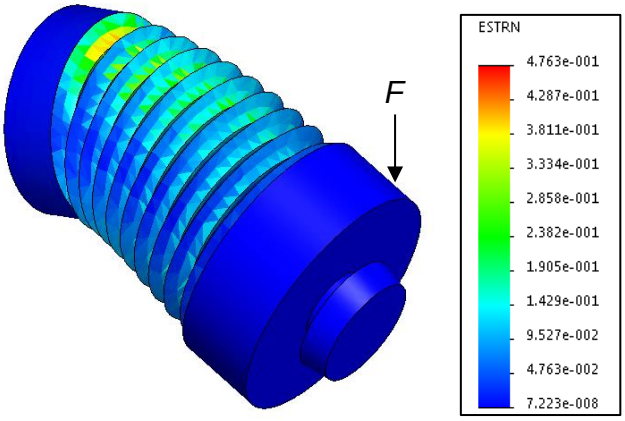

Figure 4.31 Strain range of the phase change module. Maximum strain is illustrated on the right.

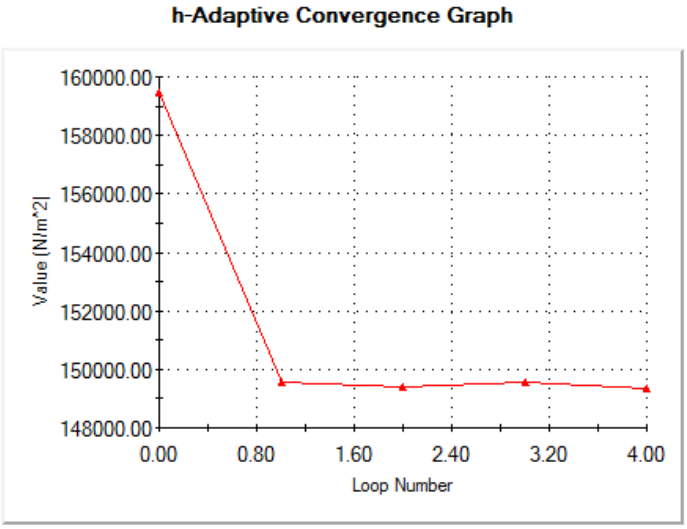

Figure 4.32 Mesh convergence study of the strain range of the phase change module. Maximum stress value is plotted in the figure.

Mesh convergence study was conducted in SolidWorks Simulation by using h-adaptive method. The result, as shown in Figure 4.32, justifies the accuracy of the simulation.

4.3.3.2 FEA Simulation on Bending Stiffness

The following assumptions were made for the simulations of the phase change modules. When LMPA is in soft state, the space occupied by the LMPA was

assumed to be empty. The temperature effect on the silicone material is negligible in the study. When LMPA is in the solid state, the contact set between the controllable stiffness element and the silicone material was assumed to be 'no penetration'. The elastic modulus of LMPA and GM (2884.6 MPa and 0.3967 MPa, respectively) are characterised in Chapter 3. The simulations were carried out in both rigid state and soft state. These modules were cantilevered in the studies, the external loads were applied to the end-effectors of the modules. The direction of the force and the results were shown in Figure 4.33, Figure 4.35, Figure 4.37 and Figure 4.39. Mesh convergence study was conducted in SolidWorks Simulation by using h-adaptive method. The result, as shown in Figure 4.34, Figure 4.36, Figure 4.38 and Figure 4.40, justify the accuracy of the simulation results.

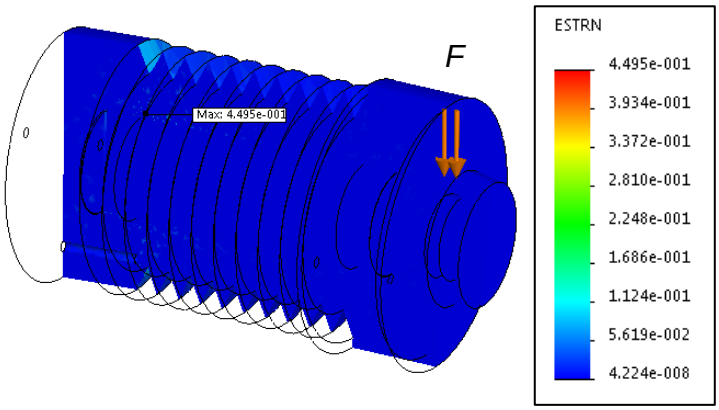

Figure 4.33 FEA model of LMPA module in rigid state. The equivalent strain is shown on the right.

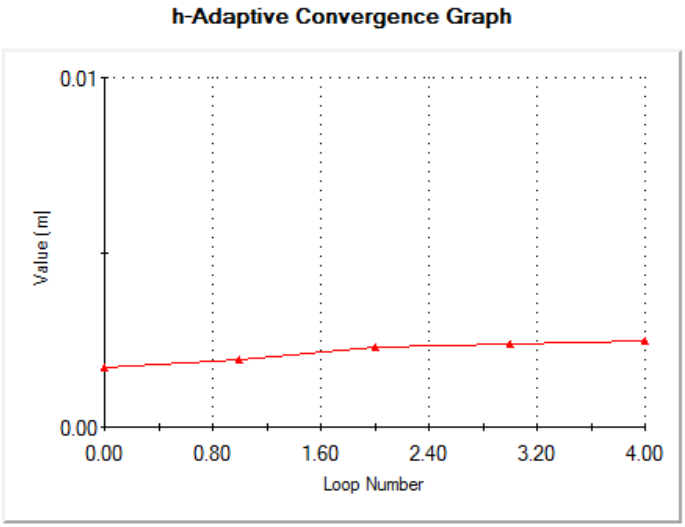

Figure 4.34 Mesh convergence study of LMPA module in rigid state. The maximum resultant displacement is plotted in the figure.

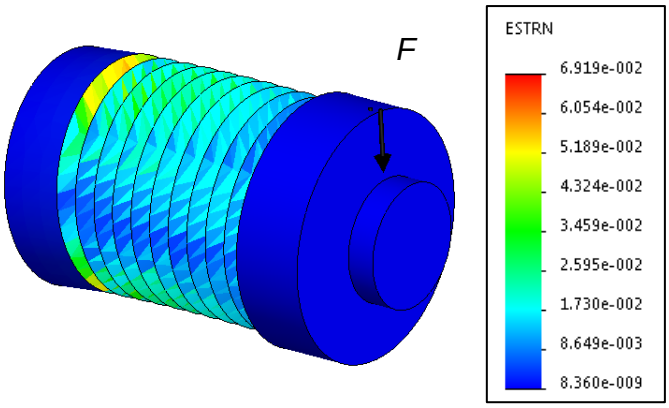

Figure 4.35 FEA model of LMPA module in soft state. The equivalent strain is shown on the right.

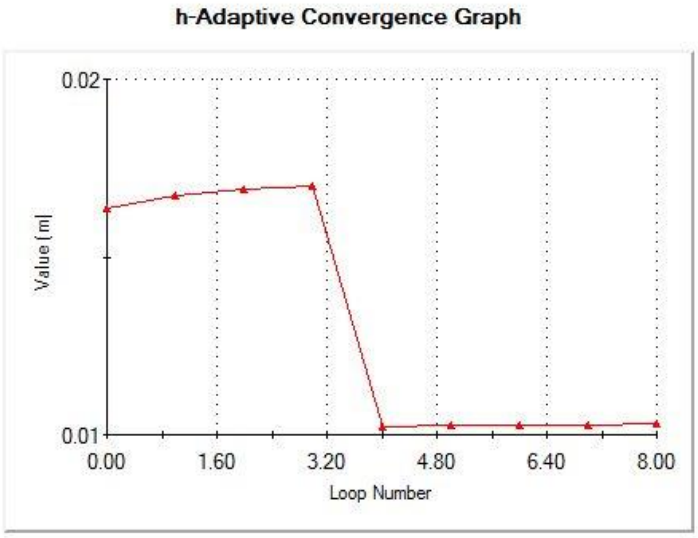

Figure 4.36 Mesh convergence study of LMPA module in soft state. The maximum resultant displacement is plotted in the figure.

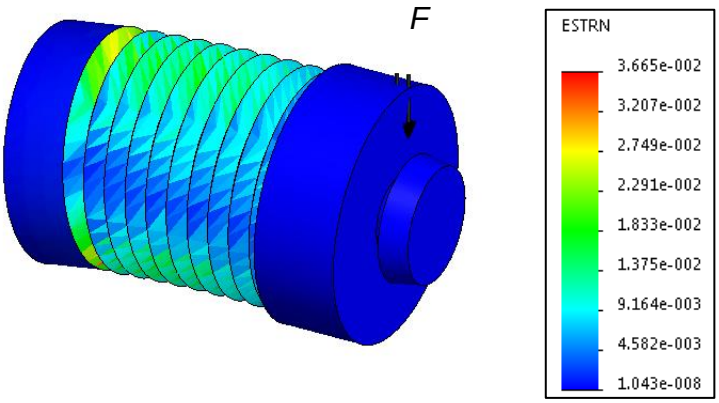

Figure 4.37 FEA model of GM module in rigid state. The equivalent strain is shown on the right.

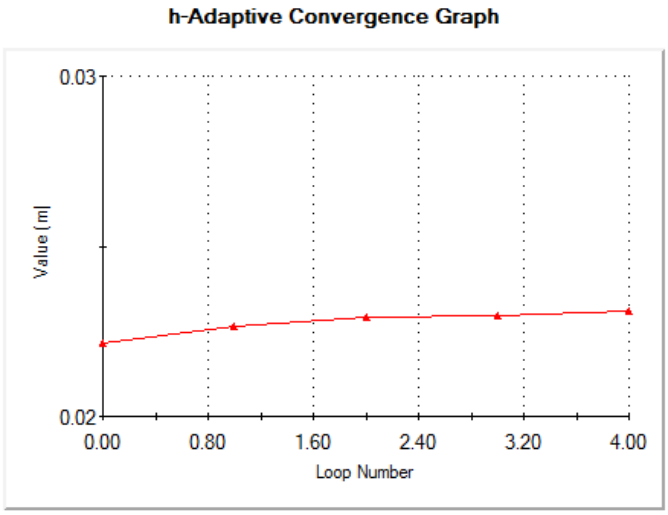

Figure 4.38 Mesh convergence study. The maximum resultant displacement is plotted in the figure.

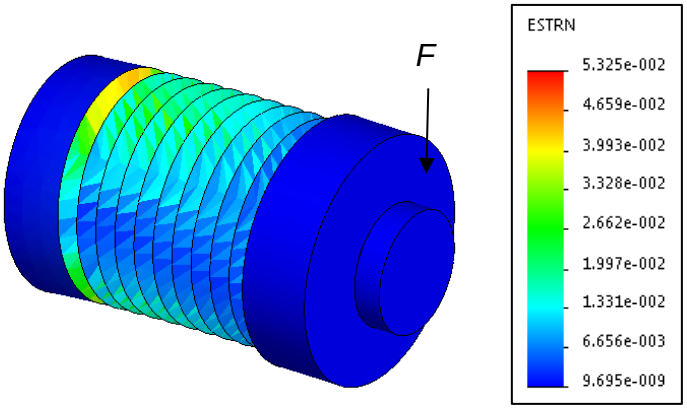

Figure 4.39 FEA model of GM module in soft state. The equivalent strain is shown on the right.

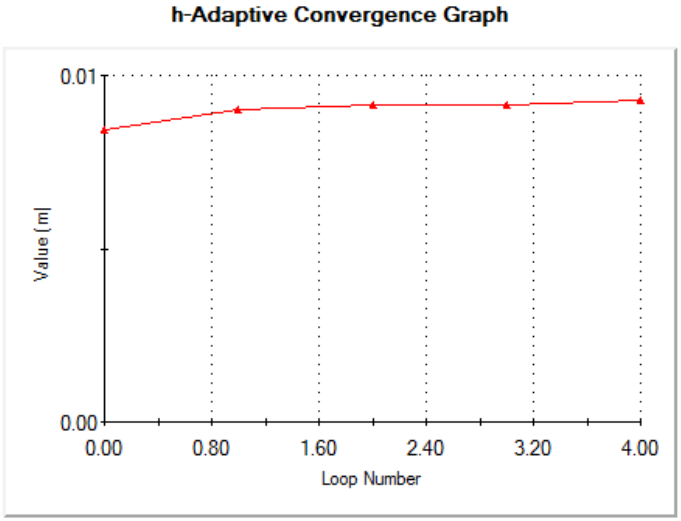

Figure 4.40 Mesh convergence study. The maximum resultant displacement is plotted in the figure.

The external loads used in the simulations, the displacement results, the maximum strain and the calculated bending stiffness are presented in the Table 4.6.

The results show the maximum equivalent strain for phase change modules fall into the tensile testing strain range, the simulations are therefore valid. As expected, the LMPA module has greater bending stiffness than GM module. The result also suggests when phase change modules are in soft state, LMPA-based approach has smaller bending stiffness than GM-base method.

Table 4.6 Theoretical Calculations of Bending Stiffness for the Single Module.

	Load (N)	**Displacement** (mm)	**Max Strain**	**Bending Stiffness** (N/mm)
LMPA (Rigid)	0.490	1.697	4.495e-001	0.2887
LMPA (Soft)	0.098	2.418	6.919e-002	0.0406
GM (Rigid)	0.098	1.301	3.665e-002	0.0753
GM (Soft)	0.098	1.483	5.325e-002	0.0661

4.4 Thermal Models of Single Module

The thermal models of the single module are given in this section. This information is specific to the LMPS-, HMA-, and LMPA-based module. The goal of this section is to provide insights on melting energy, heating time and cooling time.

4.4.1 Heating Process

To understand the energy input required to melt the TR fluids (LMPS, HMA, and LMPA) is crucial given the limited power miniature heater can provide in the single module. During the heating process, the thermal input is distributed between raising the temperature of the components of the single module and introducing phase change in the TR fluids. Heat loss during the heating process is assumed to be small in this study. The energy Q_{TR} required to melt the TR fluids in the single module can be estimated by the equation below.

$$Q_{TR} = mc\left(T_{melting} - T_0\right) + mL_f \qquad 4.13$$

where *m* is the mass of TR fluid, *c* is the specific heat capacity of the material, $T_{melting}$ is the melting temperature of the fluid, T_0 is the initial temperature of the material, and L_f is the material's latent heat fusion.

The melting time t can be estimated by using the energy input Q_{TR} and the power of the heater P_{heater}.

$$t = \frac{Q_{TR}}{P_{heater}} \tag{4.14}$$

Melting time model assumes that 100% of the power input is used to melt the TR fluids. In practice, heat is lost to the remaining materials of the module. Therefore, this model is the lower bound on melting time.

Heat time calculation model can provide the insight into how to reduce the melting time. Increasing the power could minimise the melting time. Furthermore, the materials with low melting point temperature are desirable, as well as low specific heat capacity and low latent heat fusion. Although the reduction in the mass of LMPS and HMA could shorten the melting time, it may lead to the decrease in the bonding strength. However, for the LMPA-based single module, the reduction of the material could provide a proportional decrease in heating time.

4.4.2 Cooling Process

The first step in the cooling analysis is to understand where the heat travels during the process. Figure 4.41 shows a schematic of the heat path of the single module during cooling.

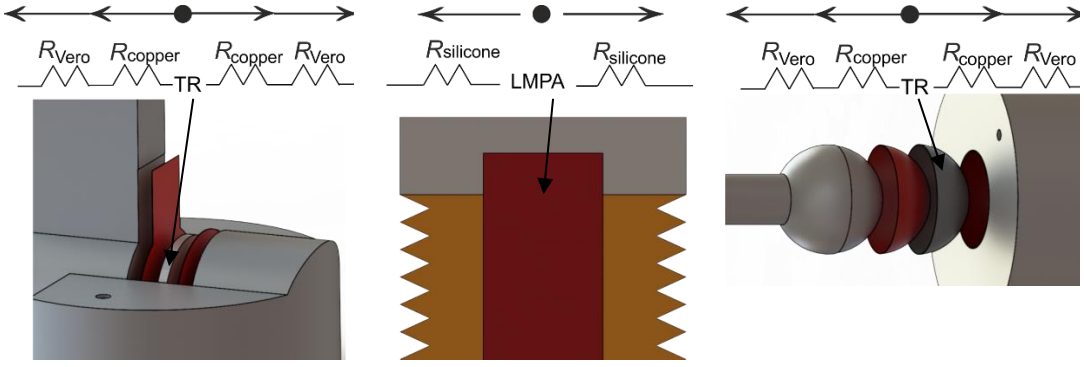

(a) (b) (c)

Figure 4.41 Heat path of the single module during cooling process. (a) heat path of LMPS- and HMA-based single module (revolute joint). (b) heat path of LMPA-based single module. (c) heat path of LMPS- and HMA-based single module (spherical joint).

The energy source is the TR fluid. The solidification energy of the TR fluid must be lost in order for the single module to enter the rigid state. The solidification energy can be calculated as,

$$Q_{solid} = mc(T - T_{solidus}) + mH_f \quad 4.15$$

where *m* is the mass of the TR fluid, *c* is the specific heat capacity for the material, *T* is the temperature of the TR fluids at the beginning of the cooling step, $T_{solidus}$ is the solidus temperature of the materials, and H_f represents the heat of fusion of the TR fluid.

The energy of the remaining components must be conducted out before the TR fluid solidified. The path for energy to exit is through conduction to the heat sink components. The heat transfer rate during cooling be estimated as,

$$q = \frac{T - T_{solidus}}{R_{sink}} \quad 4.16$$

where *T* represents the temperature of the heat sink components at the beginning of the cooling step, R_{sink} is the thermal resistance of the heat sink components, R_{sink} can be calculated as,

$$R_{sink} = \frac{L_{heat}}{A_k k} \quad 4.17$$

where L_{heat} is the length of the heat travels, A_k is the conduction area, and *k* is the thermal conductivity of the material.

Cylindrical model, as shown in Figure 4.42, is used for the thermal resistance calculation of LMPA-based single module.

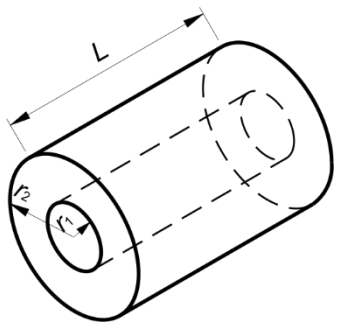

Figure 4.42 Cylindrical model for thermal resistance calculation.

Thermal resistance of the heat sink component can be estimated,

$$R_{sink} = \frac{\ln(r_2/r_1)}{2\pi L k} \quad 4.18$$

where r_1 is the inter radius of the cylinder, r_2 is the outer radius of the cylinder, *L* represents the length of the cylinder, *k* is the thermal conductivity of the material.

Solid sphere model, as illustrated in Figure 4.43, is used for the thermal resistance estimation for the second prototype of LMPS- and HMA-based single module.

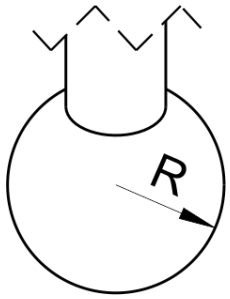

Figure 4.43 Spherical model for thermal resistance estimation.

Thermal resistance of the heat sink component can be estimated as,

$$R_{sink} = \frac{1/R}{4\pi k} \tag{4.19}$$

where *R* is the radius of the sphere, *k* is thermal conductivity of the material.

The cooling time for the single module *t* can be estimated in the following equation,

$$t = \frac{Q_{solid}}{q} \tag{4.20}$$

The temperature of the TR fluids and heat sink components is assumed to be equal to the melting point temperature of the TR fluids. However, due to the temperature difference caused by the thermal resistance of each component, components did not reach the melting point temperature of the TR fluid. In addition, the cooling time estimation model considers 100% the conduction cooling from one hot part to another cooler part.

The model provides the insight on how to reduce cooling time. For example, the design of the heat sink is important to the cooling step. The smaller the length of the heat travels, the smaller the resistance the heat conducts out of the energy source. In addition to the heat sink, the reduction of the mass of the TR fluids could reduce the cooling time. This information is specific to the LMPA-based single module since the reduction of the mass of LMPS and HMA could lead to the decrease of the bonding strength.

4.5 Summary

This chapter presents the design and analysis of the single module. Four materials that were selected and experimentally characterised in Chapter 3 are used to realise the controllable stiffness feature of the single module. Mechanical and thermal models for each design were developed. Summary for each design is presented below.

- Surface bonding single module

  (1) The first developed module consists of one degree of freedom revolute joint, a thermally activated locking mechanism and a bellows-like structure.

  (2) The second developed module is composed of a spherical joint, a thermally activated locking mechanism and a bellows-like structure.

  (3) Snap-fit approach was used to design the revolute joint and spherical joint, resulting in an angle range of 56^{o}.

  (4) LMPS and HMA were used to develop the thermally activated locking mechanism, which enabled the module to be locked at arbitrary position.

  (5) The shear bonding torque that LMPS or HMA can provide is developed. The radius of the bonding area was estimated. The revolute joint: $T_{lock} = \frac{2\pi}{3}\tau R^3$. The spherical joint: $T_{lock} = 2\pi R^3 \tau \int_0^{\theta} \sin\theta^2 \, d\theta$. τ is the shear strength of the material, R is the radius of the bonding area, and θ represents the rotation angle.

  (6) Bending stiffness for the single modules are estimated through FEA simulations. The numerical results are provided.

  (7) Thermal models (melting time and cooling time) for single module were presented. These models provide insights on the reduction of response time.

- Phase change single module

  (1) The module consists of a silicone structure and LMPA- or GM-based controllable stiffness element.

  (2) The reason of using bellows-like structure was justified through FEA simulations. The number of bellows was optimized through FEA simulations. Total number of bellows was selected to be 10.

  (3) Bending stiffness for the single modules were simulated for solid-like state and liquid-like state, respectively. The numerical results were provided.

  (4) Thermal models (melting time and cooling time) for LMPA-based module were presented. These models provide insights on the reduction of response time.

This chapter lays out the theoretical foundation for this research. The numerical results calculated in this chapter will be validated against experimental data (Chapter 6).

Chapter 5
Fabrication of the Single Module

5.1 Introduction

This chapter presents the fabrication method of the single module. The proposed designs consist of rigid components, silicone structures and controllable stiffness elements. The plastic components of the single module were produced by a 3D printer (Object 1000, Stratasys Ltd). The fabrication method for the remaining of the components is discussed in this chapter. The method of applying LMPS (low melting point solder) and HMA (hot-melt adhesive) to the surface of the copper tapes is provided.

5.2 Surface Bonding Single Module

Surface bonding single module consists of cable-driven rigid joint (revolute joint and spherical joint were developed in this research), a thermally activated locking mechanism, and a flexible bellows-like structure. Fabrication of the flexible bellows-like structure is introduced in this section. The CAD models of the mould are presented in Appendix D. The methods of applying low melting point solder and hot-melt adhesive to the surface of copper tapes are described.

5.2.1 Fabrication of the Flexible Bellows-like Structure

5.2.1.1 Revolute Joint

The components of the mould for the fabrication of the bellows-like structure of the revolute joint are shown in Figure 5.1. The mould is consisted of top cap, two stainless steel pins, two cylindrical structure and a bottom cap. Stainless steel pins were used to create the cable channels to actuate the joint. The plastic components were fabricated by using a 3D printer (Object 1000, Stratasys Ltd).

The silicone material was prepared by mixing two components (Part A and Part B) of Ecoflex 0030 in a 1:1 weight ratio. The mixed material was stirred well and then put in a degassing chamber to remove the air bubbles trapped in the liquid. The flexible bellows-like structure is fabricated by pouring the silicone material into the mould. Two stainless steel pins were then inserted into the bottom cap. Top cap was used to seal the mould and keep the pin in the position. Due to the limitation of the lab equipment, the material was cured

at room temperature. It takes four hours for Ecoflex 0030 to cure at room temperature.

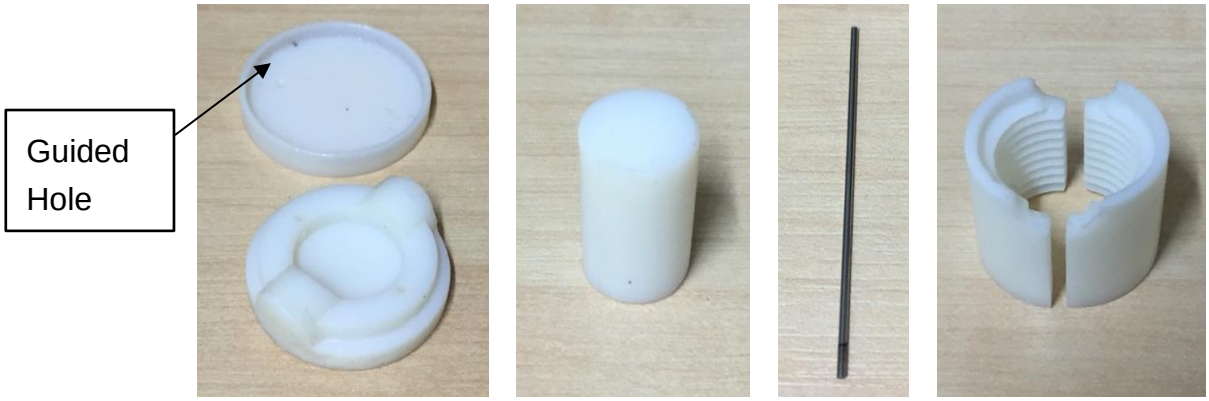

Figure 5.1 Components of the mould for the fabrication of the bellows-like structure. (a) Top and bottom cap. (b) Cylinder for creating the space for the revolute joint. (c) Stainless steel pin. (d) Two half cylindrical moulds.

5.2.1.2 Spherical Joint

The plastic components were fabricated by using a 3D printer (Object 1000, Stratasys Ltd). The components for the fabrication of the bellows-like structure for the spherical-joint-based module are shown in Figure 5.2. The silicone structure is slightly different than the one for the revolute joint. However, the same fabrication procedure was undertaken. The fabricated bellows-like structures are shown in Figure 5.3.

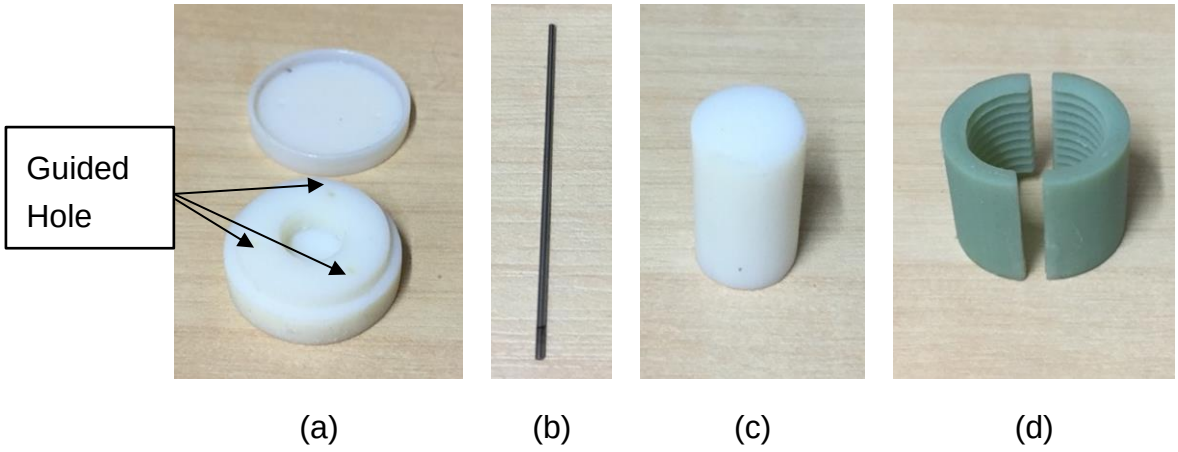

Figure 5.2 Components of the mould for the fabrication of the bellows-like structure. (a) Top and bottom cap. (b) Stainless steel pin. (c) Cylinder for creating space for the spherical joint. (d) Two half cylindrical moulds.

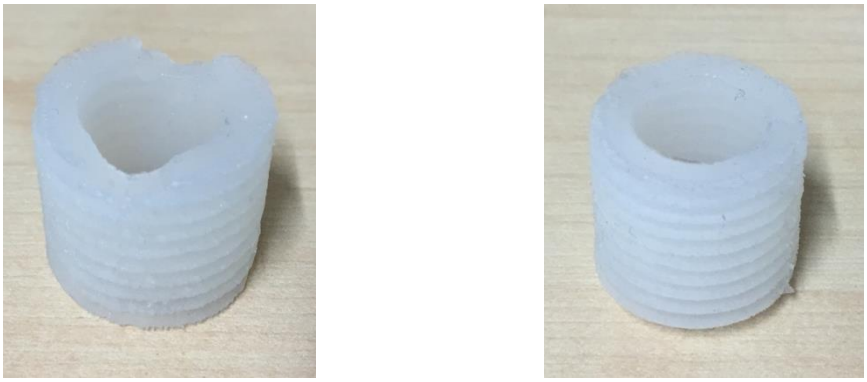

(a) (b)

Figure 5.3 The bellow-like structure after demoulding. (a) Bellows-like structure for the revolute joint. (b) Bellows-like structure for the spherical joint.

5.2.2 Low Melting Point Solder (LMPS) and Hot-melt Adhesive (HMA) Application Method

5.2.2.1 Low Melting Point Solder (LMPS) Application Method

Due to the high surface tension and low reactivity with other metals, it is not possible to apply LMPS (Field's Metal) to the surface of the copper tape without pre-treatment. Flux is commonly used for preparing the surfaces in electronics applications. Therefore, flux was used to pre-treat the surface of the copper before applying Field's Metal.

(a) (b) (c)

Figure 5.4 The method for applying Field's Metal to the surface of a copper tape. (a) Applying flux on the surface of the copper tape. (b) Dipping the copper tape into Field's Metal. (c) The copper tape is fully covered with Fields' Metal.

The application method of LMPS was taken in three steps. First, flux was applied to the surface of the copper tape by using a cotton swab [See Figure 5.4 (a)]. Then pre-treated copper tape was dipped into Field's Alloy at approximately 200 °C [see Figure 5.4 (b)]. As a result, the pre-treated surface was fully covered by Field's Metal [see Figure 5.4 (c)]. Finally, flux residue was cleaned with warm water.

5.2.2.2 Hot-melt Adhesive (HMA) Application Method

Based on the thermal models provided in Chapter 4, the mass of the material affects the heating and cooling time of the single module. Therefore, a small piece of material was prepared by cutting from a low melting point temperature glue stick [see Figure 5.5 (a)]. The copper tape was then preheated by a hotplate to raise the surface temperature above the melting point [see Figure 5.5 (b)]. Finally, the material was applied to the surface of the copper tape to form the bond [see Figure 5.5 (c)].

(a) (b) (c)

Figure 5.5 The method for applying hot-melt adhesive to the surface of a copper tape. (a) A small piece of HMA has been cut from a glue stick. (b) Preheat the copper tape with a hotplate. (c) The surface of the copper tape is fully covered with HMA.

5.2.3 Fabrication of the Complete Module.

The fabrication of shaft and base of the joint was using 3D printing technique (Object 1000, Stratasys Ltd). Resistance wires were used to activate the

bonding materials. They were wound and closely attached to a copper tape, as shown in Figure 5.6 and Figure 5.7. The application method of LMPS and HMA was introduced in Section 5.2.2. The copper tapes and resistive heater were glued on the joint shaft by Gorilla Super Glue. The joint shaft was then pushed into the base. The fabricated silicone bellows-like structure was glued on the plastic components by using Sli-Poxy Silicone Adhesive (Sil-Poxy©, Bentley Advanced Materials). The fabricated modules are shown in Figure 5.8.

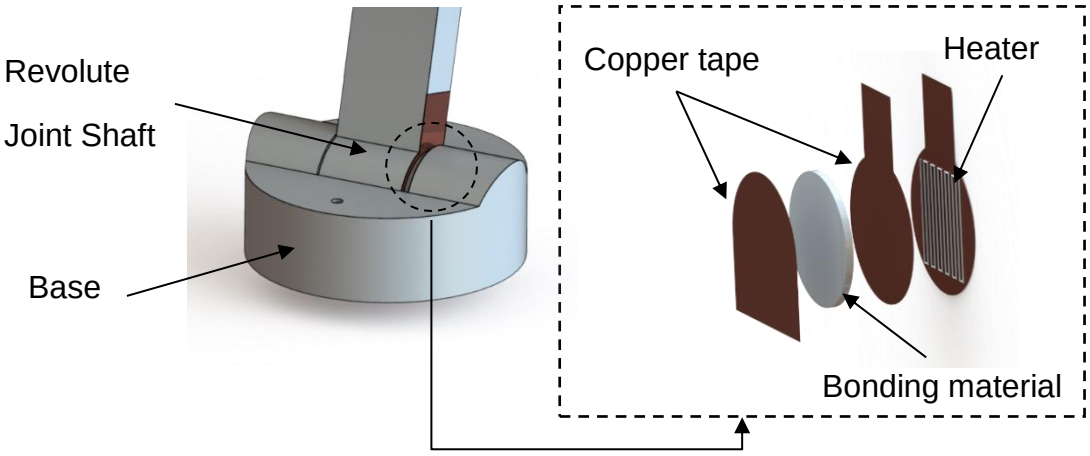

Figure 5.6 The components for thermally activated revolute joint.

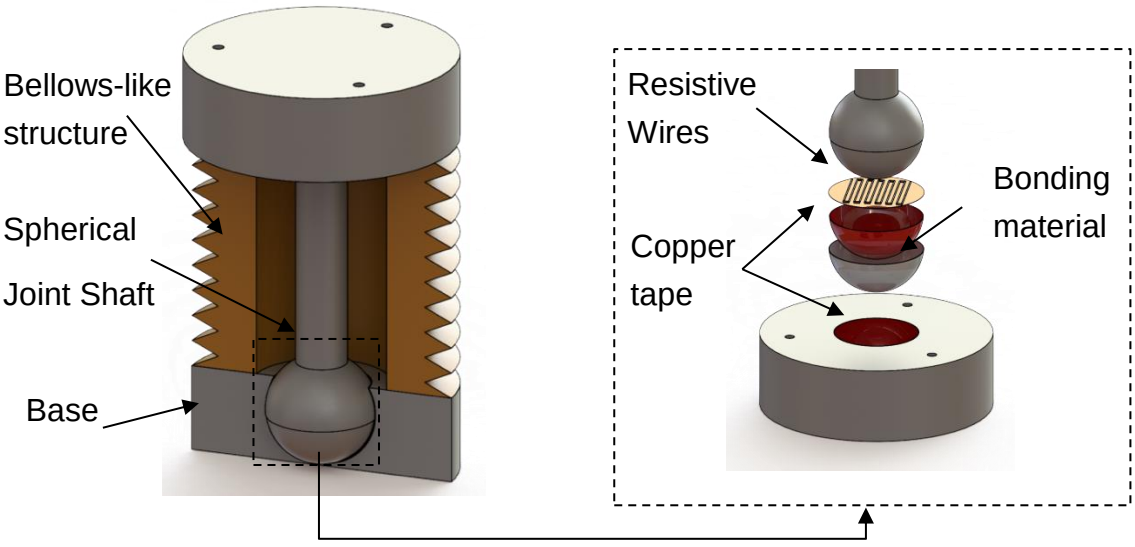

Figure 5.7 The components for the thermally activated spherical joint.

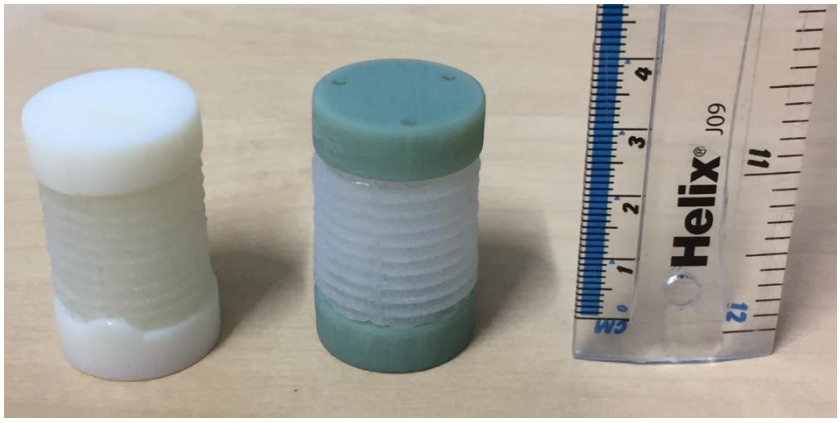

Figure 5.8 The fabricated thermally activated revolute (Left) and spherical (Right) joint.

5.3 Phase Change Single Module

Phase change single module consists of a soft structure and a controllable stiffness Element. The fabrication steps of all the components are described as below.

5.3.1 Fabrication of Controllable Stiffness Element

5.3.1.1 LMPA-based Controllable Stiffness Element

The LMPA-based controllable stiffness element consists of a solid cylindrical LMPA, an external membrane and resistive wires. The mould for producing the cylindrical LMPA is shown in Figure 5.9.

Figure 5.9 Components of the mould for fabricating LMPA-based controllable stiffness element.

The fabrication was conducted through several steps. First, liquefied LMPA was poured into the fully assembled mould to form a cylinder [See Figure 5.10

(a)]. The cylinder is 10 mm in diameter and 30 mm in length. Once the material is solidified, the mould is removed. The fabricated cylinder was dipped into liquid silicone (Dragon Skin 30, Smooth-On, Inc.) to form an external membrane [see Figure 5.10 (b)]. The membrane was used to insulate the heating element from LMPA since silicone material is typically heat-resistant. In the final step, the resistive wires were wound and attached closely to the cylindrical surface of the silicone membrane, as shown in Figure 5.10 (c).

(a) (b) (c)

Figure 5.10 Fabrication steps of LMPA-based controllable stiffness element. (a) Pouring liquefied LMPA into a fully assembled mould. (b) Dipping a cylindrical LMPA into silicone material. (c) Resistive wires were wound and closely attached to the silicone membrane.

5.3.1.2 GM-based Controllable Stiffness Element

The GM-based controllable stiffness element consists of a latex membrane and coarsely ground coffee (~900 microns). The mould for fabricating the latex membrane, as shown in Figure 5.11, was produced by a 3D printer (Object 1000, Stratasys Ltd).

Figure 5.11 The mould for the fabrication of an external latex membrane.

The membrane was formed by dipping the mould into a liquid latex [see Figure 5.12 (a) and (b)]. Once the latex was cured, it was filled with coarsely ground coffee [see Figure 5.12 (c)]. A plastic diameter tube (1.5mm in diameter) was used as vacuum pipe. A piece of Nylon tissue was used as filter. The connection between the tube and the membrane was sealed with Parafilm.

(a) (b) (c)

Figure 5.12 Fabrication steps of a GM-based controllable stiffness element. (a) The mould was dipping into a liquid latex. (b) Curing the latex membrane. (c) Fabricated GM-based controllable stiffness element (top) and ground coffee (bottom).

5.3.2 Fabrication of the Complete Module

The components of the mould for the fabrication of the soft structure are shown in Figure 5.13. Three stainless steel pins were used to create cable channels to actuate the module. The plastic components were produced by a 3D printer (Object 1000, Stratasys Ltd).

Two formulations of silicone rubber, i.e. Ecoflex 0030 (Smooth-On, Inc.) and Dragon Skin 30 (Smooth-On, Inc.), was used for the fabrication of the soft structure due to high flexibility and high Shore hardness, respectively. Ecoflex 0030 was used for fabricating the flexible bellows-like structure. Dragon Skin 30 was selected to create top and bottom cap to provide the stability and rigidity during bending.

The Ecoflex 0030 and Dragon Skin 30 were first prepared by mixing two components (Part A and Part B) in a 1:1 weight ratio, respectively. The mixed materials were stirred well and then put in a degassing chamber to remove the air bubbles trapped in the liquids. Due to the lack of the lab equipment, the materials were cured at room temperature. It takes four hours for Ecoflex 0030 to be cured at room temperature and sixteen hours for Dragon Skin 30.

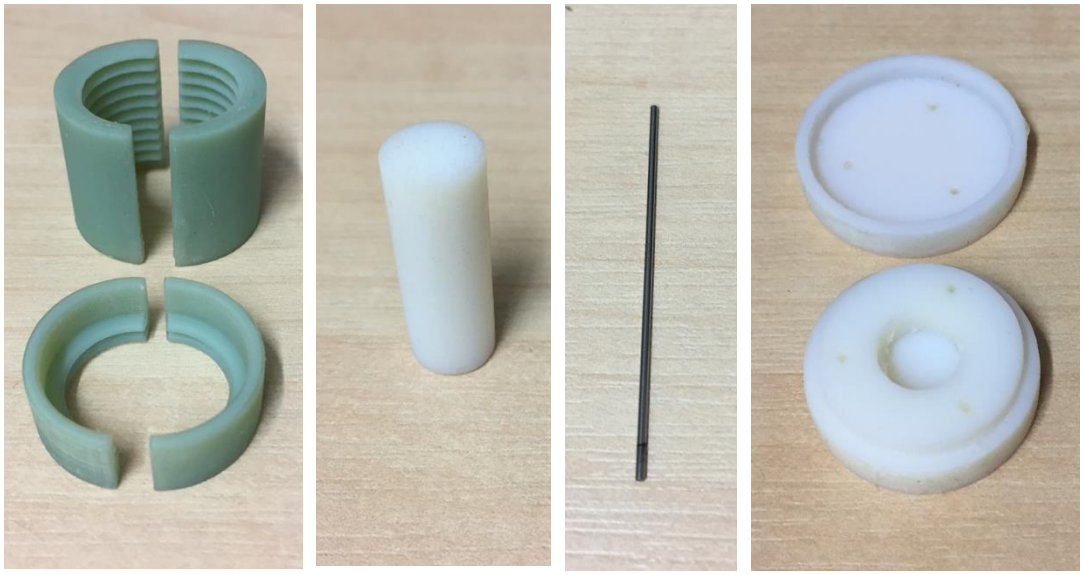

(a) (b) (c) (d)

Figure 5.13 The components for the fabrication of the soft structure of the single module. (a) Half cylindrical moulds for the fabrication of the bellows-like structure (top) and top and bottom cap (bottom). (b) Cylinder for creating the space for controllable stiffness element. (c) Stainless steel pin for creating the cable channels. (d) Top and bottom mould.

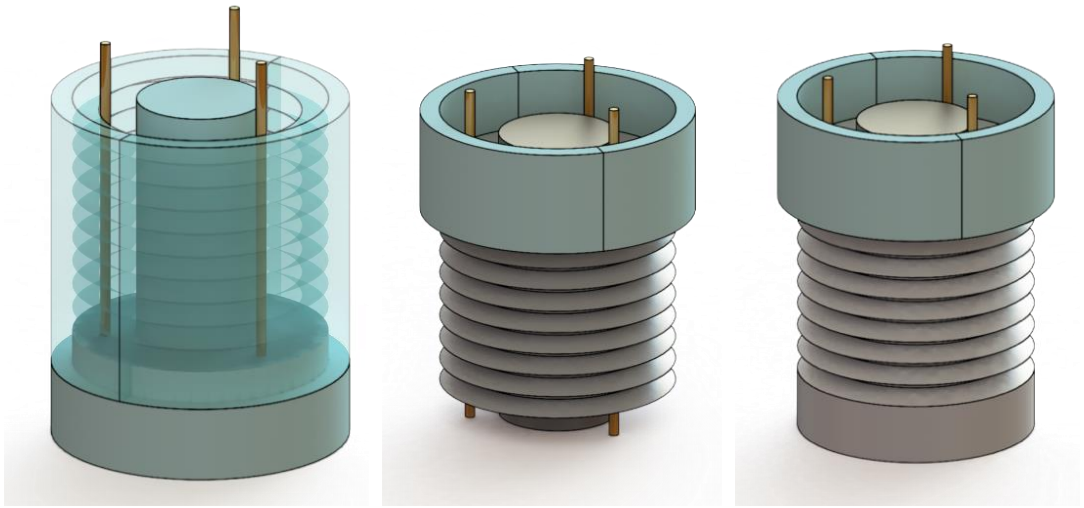

(a) (b) (c)

Figure 5.14 Fabrication of the complete module. (a) Pouring the Ecoflex 0030 into a fully assembled mould. (b) Placing the controllable stiffness element into the bellows-like structure and pouring the Dragon Skin 30 to create top cap. (c) Pouring the Dragon Skin 30 to create bottom cap.

The fabrication of complete module was conducted through several steps. First, Ecoflex 00-30 was poured into the assembled mould to form bellows-like structure, as shown in Figure 5.14 (a). Top mould, as shown in Figure 5.14 (d), was used to seal the mould and keep the pin in the position. Once

the silicone was polymerised, the top mould and outer shells were removed. Second, new half cylindrical shells were enclosed the bellows-like structure, and the controllable stiffness element was placed inside the bellows-like structure [see Figure 5.14 (b)]. Dragon Skin 30 was then poured to seal the element and create the top cap. With this process, three stainless steel pins were kept inside the bellows-like structure. When the Dragon Skin 30 was cured, the same procedure was executed again on the opposite side [see Figure 5.14 (c)]. Thus, the controllable stiffness element was fixed to the top and bottom cap.

The complete fabricated prototypes for Phase change single module are shown in Figure 5.15. The LMPA-based single module is shown in Figure 5.15 (a), and the GM-based single module is shown in Figure 5.15(b).

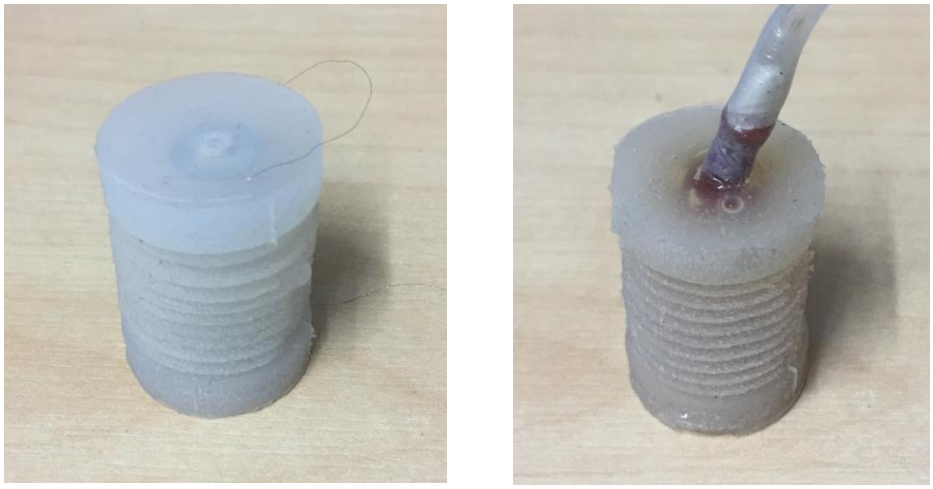

(a) (b)

Figure 5.15 The fabricated prototypes. (a) LMPA-based single module. (b) GM-based single module.

It is worth noticing that cure inhibition occurs when fabricating GM-based module. It occurs when contaminants on a model surface prevent the liquid silicone from properly curing. This could be mitigated by cleaning the surface of the latex chamber before applying silicone over the model.

5.4 Summary

This chapter presents the fabrication steps of the single modules. The proposed designs have been realised for the experimental validation. The methods of applying low melting point solder and hot-melt adhesive to the surface of the copper tape were introduced. The fabricated prototypes were presented.

Chapter 6
Experimental Validation of Single Module

6.1 Introduction

This chapter presents the experimental characterisation of the single modules. The prototypes of each design are presented and analysed for performance with the emphasis on the increase in stiffness and the response time. The theoretical models and FEA simulation results presented in Chapter 4 are validated throughout the experiments. Failure modes are discussed in the end.

6.2 Stiffness Validation of Single Module

The validation of a single module stiffness was conducted in two separate experiments: (1) A single module was cantilevered, and weights were hung from its free end while the lateral displacement of the end effector was recorded. (2) Axial compression tests were conducted to characterise the stiffness change of phase change modules. All tests were carried out when the modules were in rigid and soft state.

6.2.1 Lateral Displacement Test

Bending stiffness is an important criterion for understanding the force that the single module can support against gravity when cantilevered. It is used in this thesis to evaluate and compare the stiffness change of each design approach. Bending stiffness is calculated as the slope of the first linear region in the load-displacement graph obtained from the lateral displacement test.

6.2.1.1 Surface Bonding Single Modules

The experimental setup for surface bonding modules in lateral displacement test is shown in Figure 6.1. The modules were tested in rigid and soft state. Noted that an end-effector was designed to mount on the single module. A cable was tied at the end-effector to attach external loads. The deflection, as illustrated as "*D*" in Figure 6.1 (a), was defined as the change in position when supporting a load against gravity at the free end. Three trials were conducted, the average displacement was plotted in Figure 6.2. Experimental data from the trials were listed in Appendix B.

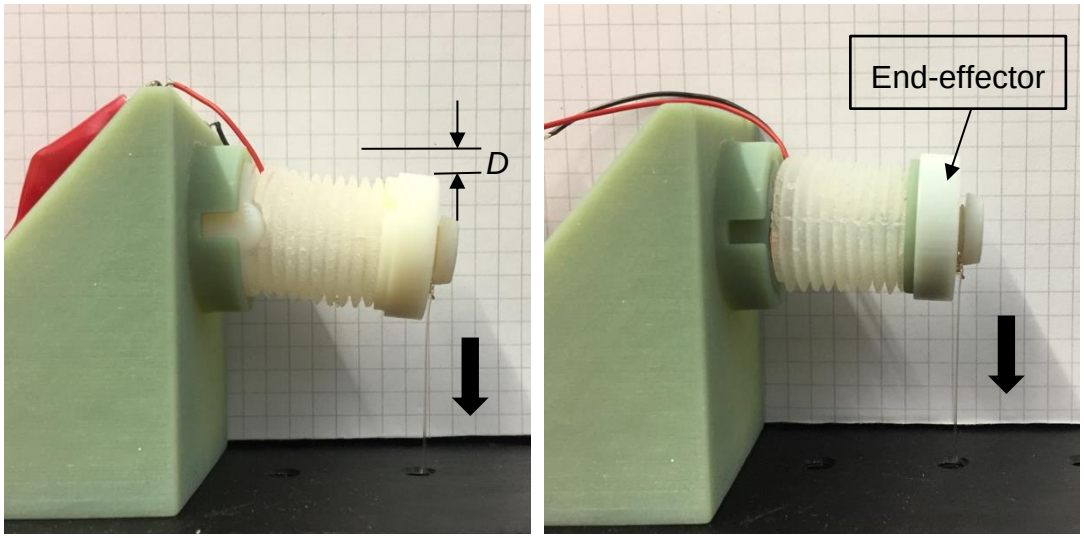

(a) (b)

Figure 6.1 Experimental setup for lateral displacement test. The direction of the imposed displacement is highlighted by the black arrow. (a) An external load was imposed at free end of the single module consists of revolute joint, where *D* is the displacement. (b) Single module consists of spherical joint in lateral displacement test.

Figure 6.2 illustrates the load required to deflect the end effector of a single module in lateral displacement test. All four tested modules appear to show a linear elastic region and a yield point (indicated as 'X'). 'Yield point' indicates the break of the LMPS/HMA bond (large displacement occurs).

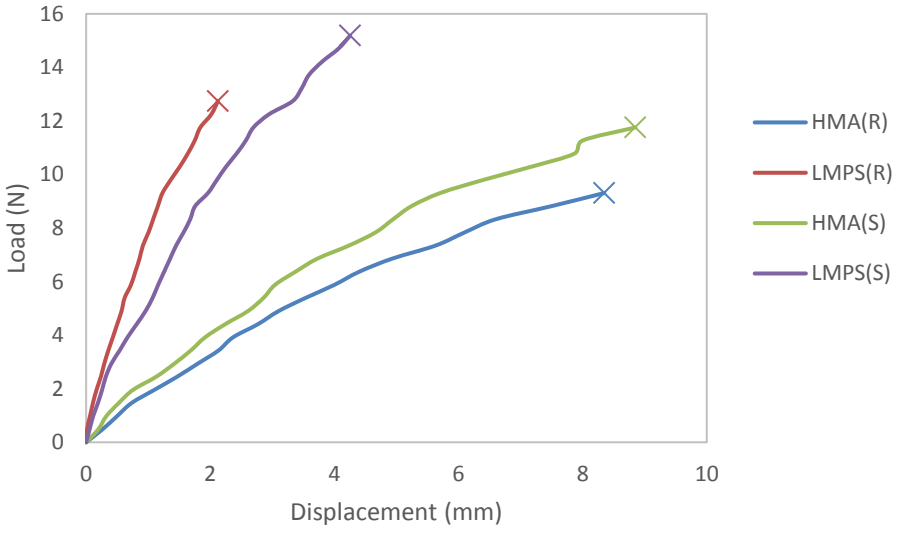

Figure 6.2 Load vs Displacement graph for the cantilevered surface bonding single modules in rigid state. "X" stands for the yield point. HMA (R) and LMPS (R) represent a revolute joint employs HMA- and LMPS-based locking mechanism, respectively. HMA (S) and LMPS (S) indicate a spherical joint explores HMA- and LMPS-based locking mechanism, respectively.

The average yield points for the revolute joint employs HMA-based and LMPS-based locking mechanism are 9.47 N and 13.23 N, respectively. The average yield points for the spherical joint utilizes HMA-based and LMPS-based locking mechanism are 12.25 N and 16.01 N, respectively. This result indicates that surface bonding modules were able to support a payload equal to more than 25X of their own weights (the average weight of surface bonding modules is 38 grams); in contrast, a granular jamming manipulator developed by Cheng et al. [71] can support a payload that is 2X of its own weight.

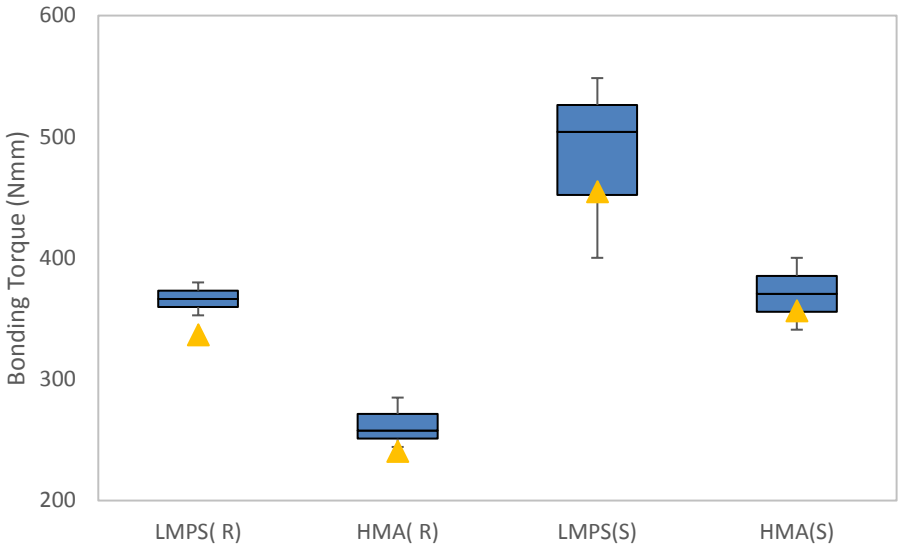

Figure 6.3 Box plot of the bonding torque of surface bonding modules. Theoretical (yellow triangle) and experimental (blue square) data are presented in the figure. HMA (R) and LMPS (R) represent a revolute joint employs HMA-based locking mechanism and LMPS-based locking mechanism, respectively. HMA (S) and LMPS (S) indicate a spherical joint explores HMA- and LMPS-based locking mechanism, respectively.

The torque imposed on the proximal revolute joint employs HMA- and LMPS-based locking mechanism at the yield point can be calculated as 262.32 Nmm and 379.91 Nmm, respectively. The torque imposed on the proximal spherical joint explores HMA- and LMPS-based locking mechanism can be estimated as 370.56 Nmm and 484.20 Nmm, respectively. The theoretical estimations for aforementioned designs are calculated in Chapter 4 as: 240.46 Nmm, 336.75 Nmm, 356.47 Nmm and 453.73 Nmm, respectively. The validation results, as plotted in Figure 6.3, follow the trends expected by the theoretical models.

Figure 6.4 and Figure 6.5 illustrate the force required to deflect the single modules when they are in soft state. Three trials were conducted, the average displacements were plotted in the figure. The graphs indicate that when the

surface bonding modules were in soft state, the displacements of the modules when under same external load were similar.

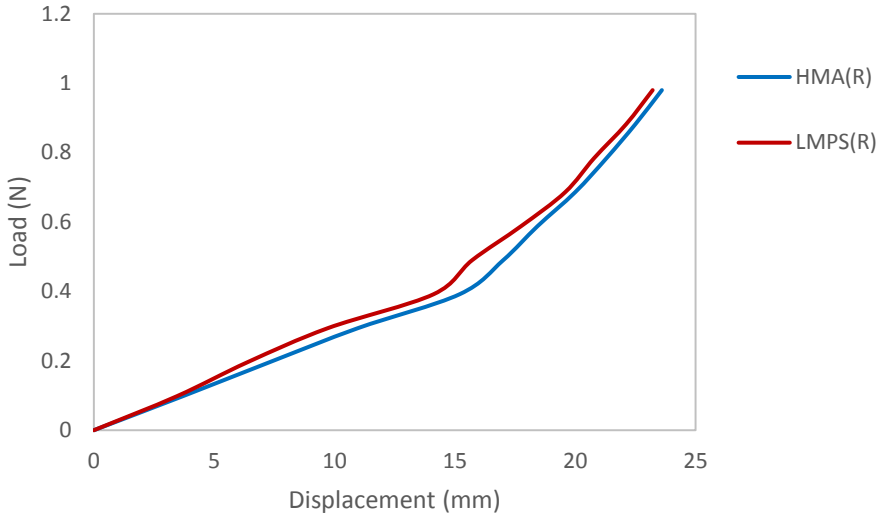

Figure 6.4 Load vs Displacement graph for revolute joint employs HMA- and LMPS-based locking mechanism in soft state. HMA (R) and LMPS (R) represent a revolute joint employs HMA- and LMPS-based locking mechanism, respectively.

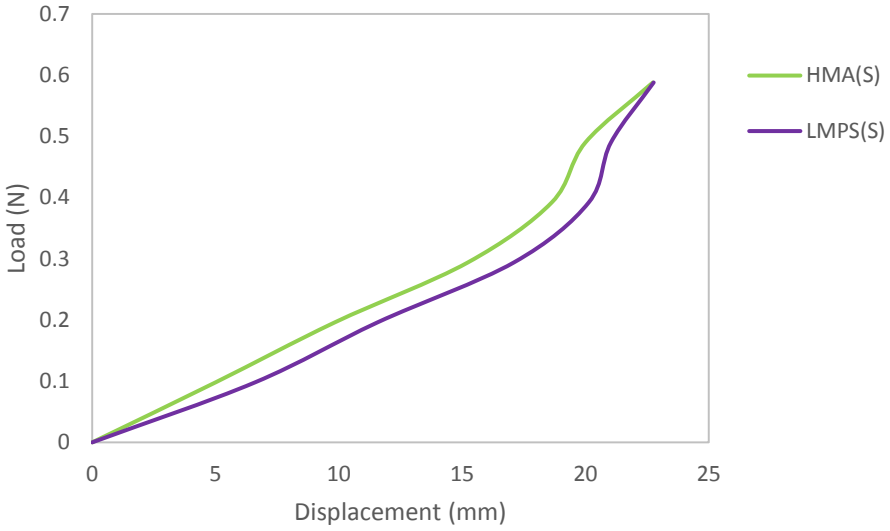

Figure 6.5 Load vs Displacement graph for spherical joint utilizes HMA- and LMPS-based locking mechanism in soft state. HMA (S) and LMPS (S) indicate a spherical joint explores HMA- and LMPS-based locking mechanism, respectively.

The data plotted in Figure 6.2, Figure 6.4 and Figure 6.5 were used to determine the bending stiffness of the surface bonding module in rigid and soft state. The bending stiffness was calculated as the slope of the first linear region in the load-displacement graph. The numerical results for the bending stiffness and increase ratio of each design are presented in Table 6.1. The

stiffness increase ratio is defined as below to measure the level of increase in this research.

$$increase\ ratio = \frac{bending\ stiffness\ in\ rigid\ state}{bending\ stiffness\ in\ soft\ state} \quad 6.1$$

Table 6.1 Numerical Results from Lateral Displacement Test. HMA (R) and LMPS (R) represent a revolute joint employs HMA- and LMPS-based locking mechanism, respectively. HMA (S) and LMPS (S) indicate a spherical joint explores HMA- and LMPS-based locking mechanism, respectively.

Design method	**Bending stiffness in soft state** (N/mm)	**Bending stiffness in rigid state** (N/mm)	**Stiffness increase ratio** (rigid/soft)
LMPS(R)	0.029±0.003	5.969±1.559	205.8
HMA(R)	0.026±0.001	1.228±0.233	47.2
LMPS(S)	0.017±0.000	3.669±0.468	215.8
HMA(S)	0.021±0.000	1.274±0.113	60.7

Based on the FEA simulations provided in Chapter 4, the bending stiffness for the revolute joint and spherical joint in rigid state are 8.7214 N/mm and 8.9620 N/mm, respectively. The bending stiffness for the revolute joint and spherical joint in soft state are 0.0269 N/mm and 0.0171 N/mm, respectively. Experimental bending stiffness is calculated for all surface bonding modules in both rigid and soft state. The comparisons between FEA simulations and experimental data are shown in Figure 6.6 and Figure 6.7. The results show that the FEA simulations overestimate rigid phase stiffness. However, they closely predict the soft phase stiffness. The theoretical rigid phase stiffness was estimated on the assumption that all modules can achieve a complete shape lock (The influence of the bonding strength of the material was not considered, the shaft and base of the joint were assumed to be one component). The assumption can be used to explain the difference between FEA predictions and experimental results. The experimental results indicate that the module employs the LMPS-based locking mechanism has greater stiffness than HMA-based locking mechanism. Therefore, it is closer to achieve a complete shape lock than the HMA-based design approach.

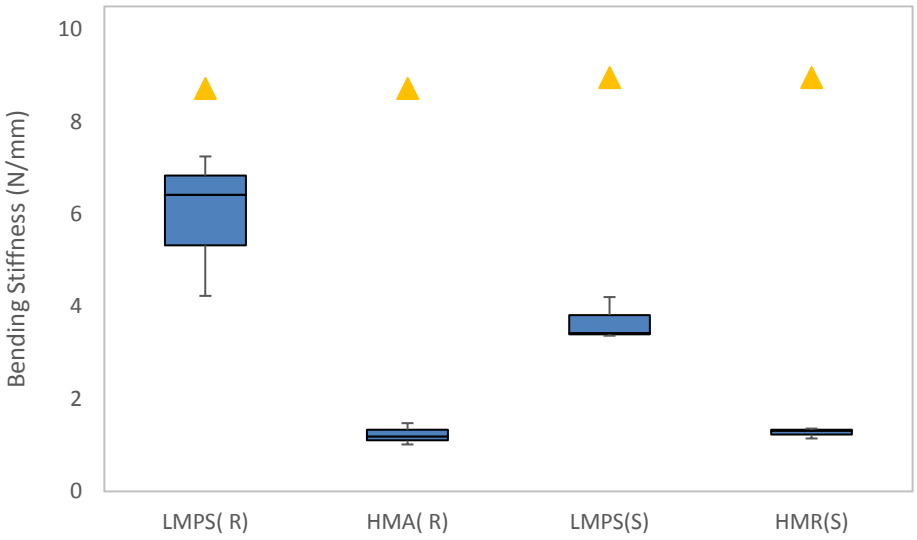

Figure 6.6 Box plot of experimental (blue rectangular) and theoretical (yellow triangle) bending stiffness for surface bonding modules in rigid state. HMA (R) and LMPS (R) represent a revolute joint employs HMA- and LMPS-based locking mechanism, respectively. HMA (S) and LMPS (S) indicate a spherical joint explores HMA- and LMPS-based locking mechanism, respectively.

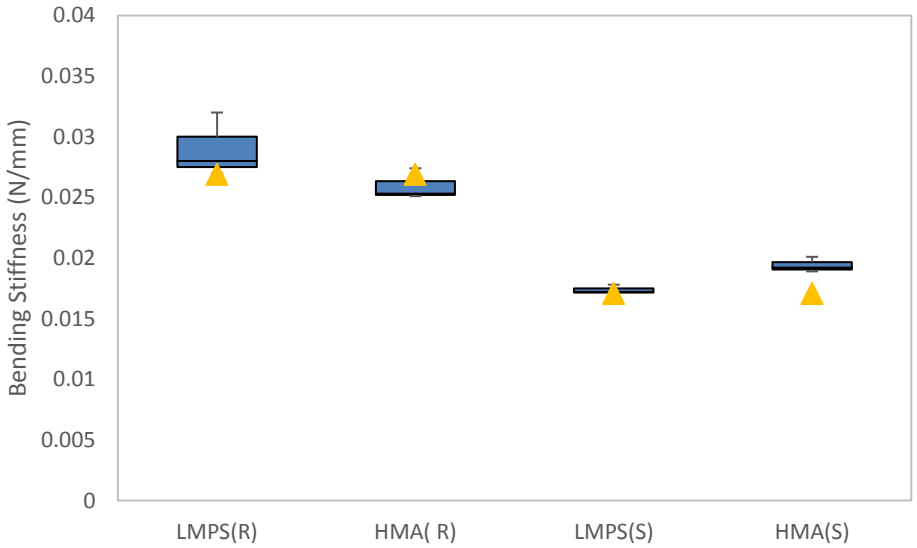

Figure 6.7 Box plot of experimental (blue rectangular) and theoretical (yellow triangle) bending stiffness for surface bonding modules in soft state. HMA (R) and LMPS (R) represent a revolute joint employs HMA- and LMPS-based locking mechanism, respectively. HMA (S) and LMPS (S) indicate a spherical joint explores HMA- and LMPS-based locking mechanism, respectively.

6.2.1.2 Phase Change Single Modules

The experimental setup for the lateral displacement test of phase change single modules is shown in Figure 6.8. The modules were tested in both rigid and soft state. An end-effector was designed and attached to the single

module. A cable was tied at the end-effector to attach the external loads. The deflection, as illustrated as "*D*" in Figure 6.8 (a) and (b), was defined as the change in position when supporting a load against gravity at the free end. Three trials were conducted, the average displacement was plotted in Figure 6.9 and Figure 6.10.

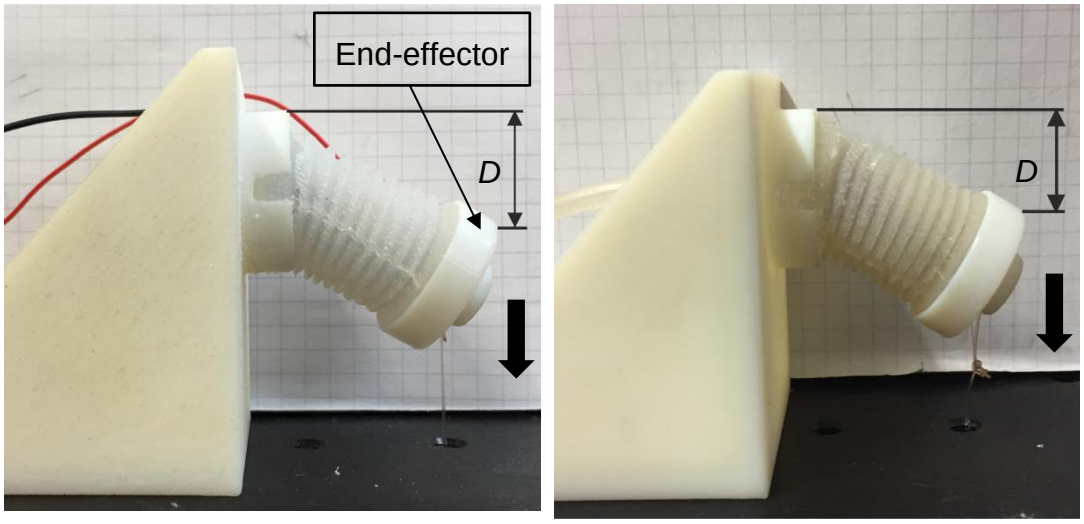

(a) (b)

Figure 6.8 Experimental setup for lateral displacement test. The direction of imposed displacement is illustrated by the black arrow. (a) LMPA-based single module. (b) GM-based single module. Displacement (D) is illustrated in the figure.

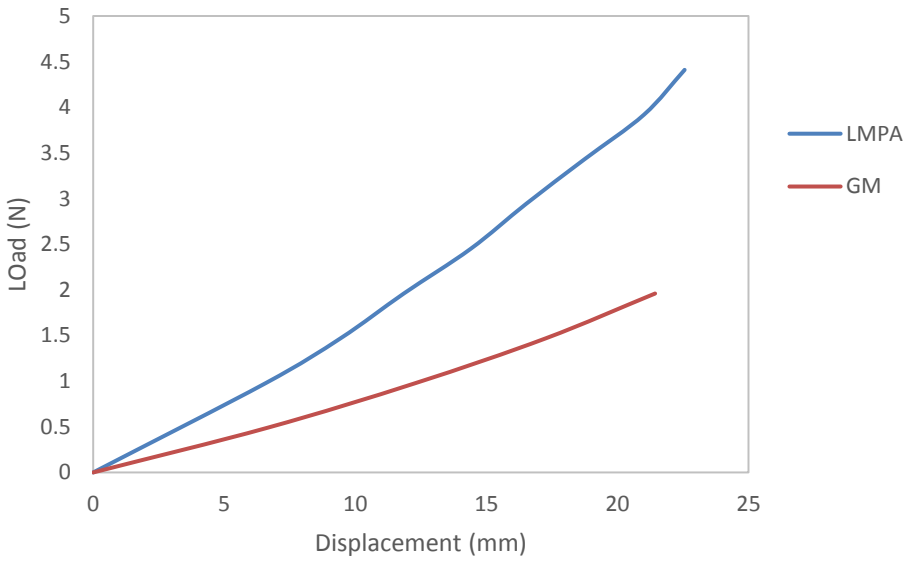

Figure 6.9 Load vs Displacement graph for LMPA- and GM-based single module in rigid state.

Figure 6.9 and Figure 6.10 illustrates the force requires deflecting the LMPA- and GM-based module in rigid state and soft state, respectively. A single

module without embedded controllable stiffness element (as illustrated as Empty in Figure 6.10) was fabricated as a comparison group. The results show that the force required to deflect LMPA-based module in rigid state is greater than the GM-based module. However, the force required to deflect LMPA-based module is smaller than its counterpart when the modules were in soft state. It is worth noticing that the force required to deflect the module without any controllable stiffness element (shown as 'Empty') is greater than the LMPA-based module in soft state.

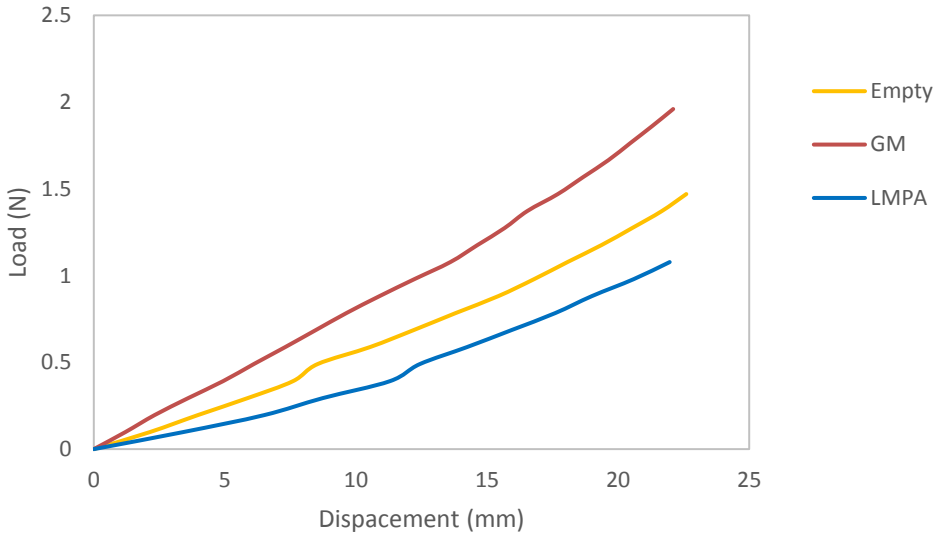

Figure 6.10 Load vs Displacement graph for LMPA- and GM-based single module in soft state.

The numerical values of bending stiffness for each design are presented in Table 6.2. These values were calculated when single modules were in rigid and soft state. The stiffness increase ratio for each design is indicated.

Table 6.2 Numerical Results from Lateral Displacement Test.

Design Method	**Bending stiffness in soft state** (N/mm)	**Bending stiffness in rigid state** (N/mm)	**Stiffness increase ratio** (rigid/soft)
Empty	0.0644±0.002	-	-
LMPA	0.0349±0.0015	0.2783±0.0199	8.0
GM	0.0803±0.0050	0.0896±0.0140	1.1

The results show that LMPA-based single module demonstrates higher bending stiffness increase than GM-based design approach. The single module without embedded controllable stiffness element has greater bending stiffness than LMPA-based module in soft state. This is possibly due to the temperature influence on the single module. The increased temperature has softened the silicone material. The detailed investigation will be presented in Section 6.3.

Based on the FEA simulations provided in Chapter 4, the calculated bending stiffness (rigid state) for LMPA- and GM-based single module are 0.2887 N/mm and 0.0753 N/mm, respectively. The bending stiffness for LMPA- and GM-based single module in the soft state are 0.0406 N/mm and 0.0661 N/mm, respectively. Theoretical and experimental bending stiffness of the modules in rigid state and soft state are illustrated in Figure 6.11 and Figure 6.12, respectively.

The results show that the FEA simulations closely predict the bending stiffness of LMPA-based module in rigid state, but overestimate the bending stiffness of LMPA-based module in soft state. Furthermore, the FEA simulation slightly underestimates the bending stiffness of GM-based module in rigid state and soft state.

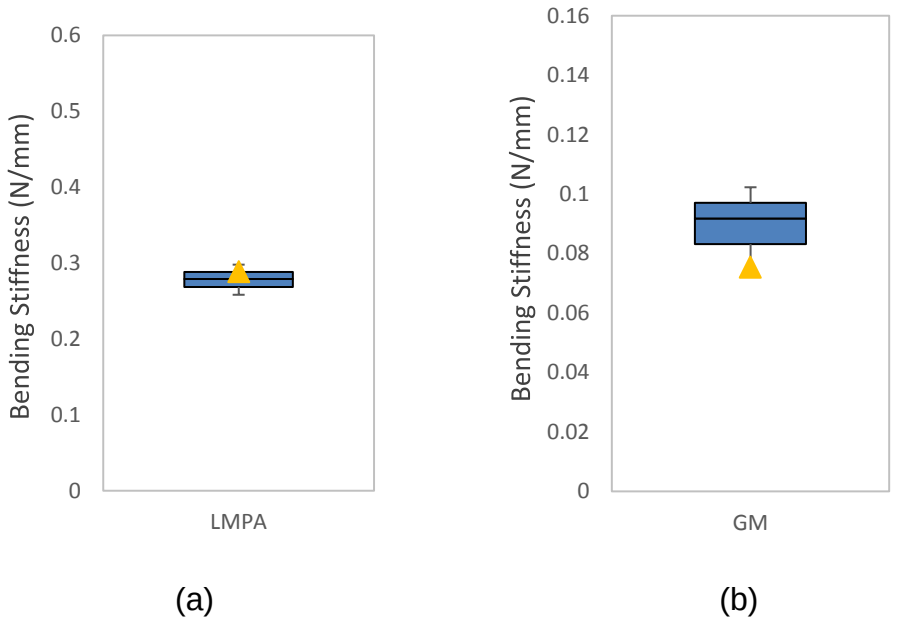

(a) (b)

Figure 6.11 Box plot of bending stiffness when LMPA- and GM-based single modules are in rigid state. (a) Experimental (blue rectangular) and theoretical (yellow triangle) bending stiffness of the LMPA-based single module. (b) Experimental (blue rectangular) and theoretical (yellow triangle) bending stiffness of the GM-based single module.

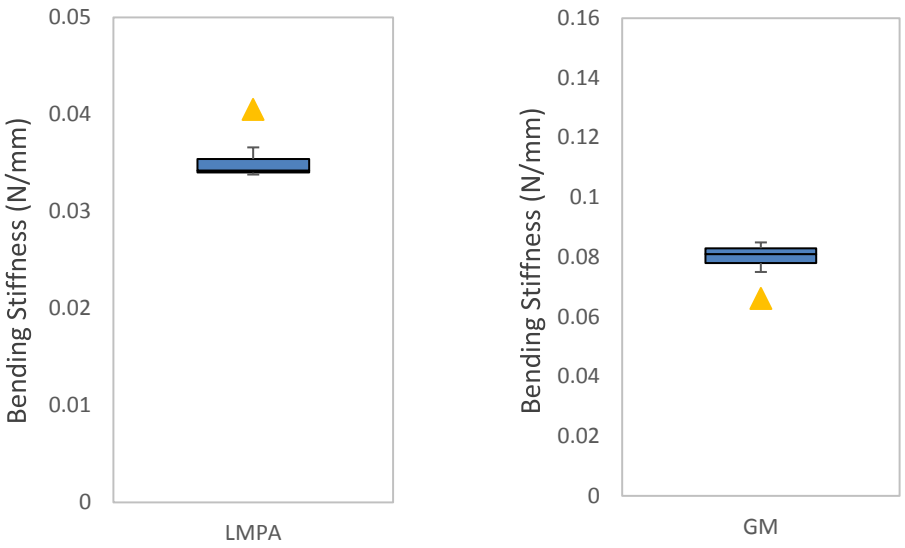

(a) (b)

Figure 6.12 Box plot of bending stiffness when LMPA- and GM-based single modules are in soft state. (a) Experimental (blue rectangular) and theoretical (yellow triangle) bending stiffness of the LMPA-based single module. (b) Experimental (blue rectangular) and theoretical (yellow triangle) bending stiffness of the GM-based single module.

The overestimation of the bending stiffness of LMPA-based module in soft state can be explained by understanding the assumption made in FEA simulations. The space occupied by the liquefied LMPA was assumed empty. The temperature influence and elastic modulus of the liquefied LMPA was not considered in the simulations. The temperature rise resulted from the liquefied LMPA could soften the silicone structure. The detailed explanation will be presented in Section 6.3. The theoretical FEA simulations are still useful to understand the upper limits on the bending stiffness of LMPA-based single module.

The results from the lateral displacement tests show GM- and LMPA-based design approaches cannot achieve a complete shape locking of the module, rather a remarkable stiffness increase.

All four design methods are seen to have a substantial stiffness increase. In comparison to the stiffness variation result from STIFF-FLOP group, which shows 36% stiffness increase (1.36 increase ratio) of the single module during the lateral displacement test [15], LMPS-, HMA-, and LMPA-based approaches were able to achieve the stiffness change respectively 150X, 35X, and 6X greater than the state of the art STFF-FLOP device.

6.2.2 Axial Displacement Test

In the axial displacement experiments, the stiffness of single module is characterised by the experimental elastic modulus. Linear regression curve was used to fit on the linear regional of the stress-strain graph. The experimental elastic modulus was calculated as the slope of the fitting curve. The experimental setup is shown in Figure 6.13. LMPA-based single module is illustrated in Figure 6.13 (a), GM-based single module is shown in Figure 6.13 (b). The direction of imposed displacement is illustrated in the figure as white arrow.

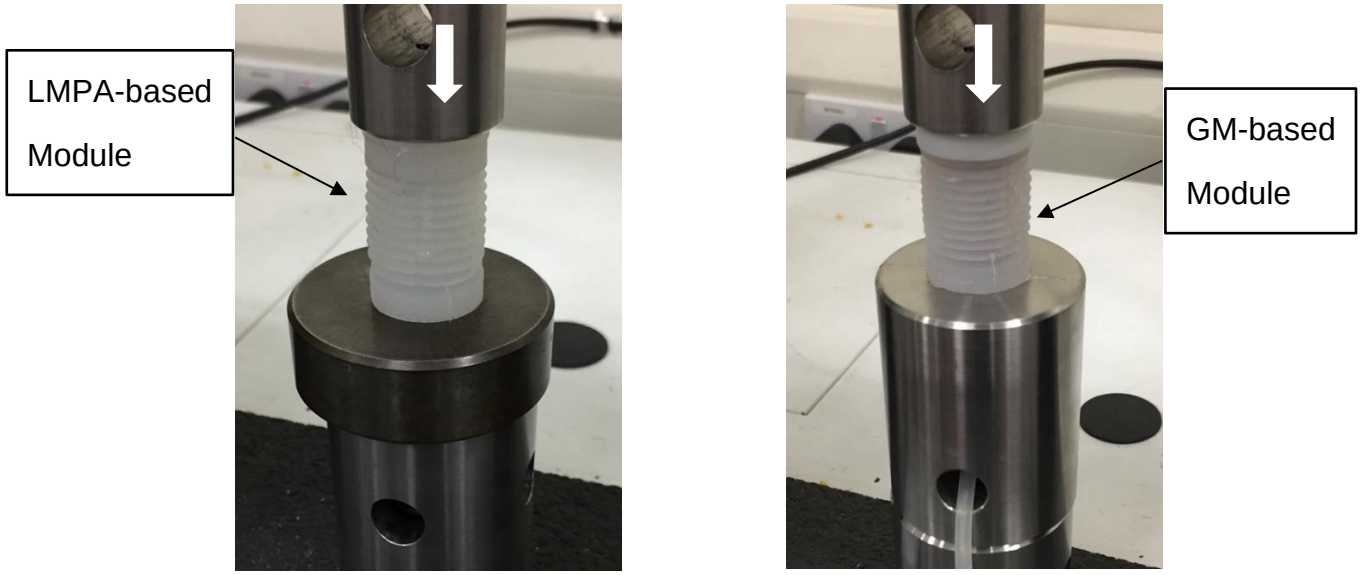

Figure 6.13 Experimental setup for axial displacement test. The direction of imposed displacement is illustrated by the white arrow. (a) LMPA-based single module. (b) GM-based single module.

The axial displacement tests were conducted when the modules were in rigid and soft phase. Each experiment was repeated three times. The stress-strain curves obtained from the axial displacement tests are shown in Figure 6.14 (GM-based module in rigid state), Figure 6.15 (GM-based module in soft state), Figure 6.16 (LMPA-based module in rigid state), and Figure 6.17 (LMPA-based module in soft state. Experimental elastic modulus of each design was determined from these figures.

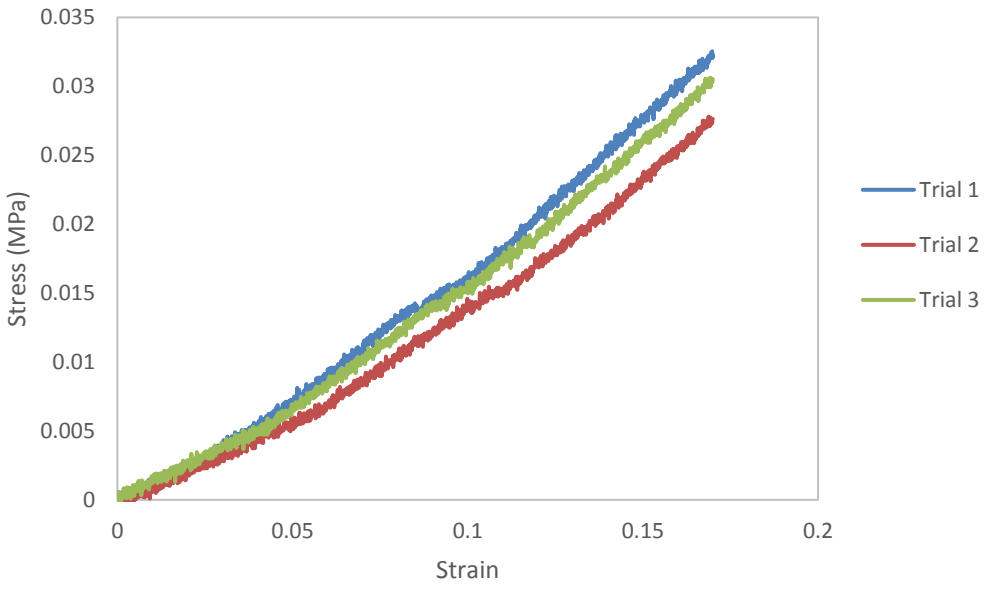

Figure 6.14 Stress-strain curve from axial displacement test (GM-based module in rigid state).

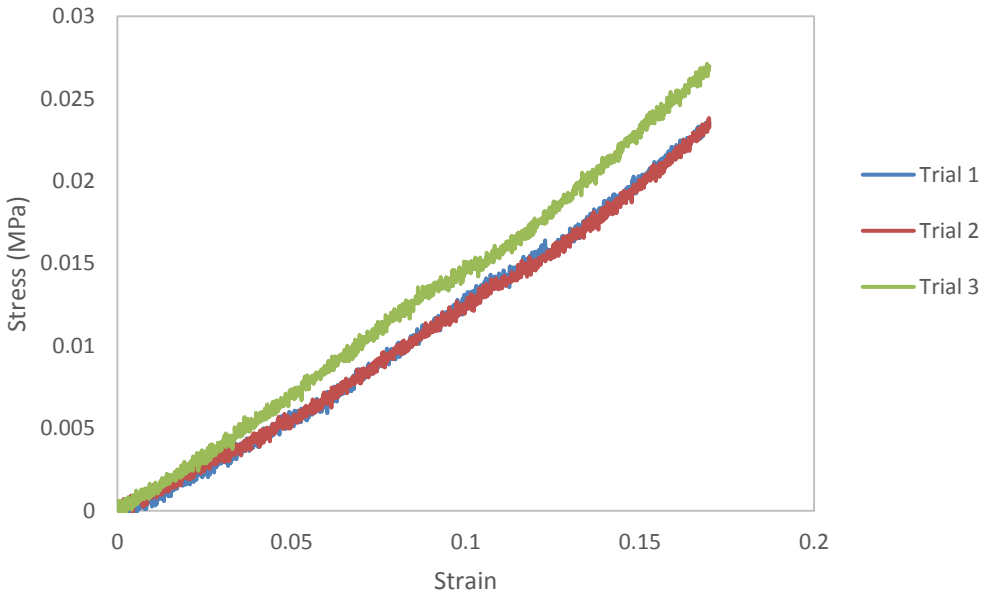

Figure 6.15 Stress-strain curve from axial displacement test (GM-based module in soft state).

It is worth noting that during low strain phase, the plots from Figure 6.14 and Figure 6.15 show a similar trend that results from compressing the external silicone components of the modules. During the axial testing, abrupt changes in the stiffness occurred due to the nature of the granular materials in the controllable stiffness element. If the external force is significant, the materials

that are pushed together by the vacuum pressure may start to separate, thus decreasing the stiffness.

The small slope appears in low strain phase, as plotted in Figure 6.16, results from the compression of the external silicone parts of the module. An abrupt change occurs when the resistant force of LMPA-based element starts to dominate. The force that requires deforming the module increases, a higher slope appears in the figure.

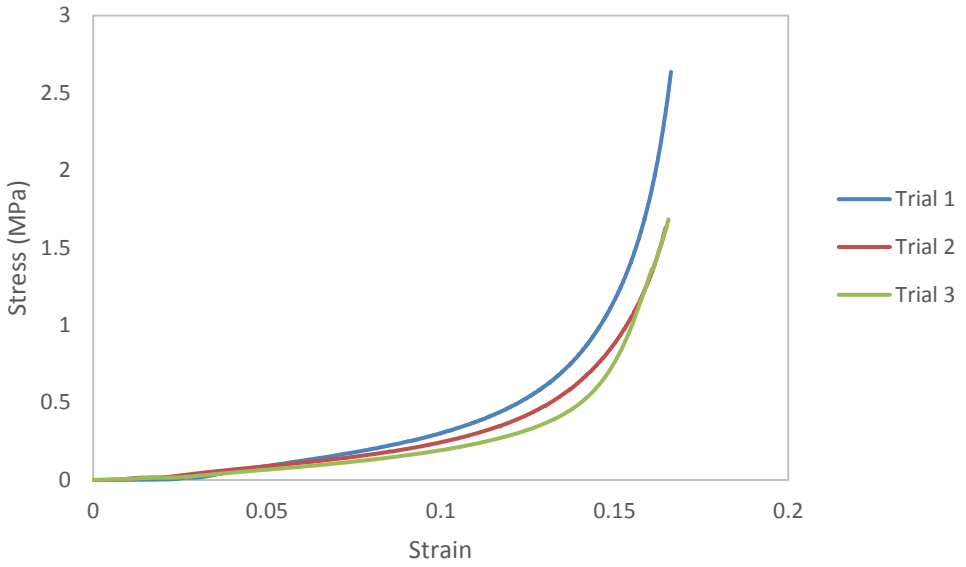

Figure 6.16 Stress-strain curve from axial displacement test (LMPA-based single module in rigid phase).

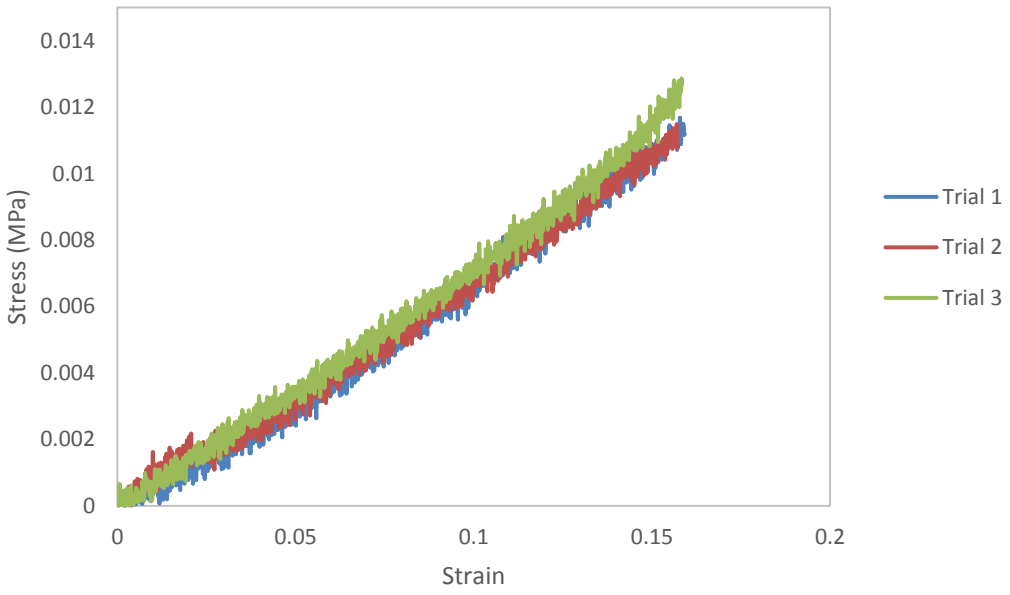

Figure 6.17 Stress-strain curve from axial displacement test (LMPA-based single module in soft phase).

The plots in Figure 6.16 and Figure 6.17 show that the force required to compress increases significantly when the controllable stiffness element is rigidified.

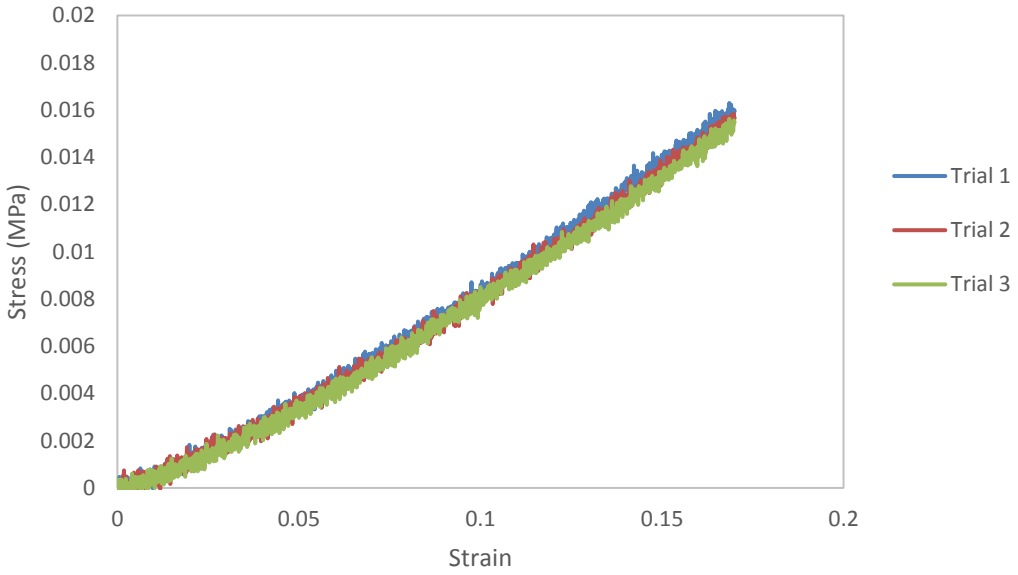

Figure 6.18 Stress-strain curve from axial displacement test (Single module without controllable stiffness element).

Axial displacement tests were conducted on the single module without the embedded controllable stiffness element. When LMPA-based single module in soft state, the controllable stiffness element is completely liquefied. The behaviour of the module, as plotted in Figure 6.17, shows a similar trend with single module without controllable stiffness element, as illustrated in Figure 6.18. The smaller slope of the stress-strain curve from Figure 6.17 can be explained by the increased temperature results in softening the silicone structure.

Table 6.3 Experimental Elastic Modulus of the Single Module.

Design method	**Elastic modulus in soft state** (MPa)	**Elastic modulus in rigid state** (MPa)	**Elastic modulus increase ratio** (rigid/soft)
LMPA	0.0753±0.0025	497.135±79.8677	6602.1
GM	0.1729±0.0003	0.2186±0.0010	1.3

Table 6.3 presents the calculated results for the experimental elastic modulus. As expected, the LMPA-based single module in rigid state has the largest

experimental elastic modulus. GM-based design approach, on the other hand, has limited elastic modulus increases. This situation could be improved by increasing the vacuum pressure (high pressure vacuum could be used). The result from Section 3.5 shows that when the vacuum pressure increases, the elastic modules of the granular materials increases as well. However, a substantial volume of the materials and high vacuum pressure may be used to increase the elastic modulus.

6.3 The Rise of Temperature on the Silicone Materials

To understand the rise of the temperature on silicone components when non-granular material devices in soft state, the following experiments were conducted. The test setup is shown in Figure 6.19.

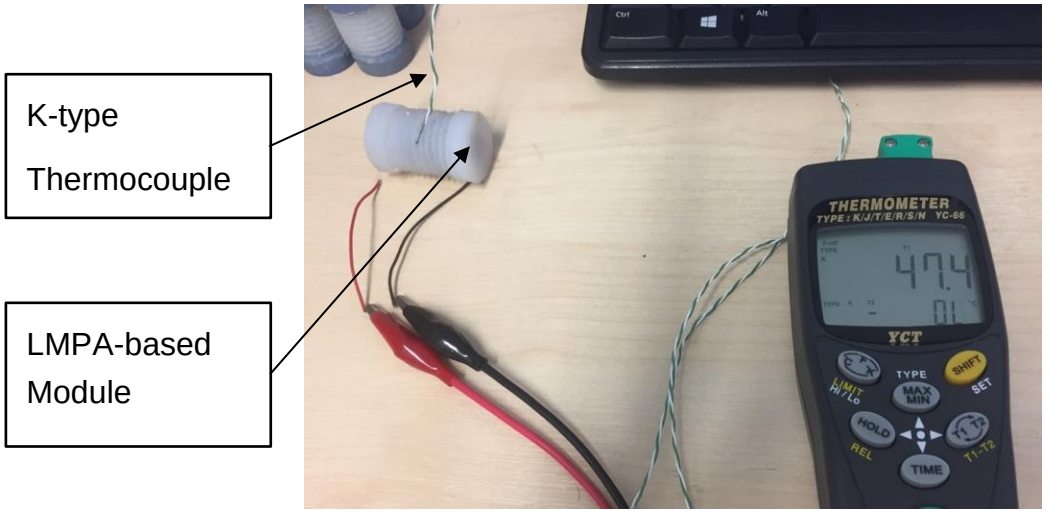

Figure 6.19 Experimental setup for understanding the rise of the temperature on the LMPA-based module.

A k-type thermocouple was used to attach the silicone component of the single module. The temperature was recorded every 15 seconds. The temperature was recorded when the module entered soft state (LMPS-, HMA-, and LMPA-based element was completely liquefied). The average power used to actuate the LMPS(R), HMA(R), LMPS(S), HMA(S), and LMPA-based element were 2.9 W, 3.7 W, 3.6 W, 2.7 W, and 8.8 W, respectively. Three trials were conducted, the average temperature of the silicone components when LMPS, HMA and LMPA modules enter liquefied state are 31.8 °C, 33.1 °C, 36.4 °C, 39.8 °C and 53.6 °C, respectively.

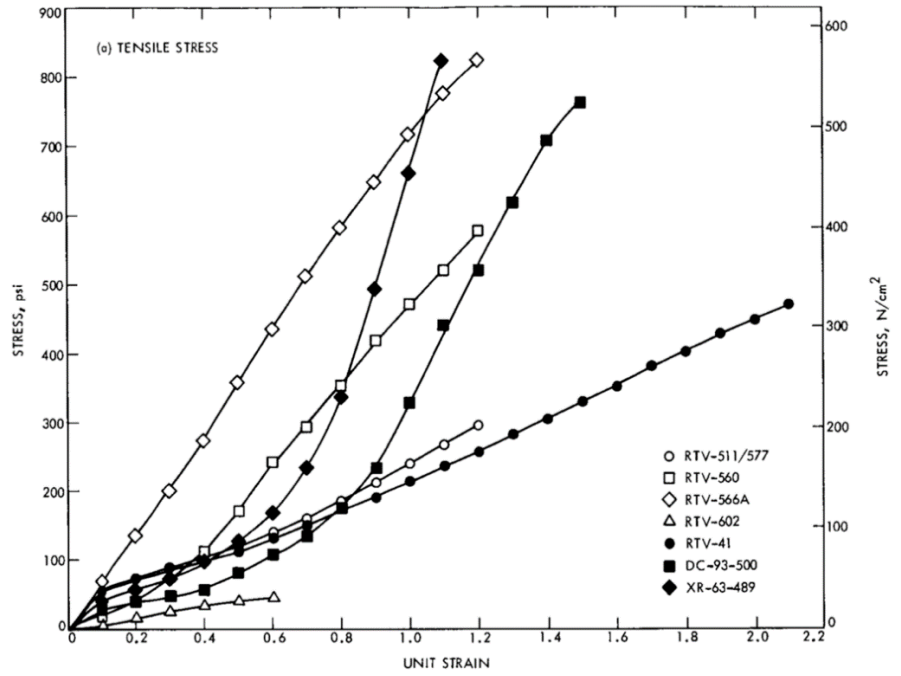

Figure 6.20 Stress vs strain of RTV silicone at 25 °C [82].

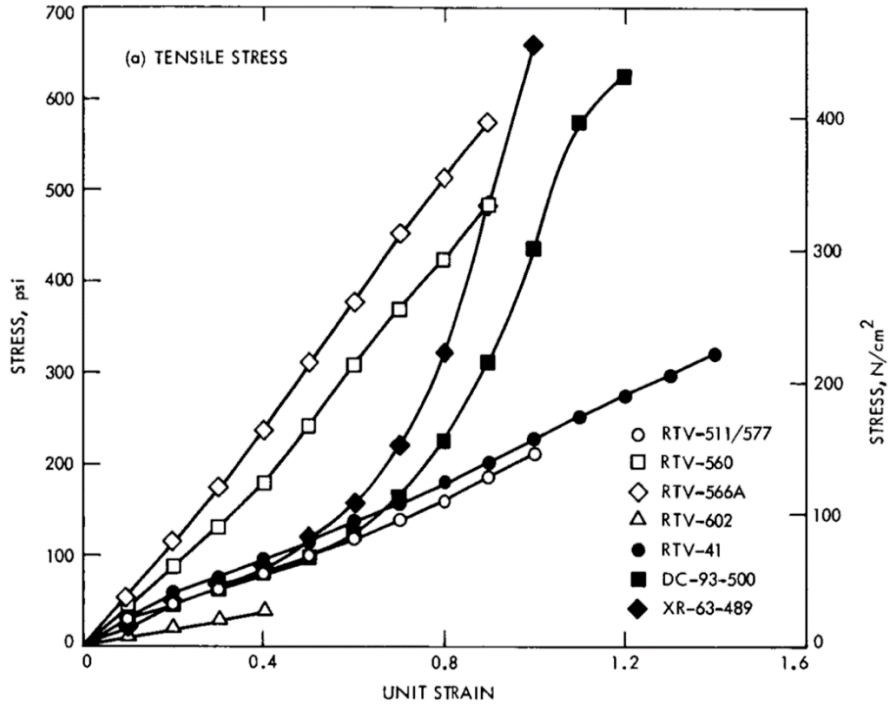

Figure 6.21 Stress vs strain of RTV silicone at 100 °C [82].

Figure 6.20 and Figure 6.21 show that stress vs strain of RTV silicone at 25 °C and 100 °C, respectively [82]. The elastic modulus of the RTV silicone can be estimated from the graphs. For example, when the temperature increased from 25 °C to 100 °C, the elastic modulus of RTV-511/577 and RTV-560 silicone decreased by ~ 35%. The linear dependence of the elastic modulus

on temperature can be predicted by the theromdymanic law [83]. The elasic modulus of the silicone is given,

$$E = \frac{3}{2} k \cdot T \cdot \rho_K \qquad 6.2$$

where *k* stands for the Boltzman constant, *T* for the temperature, and ρ_K for the degree of cross-linking [83]. The linear dependence of the elastic modulus on temperature could explain the difference (16.37%) between the simulation result and experimental bending stiffness of LMPA-based single module in soft state as well as the stiffness difference between single module without embedded controllable stiffness element and LMPA-based module in soft state.

The theoretical FEA simulation assumed the temperature influence on the silicone rubber material was negligible. However, Figure 6.20 and Figure 6.21 demonstrate the temperature influence on elastic modulus of RTV materials. The rise of temperature can decrease the elastic modulus of the material. The linear dependence of bending stiffness on elastic modulus can be explained by,

$$k = \frac{AE}{L}$$

where *A* is the cross-sectional area, *E* is the elastic modulus, and *L* is the length of the element.

Therefore, the linear dependence of bending stiffness on temperature can be predicted. Since Figure 6.20 and Figure 6.21 have demonstrated when the temperature increases from 25 °C to 100 °C, the elastic modulus decreases by ~ 35%, one can predict when the temperature increases from 25 °C to 53.6 °C (measured temperature of LMPA-based module), bending stiffness could be decreased by ~ 17.5%. The discrepancy (16.37%) between the simulation result and the experimental result can be explained. Further investigation on the temperature influence on Ecoflex 0030 and Drag Skin 30 will be conducted in the future.

6.4 Response Time Validation of Single Module

Response time defined here as the time for a single module to transition between rigid phase and soft state. The softening time and rigidifying time are defined in this section to characterise the response time for the single modules.

6.4.1 Softening Time

For the GM-based single module, the softening time is defined as the time between the vacuum switched off and when single module reached a flexible configuration. Because the transition time can be rapid, the experiments were recorded and softening time was determined by analysing the video frame by frame. For the rest of the designs, single modules were cantilevered in rigid state, and weight (500 grams) was hung from its free end. The softening time is defined as the time between when the resistance heater is activated to when the module is soft and flexible. Three trials were conducted. The power consumption and vacuum pressure that were used to activate the module are listed in the first row of Table 6.4, the softening time is presented in the second row.

Table 6.4 Power Consumption and Softening Time of Each Design. HMA (R) and LMPS (R) represent a revolute joint that employs HMA- and LMPS-based locking mechanism, respectively. HMA (S) and LMPS (S) indicate a spherical joint that explores HMA- and LMPS-based locking mechanism, respectively.

	LMPS(R)	**HMA(R)**	**LMPS(S)**	**HMA(S)**	**LMPA**	**GM**
Power	2.9±0.2 W	3.7±0.4 W	3.6±0.1 W	2.7±0.5 W	8.8±1.0 W	180 mmHg
Time (s)	13.0±3.9	8.0±1.5	29.4±7.8	18.6±2.5	63.3±7.1	0.2

For GM-based single module, the time required to soften the module is 0.2 seconds. It was the fastest among five tested modules. It took 63.3±7.1 seconds for LMPA-based controllable stiffness element to transition from solid-like state to liquid-like state. It was the slowest among five tested modules. This is in line with theoretical estimation. The design can be mitigated by decreasing the diameter of the controllable stiffness element, therefore reducing the mass of the element. The LMPS- and HMA-based revolute joints reacted faster than the spherical joint. Furthermore, HMA is faster to soften than LMPA. This is due to the temperature influence on the bonding materials. (The bonding strength of HMA declined exponentially when the temperature increased, whereas the bonding strength of LMPS decreased steadily). HMA-based single module can exploit this characteristic by increasing the external loads to further shorten the softening time.

6.4.2 Rigidifying Time

For the GM-based single module, the test for determining rigidifying time was undertaken by placing the module from a horizontal position and recording the time between vacuum activated and when the module reached a rigid configuration. The time was determined by parsing individual video frames. For the rest of the designs, the rigidifying time was measured as the time between when the resistance heater is turned off, and the module is rigid. This was done by manually pushing the module until it was rigid, and time was recorded accordingly. The numerical results are presented in Table 6.5.

Table 6.5 Rigidifying Time of Each Design. HMA (R) and LMPS (R) represent a revolute joint that employs HMA- and LMPS-based locking mechanism, respectively. HMA (S) and LMPS (S) indicate a spherical joint that explores HMA- and LMPS-based locking mechanism, respectively.

	LMPS(R)	**HMA(R)**	**LMPS(S)**	**HMA(S)**	**LMPA**	**GM**
Time (s)	7.8±1.9	42.7±7.2	18.5±2.8	30.2±5.8	114.2±27.8	0.2

The result shows that the GM-based single module has the quickest rigidifying time, whereas LMPA-based design has the slowest rigidifying time. This is due to the large amount of the mass of LMPA in the single module. LMPS-based design approach is faster to solidify than HMA-based method. The measured results are not representative of the limits of the proposed methods. Since there are no temperature sensors in the current design, the modules can be easily overheated. As a result, the rigidifying time can be affected.

6.5 Failure Modes

It is important to understand the limits of the design before failure occurs. For surface bonding approach, two main failure mechanisms were observed during the experiments. The detachment of the copper tapes from plastic components occurred before the break of the bond formed by LMPS or HMA. This can be mitigated by using high shear strength adhesive (The shear strength of adhesive is greater than the bonding materials) with high temperature resistance (above 80 °C). For the spherical joint, the failure occasionally occurred when the link broke before the separation of the bond during the lateral displacement tests. This can be improved by using high

Young's Modulus of the material to construct the link or increasing the diameter of the link.

For LMPA-based single module, the increased external load can lead to the detachment of the controllable stiffness element from the bottom silicone cap. The cap cannot fully support the embedded LMPA during the bending. This can be mitigated by using high Shore hardness silicone material and decreasing the diameter of the controllable stiffness element.

6.6 Summary

This chapter presented the experimental characterisation of the single module, with emphasis on the increase in stiffness and the response time. Failure modes were discussed in the end.

- Lateral displacement tests were conducted to characterise the bending stiffness of each design. For surface bonding design approach, the experimental results indicate that modules employs the LMPS-based locking mechanism have better stiffness than HMA-based locking mechanism, and it is closer to achieve a complete shape lock. For phase change design method, LMPA-based single module demonstrated a significant stiffness increase ratio (8.0 ratio). In contrast, GM-based single module showed a minor increase in stiffness ratio (1.1 ratio).
- Axial displacement tests were conducted on LMPA- and GM-based single module to characterise the experimental elastic modulus. As expected, LMPA-based demonstrated the highest elastic modulus (497.135±79.8677 MPa) and highest increase ratio in elastic modulus (6602.1 ratio). GM-based module, on the other hand, showed a minor elastic modulus increase, only 26.43%. In comparison with the results from STIFF-FLOP project, where the elastic constant increase is seen to be 75.7% (no chamber inflation). This is due to the different vacuum pressure used in the experiments, 0.024 MPa with respect to 0.098 MPa (STIFF-FLOP).
- The conclusion draw from lateral and axial displacement tests is that all four design approaches cannot achieve a complete shape lock, rather a significant increase in stiffness. The results show that the proposed design methods can modulate the stiffness when required. This is an important capability for hard and soft robot to be utilized in variable environments.
- Response time was interrupted as the time for a single module to transition between rigid phase and soft state. Softening time and rigidifying time were defined in this chapter to quantifiably measure the response time of each design. The results show that GM-based single module demonstrated the

quickest response time in terms of softening and rigidifying time. LMPS- and HMA-based module showed reasonable response time, this can be further improved by decreasing the mass of the bonding materials.

- For surface bonding single modules, two main failure mechanisms were observed during the lateral displacement experiments. The detachment of the copper tapes from plastic components is the main source of the failure for surface bonding single modules. In addition, the link of the joint occasionally breaks when the external load is significant. For phase change single modules, the detachment of the controllable stiffness elements from the bottom silicone cap is the main reason of failure.

Chapter 7
Conclusions and Future Work

This chapter details the conclusions draw from the experimental characterisation of the single modules and recommendations for further research.

7.1 Assessment of Research Objectives

This section identifies the methodologies applied during the research.

7.1.1 To Identify the Possible Materials that Can be Used for the Development of the Controllable Stiffness Mechanism.

Four materials (i.e. low melting point solder, hot-melt adhesive, low melting point alloy, and granular material) that can be used for the design of the controllable stiffness mechanism were identified in Chapter 2. These materials have relatively fast transition time and good relative stiffness change. They can transition between solid-like state and liquid-like state. This characteristic can be exploited for the development of the controllable stiffness element.

7.1.2 To Investigate the Properties of the Identified Materials Related to the Design of the Controllable Stiffness Mechanisms.

The properties of four materials were investigated in Chapter 3. The experimental methods were used to characterise the relevant properties. Solidus temperature was measured for low melting point solder, hot-melt adhesive and low melting point alloy. This was used to estimate the solidified time. Temperature influence on the bonding strength was tested on low melting point solder and hot-melt adhesive. The understanding of this property can reduce the response time of the single module. The selection of the adherend can affect the bonding strength of the hot-melt adhesive. Different choices of the adherend were investigated, copper was selected as adherend for hot-melt adhesive. Compression tests were conducted on low melting point alloy and granular material, and tensile tests were carried out on silicone rubber materials. Hyperelastic fitting models were produced. These were used to estimate the stiffness of the single module in rigid and soft state. Finally, the repeatability of the materials was tested on low melting point solder and hot-melt adhesive. The change of the bonding strength over repetitions was analysed.

7.1.3 To Design the Controllable Stiffness Mechanism that Can be Employed by the Single Module.

Design and analysis of the controllable stiffness single module were presented in Chapter 4. Design of the single module was broken down into two categories: design of surface bonding modules (LMPS- and HMA-based single module) and design of phase change modules (LMPA- and GM-based single module). Rigid revolute and spherical joints were developed to employ the LMPS- and HMA-based locking mechanisms. Furthermore, LMPA- and GM-based controllable stiffness elements were designed to be embed into the soft modules. FEA simulations were carried out to estimate the bending stiffness of the single modules and to optimise the silicone bellows-like structures.

7.1.4 To Experimentally Characterise the Performance of the Single Module With Emphasis on Measurement of Stiffness and Response Time.

The fabricated single modules were experimentally characterised in Chapter 6. The characterisation was focused on the stiffness change and response time of each design.

7.2 Summaries

The following summaries of results are drawn from the work carried out in this research:

7.2.1 LMPS-based Single Module

The proposed single module consisted of a silicone bellows-like structure and a thermally activated joint. A LMPS-based thermally activated mechanism was developed. The mechanism consisted of a resistive heater, and a layer of LMPS sandwiched between two copper tapes. Revolute and spherical joints were designed to fully explore the locking mechanism.

7.2.1.1 Bending Stiffness

Lateral displacement tests were conducted on the single modules in the rigid and soft state. The results showed that the proposed designs experienced a significant increase ratio in stiffness: 205.8 and 215.8 increase ratio for revolute and spherical joint, respectively.

7.2.1.2 Response Time

Response time (i.e. softening time and rigidifying time) was defined in this study as the time for a single module to transition between rigid phase and soft state. The measured softening time for the revolute joint, and spherical joint were 13.0±3.9s and 29.4±7.8s, respectively. The measured rigidifying time for the revolute joint and spherical joint were 7.8±1.9s and 18.5±2.8s, respectively.

7.2.2 HMA-based Single Module

The proposed single module consisted of a silicone bellows-like structure and a thermally activated joint. An HMA-based locking mechanism was developed under this context. The mechanism consisted of a resistive heater, and a layer of HMA sandwiched between two copper tapes. Revolute and spherical joints were developed to fully explore the locking mechanism.

7.2.2.1 Bending Stiffness

Lateral displacement tests were conducted to characterise the bending stiffness of the single module. The results indicated that single module that utilized HMA-based locking mechanism showed a remarkable increase in bending stiffness: 47.2 and 60.7 increase ratio for revolute and spherical joint, respectively.

7.2.2.2 Response Time

The measured softening time for the revolute joint and the spherical joint are 8.0±1.5s and 18.6±2.5s, respectively. The measured rigidifying time for the revolute joint and spherical joint are 42.7±7.2s and 30.2±5.8s, respectively. In comparison to the modules that employ LMPS-based locking mechanism, single modules that utilized HMA-based locking mechanism are quicker to be unlocked (from solid-like state to liquid-like state), but they took longer time to be locked.

7.2.3 LMPA-based Single Module

The proposed single module was composed of a silicone structure and a LMPA-based controllable stiffness element.

7.2.3.1 Bending Stiffness

Lateral displacement experiments were conducted to characterise the bending stiffness of the single module in the soft and rigid state. The results showed that the module demonstrated a reasonable increase ratio in bending stiffness (8 increase ratio).

7.2.3.2 Elastic Modulus

Axial displacement tests were carried out to estimate the elastic modulus of the LMPA-based single module in the soft and rigid state. As expected, the module demonstrated a significant increase ratio in elastic modulus (6602.1 increase ratio). Theoretical models were validated throughout the experiments. The results showed that the theory closely predicts the elastic modulus for the LMPA-based single module in the soft and rigid state.

7.2.3.3 Response Time

The measured softening time and rigidifying time for the LMPA-based single module are 63.3±7.1s and 114.2±27.8s. LMPA-base single module has the slowest response time compared to the rest of the designs. Given the amount of the mass used in the LMPA-based controllable stiffness element, this was in line with theoretical prediction.

7.2.4 GM-based Single Module

The module consisted of a silicone structure and GM-based controllable stiffness element.

7.2.4.1 Bending Stiffness

Lateral displacement experiments were performed to evaluate the bending stiffness of a GM-based single module. The tests were carried out with and without activating the controllable stiffness element. Although the stiffness increase was not optimal (1.1 increase ratio), the module demonstrated the capability of modulating stiffness when required.

7.2.4.2 Elastic Modulus

Axial displacement experiments were conducted on the single module to evaluate the elastic modulus. The tests were performed when the controllable stiffness element was activated and when it was not. The results showed that the computed elastic modulus increased slightly (1.3 increase ratio). Although the increase was not optimal, the system was able to provide stiffness variation in different directions (vertical and horizontal).

7.2.4.3 Response Time

For the GM-based single module, the transition time of granular materials was rapid. The softening and rigidifying time were both 0.2s. In terms of response time, GM-based single module enjoyed a decided advantage with respect to the LMPS-, HMA-, and LMPA-based single module.

7.3 Conclusions and Future Work

This research has presented the synthesis, design and analysis of the controllable stiffness single module for a modular manipulator. Four materials were proposed to design the controllable stiffness mechanisms. The fabrication of the components of the single modules has been detailed. Extensive characterisations of the selected materials and the performances of the modules have been provided. The theoretical FEA models were developed and validated through experimental tests.

Due to the extensive materials used in this study, experimental approaches were used to evaluate the properties of the materials and the performances of the single modules. However, the analytic models were developed, and FEA simulations were performed to optimise the design parameters. These results were validated through experiments. Future research is required to develop detailed FEA models to accurately predict the response time of each design.

In parallel to more accurate modelling, integration of temperature sensors will play an important role in modulating the stiffness of the module. Furthermore, the integration of sensors in the module could help understand the precise moment when the module enters the soft phase, as well as preventing overheating. Future work will address the need for the sensing elements.

LMPS-, HMA-, LMPA-, and GM-based controllable stiffness mechanisms were introduced to modulate the overall stiffness of the module. LMPS-, HMA-, and LMPA-based approaches demonstrated a significant increase in bending stiffness, LMPS-based module was found to achieve a stiffness change 150X greater than the state of the art granular material approach, whereas GM-based methods showed a minor increase than its counterparts. Although the increase was not optimal, GM-based single module was able to provide stiffness variation in different directions (vertical and horizontal). Future research will improve the designs through the optimisations of the controllable stiffness elements (i.e. non-cylindrical shape element and membrane material). In addition, by reducing the amount of the mass used in thermally activated joint, the slow response time can be mitigated, as well as lowering the rise of the temperature in silicone materials.

Surface bonding modules are suitable for missions where high strength is required (i.e. manipulation and extraction). The results show that surface bonding modules were able to support a payload equal to more than 25X of its own weight. In addition, phase change modules demonstrated high

dexterity in terms of bending and compression. These modules have a highly compressible structure, which allows them to operate in the environment where the diameter of the insertion port is smaller than their nominal diameters. The soft silicone structures prevent the damage to the working environments. The capability of stiffening enables the modules to interact the environment efficiently. Future research is required to construct a snake-like manipulator based on the proposed single modules to perform various missions.

List of References

1. C. Wright, A. Buchan, B. Brown, J. Geist, M. Schwerin, D. Rollinson, M. Tesch, and H. Choset, “Design and architecture of the unified modular snake robot,” in *Proc. IEEE Int. Conf. Robot. Autom*., 2012, pp. 4347–4354.
2. C. Wright, A. Johnson, A. Peck, Z. McCord, A. Naaktgeboren, P. Gianfortoni, M. Gonzales-Rivero, R. Hatton, H. Choset, ‘‘Design of modular snake robot,’’ in *Proc. IEEE Int. Conf. Intell. Robots Syst*., 2007, pp. 2609–2614.
3. D. Trivedi, C. D. Rahn, W. M. Kier, and I. D. Walker, “Soft robotics: Biological inspiration, state of the art, and future research,” *Appl. Bionics Biomech*., vol. 5, pp. 99–117, 2008.
4. W. M. K. D. Trivedi, C. D. Rahn, and I. D. Walkerca, “Soft robotics: Biological inspiration, state of the art, and future research,” *Appl. Bionics Biomech*., vol. 5, no. 3, pp. 99–117, 2008.
5. N. Simaan, R. Taylor, and P. Flint, "High Dexterity Snake-like Robotic Slaves for Minimally Invasive Telesurgery of the Upper Airway," in *Int. Conf. on Medical Image Computing and Computer- Assisted Intervention*, St. Malo, France, 2004, pp. 17-24.
6. N. Simaan, R. Taylor, and P. Flint, “A dexterous system for laryngeal surgery,” in *Proc. IEEE Int. Conf. Robot. Autom*., New Orleans, LA, Apr. 2004, pp. 351–357.
7. A. Degani, H. Choset, A. Wolf, and M. A. Zenati, "Highly Articulated Robotic Probe for Minimally Invasive Surgery," in *IEEE Int. Conf. Robot. Autom*., Orlando, Florida, 2006, pp. 4167- 4172.
8. A. Degani, H. Choset, A. Wolf, T. Ota, and M. A. Zenati, "Percutaneous Intrapericardial Interventions Using a Highly Articulated Robotic Probe," in *IEEE / RAS-EMBS Int. Conf. on Biomedical Robotics and Biomech*., Pisa, Italy, 2006, pp. 7-12.
9. M. Manti, V. Cacucciolo, and M. Cianchetti. Stiffening in soft robotics: A review of the state of the art. *IEEE Robot. Autom*., vol. 23, no. 3, pp. 93–106, 2016.
10. C. Majidi and R. J. Wood, “Tunable elastic stiffness with micro-confined magnetorheological domains at low magnetic field,” *Applied Physics Letters*, vol. 97, no. 16, p. 164104, 2010.
11. B. Liu, S.A. Boggs, and M.T. Shaw. “Electrorheological Properties of Anisotropically Filled Elastomers”. *IEEE Trans. DEI*, vol. 8, no. 2, pp. 173- 181, April 2001.
12. N. Cheng, G. Ishigami, S. Hawthorne, C. Hao, M. Hansen, M. Telleria, R. Playter, and K. Iagnemma, “Design and analysis of a soft mobile robot composed of multiple thermally activated joints driven by a single actuator,” in *Proc. IEEE Int. Conf. Robot. Autom*., Anchorage, AK, USA, May 2010, pp. 5207–5212.
13. M. Telleria, M. Hansen, D. Campbell, A. Servi,and M. Culpepper,“Modeling and implementation of solder-activated joints for single-actuator, centimeter-scale robotic mechanisms,” in *Proc. IEEE Int. Conf. Robot*. Autom., Anchorage, AK, USA, May 2010, pp. 1681–1686.
14. N. G. Cheng, M. B. Lobovsky, S. J. Keating, A. M. Setapen, K. I. Gero, A. E. Hosoi, and K. D. Iagnemma, “Design and analysis of a

robust, low-cost, highly articulated manipulator enabled by jamming of granular media," in *Proc. IEEE Int. Conf. Robot. Autom*., May 2012, pp. 4328 –4333.

15. M. Cianchetti, T. Ranzani, G. Gerboni, I. D. Falco, C. Laschi, A. Menciassi, "STIFF-FLOP Surgical Manipulator: mechanical design and experimental characterization of the single module", *IEEE/RSJ Int. Conf. Intell. Robots Syst*., 2013, pp. 3576-3581.
16. T. Ranzani, M. Cianchetti, G. Gerboni, I. D. Falco, and A. Menciassi, 'A Soft Modular Manipulator for Minimally Invasive Surgery: Design and Characterization of a Single Module', *IEEE Trans. Robot*., vol. 32, no. 1, pp. 187–200, Feb. 2016.
17. B. E. Schubert and D. Floreano, "Variable stiffness material based on rigid low-melting-point-alloy microstructures embedded in soft polydimethylsiloxane (PDMS)," *RSC Advances*, vol. 3, no. 46, pp. 24671–24679, 2013.
18. N. G. Cheng, A. Gopinath, L. Wang, K. Iagnemma, and A. E. Hosoi, "Thermally tunable, self-healing composites for soft robotic applications," *Macromolecular Materials and Engineering*, vol. 299, no. 11, pp. 1279-1284, 2014.
19. J. Shintake, B. Schubert, S. Rosset, H. Shea, and D. Floreano, "Variable stiffness actuator for soft robotics using dielectric elastomer and low- melting-point alloy," in *Proc. IEEE/RSJ Int. Conf. Intell. Robots Syst*., 2015, pp. 1097–1102.
20. OCRobotics. *Snake-arm Robots [Online]*. Available: http://www.ocrobotics.com/technology-/snakearm-robots/.
21. J. Shang, C. J. Payne, J. Clark, D. P. Noonan, K.-W. Kwok, A. Darzi, and G.-Z. Yang, "Design of a multitasking robotic platform with flexible arms and articulated head for minimally invasive surgery," in *Proc. IEEE/RSJ Int. Conf. Intell. Robot. Syst*., 2012, pp. 1988–1993.
22. K.-W. Kwok, K. H. Tsoi, V. Vitiello, J. Clark, G. Chow, W. Luk, and G.-Z. Yang, "Dimensionality reduction in controlling articulated snake robot for endoscopy under dynamic active constraints," *IEEE Trans. Robot*., vol. 29, no. 1, pp. 15–31, Feb. 2013.
23. K. Ikuta, S. Daifu, T. Hasegawa and H. Higashikawa, "Hyper-finger for Remote Minimally Invasive Surgery in Deep Area," in *Proc. of Medical Image Computing and Computer Assisted Intervention*, 2002, pp.173-181.
24. C. Ishii, K. Kobayashi, Y. Kamei, and Y. Nishitani, "Robotic forceps manipulator with a novel bending mechanism," *IEEE/ASME Trans. Mechatronics*, vol. 15, no. 5, pp. 671–684, Oct. 2010.
25. C. Ishii and K. Kobayashi, "Development of a New Bending Mechanism and its Application to Robotic Forceps Manipulator," in *Proc. 2007 IEEE Int. Conf. on Robot. Autom*., Roma, Italy, 2007, pp. 599-604.
26. I C. Ishii and K. Kobayashi, "Development of a New Robotic Forceps Manipulator for Minimally Invasive Surgery and Its Control," in *Proc. SICE-ICASE Int. Joint Conf*, 2006, pp. 250-253.
27. I. D. Walker, "Continuous backbone "continuum" robot manipulators," *ISRN Robot*., vol. 2013, pp. 1–19, 2013.

28. J. S. Mehling, M. A. Diftler, M. Chu, and M. Valvo, “A min- imally invasive tendril robot for in-space inspection,” in *Proc. IEEE/RAS-EMBS Int. Conf. Biomed. Robot. Biomechatron*., 2006, pp. 690–695.
29. H. Y. Hu, P. F. Wang, B. Zhao, et al. "Design of a novel snake-like robotic colonoscope," in *Proc. IEEE Int. Conf. Robot*. Biomimetics, Guilin, 2009, pp. 1957- 1961.
30. I. A. Gravagne and I. D. Walker, “Large deflection dynamics and control for planar continuum robots,” *IEEE/ASME Trans. Mechatron*., vol. 8, no. 2, pp. 299–307, Jun. 2003.
31. Q. Zhao and F. Gao, "Design and Analysis of a Kind of Biomimetic Continuum Robot", in *Proc. IEEE Int. Conf. Robot. Biomimetics*, Tianjin, China, 2010, pp. 1316-1320.
32. N. Simaan, “Snake-like units using flexible backbones and actuation redundancy for enhanced miniaturization,” in *Proc. IEEE Int. Conf. Robot. Autom*., Barcelona, Spain, Apr. 2005, pp. 3023–3028.
33. N. Simaan, K. Xu, W. Wei, A. Kapoor, P. Kazanzides, R. H. Taylor, and P. Flint, “Design and Integration of a Telerobotic System for Minimally Invasive Surgery of the Throat,” *The Int. J. of Robotics Research*, vol. 28, no. 9, pp. 1134–1153, 2009.
34. J. Ding, R. E. Goldman, K. Xu, P. K. Allen, D. L. Fowler, and N. Simaan, “Design and coordination kinematics of an insertable robotic effectors platform for Single-Port access surgery,” *IEEE/ASME Trans. Mechatron*., vol. 18, no. 5, pp. 1612–1624, Oct. 2013.
35. M.W. Hannan, I.D. Walker, “Analysis and Experiments with an Elephant’s Trunk Robot,” *Advanced Robotics*, Vol. 15, No. 8, pp. 847-858, 2001.
36. Z. Li and R. Du, "Design and Analysis of a Bio-Inspired Wire-Driven Multi-Section Flexible Robot," *Int. J. Adv. Robotic Sy*., vol. 10, 2013, pp. 288-299.
37. Y, Yang and W, Zhang. ET Arm: Highly Compliant Elephant-Trunk Continuum Manipulator. *Int. Conf. Intell. Robotics Applicat*. 2014.
38. V. Sujan and S. Dubowsky, “Design of a lightweight hyper- redundant deployable binary manipulator,” *J. Mech. Des*., vol. 126, no. 1, pp. 29–39, Jan. 2004.
39. V. A. Sujan, M. D. Lichter, and S. Dubowsky, “Lightweight hyper-redundant binary elements for planetary exploration robots,” in *Proc. IEEE/ASME Int. Conf. Advanced Intell. Mechatronics*, July 8–11, 2001, pp. 1273–1278.
40. S. M. Segreti, M. Kutzer, R. Murphy, and M. Armand, “Cable length prediction for a compliant surgical manipulator,” in *Proc. IEEE Int. Conf. Robot*. Autom., 2012.
41. J. Peirs, H. V. Brussel, D. Reynaerts, and G. D. Gersem, “A flexible distal tip with two degrees of freedom for enhanced dexterity in endoscopic robot surgery,” in *Proc. MME, The 13th Micromechanics Eur. Workshop*, Sinaia, Romania, 2002, pp. 271–274.
42. J. Lock, G. Laing, M. Mahvash, and P. E. Dupont, “Quasistatic modeling of concentric tube robots with external loads,” in *Proc. IEEE/RSJ Int. Conf. Intell. Robot. Syst*., 2010, pp. 2325–2332.
43. R. J. Webster, III, A. M. Okamura, and N. J. Cowan, “Toward active cannulas: Miniature snake-like surgical robots,” in *Proc. IEEE/RSJ Int. Conf. Intell. Robots Syst*. Oct. 9–15, 2006, pp. 2857–2863.

44. R. J. Webster, III, A. M. Okamura, and N. J. Cowan, “Kinematics and calibration of active cannulas,” in *Proc. IEEE Int. Conf. Robot. Autom*., 2008, pp. 3888–3895.
45. H. Su, D. C. Cardona, W. Shang, A. Camilo, G. A. Cole, D. C. Rucker, R. J. Webster, and G. S. Fischer, “A MRI-guided concentric tube continuum robot with piezoelectric actuation: A feasibility study,” in *Proc. IEEE Int. Conf. Robot. Autom*., 2012, pp. 1939–1945.
46. M. Mahvash and M. Zenati, “Toward a hybrid snake robot for single-port surgery,” in *Annual International Conference of the IEEE Engineering in Medicine and Biology Society*, 2011, pp. 5372–5375.
47. I. D. Walker and M. W. Hannan, “A novel elephant’s trunk robot,” in *Proc. IEEE/ASME Intl. Conf. on Advanced Intelligent Mechatronics*, Atlanta, GA, Sept. 1999, pp. 410–415.
48. F. Renda, M. Cianchetti, M. Giorelli, A. Arienti, and C. Laschi, “A 3D steady-state model of a tendon-driven continuum soft manipulator inspired by the octopus arm.” *Bioinspiration Biomimetics,* vol. 7, no. 2, p. 025006, 2012.
49. F. Renda, M. Giorelli, M. Calisti, M. Cianchetti, and C. Laschi, “Dynamic model of a multibending soft robot arm driven by cables,” I*EEE Trans. Robot*., vol. 30, no. 5, pp. 1109–1122, Oct. 2014.
50. H. Wang, W. Chen, X. Yu, T. Deng, X. Wang, and R. Pfeifer, “Visual servo control of cable-driven soft robotic manipulator,” in *Intelligent Robots and Systems (IROS), 2013 IEEE/RSJ Int. Conf. on*, Nov 2013, pp. 57–62.
51. M. Cianchetti, A. Arienti, M. Follador, B. Mazzolai, P. Dario, and C. Laschi, “Design concept and validation of a robotic arm inspired by the octopus,” *Mater. Sci. Eng. C*, vol. 31, pp. 1230–1239, 2011.
52. M. Cianchetti, M. Follador, B. Mazzolai, P. Dario, and C. Laschi, “Design and development of a soft robotic octopus arm exploiting embodied intelligence”, *IEEE Int. Conf. Robot. Autom*., 2012, pp. 5271-5276.
53. A. Bartow, A. Kapadia, and I. D. Walker, “A novel continuum trunk robot based on contractor muscles,” in *Proc. 12th WSEAS Int. Conf. Signal Process. Robot. Autom*., 2013, pp. 181–186.
54. H. Tsukagoshi, A. Kitagawa, and M. Segawa, “Active hose: An artificial elephant’s nose with maneuverability for rescue operation,” in *Proc. IEEE Int. Conf. Robot. Autom*., vol. 3, Seoul, Korea, May 2001, pp. 2454–2459.
55. M. B. Pritts and C. D. Rahn, “Design of an artificial muscle continuum robot,” in *Proc. IEEE Int. Conf. Robot. Autom*., vol. 5, New Orleans, LA, Apr. 2004, pp. 4742–4746.
56. R. K. Katzschmann, A. D. Marchese, and D. Rus, “Autonomous object manipulation using a soft planar grasping manipulator,” *Soft Robotics*, vol. 2, no. 4, pp.155-164, 2015.
57. R. Kang, D. T. Branson, T. Zheng, E. Guglielmino, and D. G. Caldwell, “Design, modeling and control of a pneumatically actuated manipulator inspired by biological continuum structures,” *Bioinspiration Biomimetics*, vol. 8, no. 3, p. 036008, 2013.
58. A. Stilli, H. Wurdemann, and K. Althoefer, “Shrinkable, stiffness-controllable soft manipulator based on a bio-inspired antagonistic

actuation principle," in *IEEE/RJS Inter. Conf. Intell. Robots Sys.*, 2014.
59. S. J. Bardaro and L. Swanstrom, "Development of advanced endoscopes for natural orifice transluminal endoscopic surgery (NOTES)," *Minimally Invas. Ther.*, vol. 15, no. 6, pp. 378–383, 2006.
60. Y. Chen, J. H. Chang, A. S. Greenlee, K. C. Cheung, A. H. Slocum, and R. Gupta, "Multi-turn, tension-stiffening catheter navigation system," in *Proc. IEEE Int. Conf. Rob. Autom*., Anchorage, AK, USA, May 2010, pp. 5570–5575.
61. Y.-J. Kim, S. Cheng, S. Kim, and K. Iagnemma, "A novel layer jamming mechanism with tunable stiffness capability for minimally invasive surgery," *IEEE Trans. Robot*., vol. 29, no. 4, pp. 1031–1042, Aug. 2013.
62. S. Sadati, Y. Noh, S. Naghibi, and A. Althoefer, "Stiffness control of soft robotic manipulators for minimally invasive surgery (mis) using scale jamming," in *Int. Conf. Rob. and Autom*., Amsterdam, The Netherlands, 2015, pp. 141–151.
63. C. Cao and X. Zhao, "Tunable stiffness of electrorheological elasto mers by designing mesostructures," *Appl. Phys. Lett*., vol. 103, no. 4, p. 041901, July 2013.
64. J. Neubert, A. Rost, and H. Lipson, "Self-soldering connectors for modular robots," *Transaction of Robotics*, vol. PP, no. 99, pp. 1–14, 2014.
65. Wikipedia. *Fusible Alloy*. Available from: https://en.wikipedia.org/wiki/Fusible_alloy.
66. L. Wang and F. Iida "Physical connection and disconnection control based on hot melt adhesives," *IEEE/ASME Trans. Mechatron*., vol. 18, no. 4, pp. 1397-1409, Aug. 2013.
67. L. Wang, L. Graber, and F. Iida, ''Large-payload climbing in complex vertical environments using thermoplastic adhesive bonds,'' *IEEE Trans. Robot*., vol. 29, no. 4, pp. 863–874, Aug. 2013.
68. WILLIAMROWLAND. *Lens Alloy*. Available from: http://www.william-rowland.com/pages/low-melting-point-alloy.
69. A. Scari, B. Pockszevnicki, J. Junior, and P. Magalhaes Junior, "Stress-Strain Compression of AA6082-T6 Aluminum Alloy at Room Temperature," *Journal of Structures*, vol. 2014, no. 387680, pp. 1-7, 2014.
70. ASTM Committee. Standard E9-09, Standard Test Methods of Compression Testing of Metallic Materials at Room Temperature, in: *Annual Book of ASTM Standards*, 3.01, 2012, pp. 92–100.
71. N. G. Cheng, Design and Analysis of Jammable Granular Systems, Ph.D. Thesis, Massachusetts Insitute of Technology, 2013.
72. Wikipedia. *Silicone Rubber*. Available from: https://en.wikipedia.org/wiki/Silicone_rubber.
73. ASTM Committee. Standard test methods for vulcanized rubber and thermoplastic rubbers and thermoplastic elastomers-Tension [D412-98]. New York: American National Standards Institute, 1998.
74. SMOOTH-ON. *Technical and Buying Information*. Available from: https://www.smooth-on.com/product-line/dragon-skin/.
75. S. Meghezi, F. Couet, P. Chevallier, and D. Mantovani, "Effects of a pseudophysiological environment on the elastic and viscoelastic

properties of collagen gels," *Int. J. of Biomaterials*, vol.2012, Article ID 319290, 9 pages, Jul. 2012.

76. J. L. Sparks, N. A. Vavalle, K. E. Kasting, B. Long, M. L. Tanaka, P. A. Sanger, K. Schnell, and T. A. Conner-Kerr, "Use of silicone materials to simulate tissue biomechanics as related to deep tissue injury," *Advances in Skin & Wound Care*, vol. 28, no. 2, pp. 59–68, Feb. 2015.
77. M. Hassan, M. Hamdi, and A. Noma, "The nonlinear elastic and viscoelastic passive properties of left ventricular papillary muscle of a guinea pig heart.", *J. Mech. Behav. Biomed*. Mater., vol. 5, no. 1, pp. 99– 109, Jan. 2012.
78. L. J. Huat, Customizable Soft Pneumatic Gripper Devices. Master Thesis, National University of Singapore, 2015.
79. R. Soddhi and M. Sonnenberg, "Use of snap-fit fasteners in the multi-life-cycle design of products," in *IEEE Intl. Symp. on Electr. & Env*., 1999.
80. P. A. Tres, *Designing plastic parts for assembly*, 5th ed. Cincinnati, OH: Hanser Gardner Publ., 2003.
81. Stratasys, *PolyJet Materials Datasheet*. Available from: http://www.stratasys.com/polyjet.
82. M. A. Salama, W. M. Rowe, and R. K. Yasui, "Thermoelastic Analysis of Solar Cell Arrays and their Material Properties", Jet Propulsion Lab., JPL-TM-33-626, 1973.
83. F. Schneider, T. Fellner, J. Wilde, U. Wallrabe, "Mechanical Properties of Silicones for MEMS", *J. Micromech. Microeng*., vol. 18, no. 6, Apr. 2008.

Appendix A
MATLAB .m files

This section contains the .m files developed and used in the thesis.

A.1 hyperelasticity_model.m

This section of code reads the data from tensile experiments (Ecoflex 0030 and Dragon Skin 30) and plots the fitting curve.

```
clc
clear

%read uniaxial test data
data=xlsread('/Users/bingyinma/Documents/MATLAB/DragonSkin_Specimen.xls');
%data=xlsread('/Users/bingyinma/Documents/MATLAB/Ecoflex_Specimen.xls');


Stress=data(:,7); %Engineering stress
Stretch=data(:,8); %Stretch values

%polynomial fit of experimental stress-stretch curve
Pol_UT=polyfit(Stretch, Stress, 5); %fifth order polynomial


%calculate tension data to be fitted with function
r=length(Stretch);
Stretch_max=max(Stretch);
Stretch=linspace (1, Stretch_max, r); %stretch values equally spaced between 1 and Stretch_max
PKF_UT=polyval(Pol_UT,Stretch); %PK stress corresponding to 'Stretch'

%calculation of optimal material parameters
STR=[Stretch];
STS=[PKF_UT];

%NeoHookean model
NeoHookean_C0= [10];

% Yeoh model
Yeoh_C0 = [10, 2, 1]; %Initial guess
Yeoh_lb = [0, 0, -inf]; %Lower bound of the optimal solution vector
Yeoh_ub = [inf, inf, inf]; %Upper bound of the optimal solution vector

%Mooney3 model
Mooney3_C0 = [0.03, 2, 2];
Mooney3_lb = [-inf, 0, -inf]; %Lower bound of the optimal solution vector
Mooney3_ub = [inf, inf, inf]; %Upper bound of the optimal solution vector
```

```
% Mooney5 model
Mooney5_C0 = [0.03, 4, 5, 6, 2]; %Initial guess
Mooney5_lb = [-inf, -inf, -inf, -inf, -inf]; %Lower bound of the optimal solution
vector
Mooney5_ub = [inf, inf, inf, inf, inf]; %Upper bound of the optimal solution
vector

% Ogden2 model
Ogden2_C0 = [0.03, 4, 5, 6]; %Initial guess
Ogden2_lb = [-inf, -inf, -inf, -inf]; %Lower bound of the optimal solution
vector
Ogden2_ub = [inf, inf, inf, inf]; %Upper bound of the optimal solution vector

%Arruda model
Arruda_C0 = [10, 2]; %Initial guess
Arruda_lb = [-inf, -inf]; %Lower bound of the optimal solution vector
Arruda_ub = [inf, inf]; %Upper bound of the optimal solution vector

optnew = optimset('DiffMaxChange',0.000001,'DiffMinChange',1e-15,...
    'TolFun',1e-15, 'TolX',1e-15,'MaxFunEvals',10000,'MaxIter',10000);

%curve fit options
[NeoHookean_C, NeoHookean_sse] = lsqcurvefit(@NeoHookean,
NeoHookean_C0,STR,STS);

[Yeoh_C, Yeoh_sse] =
lsqcurvefit(@Yeoh,Yeoh_C0,STR,STS,Yeoh_lb,Yeoh_ub,optnew); %Yeoh
optimal solution

[Mooney3_C, Mooney3_sse] =
lsqcurvefit(@Mooney3,Mooney3_C0,STR,STS,Mooney3_lb,Mooney3_ub,op
tnew); %Mooney3 optimal solution

[Mooney5_C, Mooney5_sse] =
lsqcurvefit(@Mooney5,Mooney5_C0,STR,STS,Mooney5_lb,Mooney5_ub,op
tnew); %Mooney5 optimal solution

[Ogden2_C, Ogden2_sse] =
lsqcurvefit(@Ogden2,Ogden2_C0,STR,STS,Ogden2_lb,Ogden2_ub,optnew
); %Ogden2 optimal solution

[Arruda_C, Arruda_sse] =
lsqcurvefit(@Arruda,Arruda_C0,STR,STS,Arruda_lb,Arruda_ub,optnew); %A
rruda optimal solution

%plot the fitting curve
times=linspace(STR(1),STR(end));
figure(1)

plot(times,NeoHookean(NeoHookean_C,times))
```

```
hold on
plot(times,Yeoh(Yeoh_C,times),'g-')
hold on
plot(times,Mooney3(Mooney3_C,times),'y')
hold on
plot(times,Mooney5(Mooney5_C,times),'b-') %plot Mooney5 model curve
hold on
plot(times,Ogden2(Ogden2_C,times),'r-')
hold on
plot(times,Arruda(Arruda_C,times),'--')
hold on
plot(Stretch, Stress, 'k-')

legend('Neo Hookean Fitting Curve','Yeoh Fitting Curve','3 term Mooney-Rivlin Fitting Curve','5 term Mooney-Rivlin Fitting Curve','2 term Ogden Fitting Curve','Arruda-Boyce Fitting Curve','Experimental Data')
xlabel('Stretch')
ylabel('Stress (MPa)')

title('Hyperelastic Models Fitting Curves')
```

A.2 Arruda.m

This section of code describes Arruda-Boyce function.

```
%%%%%%%%%%%%%%%%%%%%%%%%%%%%%%%%%%%%%%%%%%%%%
%%%%%Stress for Arruda model%%%%%%%%%%%%%%%%%%%%%%%%%%%%%%%%%%%%%%
function [S] = arruda(C,STR)
%material constants
mu1=C(1);
lambda=C(2);
S=2.*mu1.*(STR-1./STR.^2).*[1./2+1./10.*(STR.^2+2./STR).*1./lambda.^2+ ...
   33./1050.*(STR.^2+2./STR).^2.*1./lambda.^4+ ...
   76./7050.*(STR.^2+2./STR).^3.*1./lambda.^6+ ...
   2595./673750.*(STR.^2+2./STR).^4.*1./lambda.^8];
end
```

A.3 Mooney3.m

This section of code describes 3-term Mooney-Rivlin function.

```
%%%%%%%%%%%%%%%%%%%%%%%%%%%%%%%%%%%%%%%%%%%%%
%%%%%Stress for Mooney3 model%%%%%%%%%%%%%%%%%%%%%%%%%%%%%%%%%%%%%%
function [S] = Mooney3(C,Stretch)
%material constants
mu1=C(1);
mu2=C(2);
mu3=C(3);
```

```
S=2.*mu1.*(Stretch-1./Stretch.^2)+ ... %Strain energy first term
   2.*mu2.*(1-1./Stretch.^3)+ ... %Strain energy second term
   6.*mu3.*(Stretch.^2-Stretch-1+1./Stretch.^2+1./Stretch.^3-
1./Stretch.^4); %Strain energy third term
end
```

A.4 Mooney5.m

This section of code describes 5-term Mooney-Rivlin function.

```
%%%%%%%%%%%%%%%%%%%%%%%%%%%%%%%%%%%%%%%%%%%%%
%%%%%Stress for Mooney5
model%%%%%%%%%%%%%%%%%%%%%%%%%%%%%%%%%%%%%%%
function [S] = Mooney5(C,Stretch)
%material constants
mu1=C(1);
mu2=C(2);
mu3=C(3);
mu4=C(4);
mu5=C(5);
S=2.*mu1.*(Stretch-1./Stretch.^2)+ ... %Strain energy first term
   2.*mu2.*(1-1./Stretch.^3)+ ... %Strain energy second term
   6.*mu3.*(Stretch.^2-Stretch-1+1./Stretch.^2+1./Stretch.^3-
1./Stretch.^4)+ ...%Strain energy third term
   4.*mu4.*(Stretch.^2+2./Stretch-3).*(Stretch-1./Stretch.^2)+ ... ...%Strain
energy fourth term
   4.*mu5.*(2.*Stretch+1./Stretch.^2-3).*(1-1./Stretch.^3); ...%Strain energy
fifth term
end
```

A.5 Ogden2.m

This section of code describes 2-term Ogden function.

```
%%%%%%%%%%%%%%%%%%%%%%%%%%%%%%%%%%%%%%%%%%%%%
%%%%%Stress for Ogden2
model%%%%%%%%%%%%%%%%%%%%%%%%%%%%%%%%%%%%%%%
function [S] = ogden2(C,L)
%material constants
mu1=C(1); alpha1=C(2);
mu2=C(3); alpha2=C(4);
S=mu1.*(L.^(alpha1-1)-L.^(-(1+alpha1./2)))+ ... %Strain energy first term
   mu2.*(L.^(alpha2-1)-L.^(-(1+alpha2./2))); %Strain energy second term
end
```

A.6 Yeoh.m

This section of code describes 3-term Yeoh function.

```
%%%%%%%%%%%%%%%%%%%%%%%%%%%%%%%%%%%%%%%%%%%%%%%%%%%%%%%%%%%%%%%%%%%%%%%%%%%%%%%%%%%%%%%%%%%%%%
%%%%%Stress for Yeoh
model%%%%%%%%%%%%%%%%%%%%%%%%%%%%%%%%%%%%%%%%%%%%%%%%%%%%%%
function [S] = Yeoh(C,Stretch)
%material constants
mu1=C(1);
mu2=C(2);
mu3=C(3);
S=2.*(Stretch-1./Stretch.^2).*[mu1+2*mu2.*(Stretch.^2+2./Stretch-
3)+3*mu3.*(Stretch.^2+2./Stretch-3).^2];
end
```

A.7 linear_regression.m

This section of code reads the test data from tensile experiments (Ecoflex 0030 and Dragon Skin 30) and plots a linear regression fitting curve.

```
clc
clear

%read uniaxial test data
%
data=xlsread('/Users/bingyinma/Documents/MATLAB/DragonSkin_Specime
n.xls'); %load DragonSkin data
data=xlsread('/Users/bingyinma/Documents/MATLAB/Ecoflex_Specimen.xls'
); %load Ecoflex data

Stress=data(:,4); %Engineering Stress
Strain=data(:,5); %Strain Values

% index=(Strain>=0.75)&(Strain<=2); % Get the index of DragonSkin 30
index=(Strain>=0.75)&(Strain<=6); % Get the index of Ecoflex 0030

p=polyfit(Strain(index),Stress(index),1); % Fit polynomial coefficients for line
yfit = p(2)+Strain(index).*p(1);  % Compute the best-fit line
plot(Strain,Stress,'o');            % Plot the data
hold on              % Add to the plot
plot(Strain(index),yfit,'--');     % Plot the best-fit line

legend('Stress-Strain Curve','Linear Regression Curve')
xlabel('Strain')
ylabel('Stress (N/mm^2)')
```

Appendix B
Results from Lateral Displacement Tests

This section contains the results from lateral displacement experiments.

B.1 Surface Bonding Modules

The following data presents lateral displacements of the revolute joint that employs HMA-based locking mechanism in locking state.

Load (gram)	Load (N)	Displacement (mm)		
		Trial 1	Trial 2	Trial 3
0	0	0	0	0
50	0.49	0.3	0.2	0.3
100	0.98	0.5	0.5	0.5
150	1.47	0.6	0.8	0.8
200	1.96	1	1.1	1.2
250	2.45	1.3	1.5	1.6
300	2.94	1.5	1.8	2.1
350	3.43	1.7	2.1	2.6
400	3.92	2.1	2.2	2.8
450	4.41	2.4	2.5	3.4
500	4.9	2.7	2.9	3.7
550	5.39	3.1	3.3	4.2
600	5.88	3.4	3.9	4.7
650	6.37	3.8	4.2	5.2
700	6.86	4.4	4.5	5.9
750	7.35	4.7	5.5	6.7
800	7.84	5.2	6	7.1
850	8.33	5.6	6.5	7.7
900	8.82		7	8
950	9.31		7.5	9.2

1000	9.8		8.1	

The following data presents lateral displacements of the revolute joint that employs LMPS-based locking mechanism in locking state.

Load (gram)	Load (N)	Displacement (mm)		
		Trial 1	Trial 2	Trial 3
0	0	0	0	0
50	0.49	0.01	0.02	0.01
100	0.98	0.07	0.05	0.04
150	1.47	0.1	0.11	0.1
200	1.96	0.2	0.16	0.14
250	2.45	0.25	0.21	0.2
300	2.94	0.3	0.25	0.24
350	3.43	0.35	0.32	0.3
400	3.92	0.5	0.38	0.33
450	4.41	0.55	0.47	0.38
500	4.9	0.65	0.54	0.44
550	5.39	0.7	0.59	0.49
600	5.88	0.9	0.65	0.53
650	6.37	0.95	0.75	0.58
700	6.86	1	0.84	0.65
750	7.35	1.05	0.92	0.7
800	7.84	1.15	0.99	0.84
850	8.33	1.3	1.04	0.9
900	8.82	1.4	1.1	0.95
950	9.31	1.5	1.15	1.01
1000	9.8	1.7	1.22	1.14
1050	10.29	1.9	1.28	1.31
1100	10.78	2.1	1.34	1.52

1150	11.27	2.2	1.42	1.61
1200	11.76	2.3	1.54	1.67
1250	12.25	2.5	1.64	1.99
1300	12.74	2.7	1.7	
1350	13.23	3		

The following data presents lateral displacements of the spherical joint that employs HMA-based locking mechanism in locking state.

Load (gram)	Load (N)	Displacement (mm)		
		Trial 1	Trial 2	Trial 3
0	0	0	0	0
50	0.49	0.15	0.04	0.4
100	0.98	0.26	0.12	0.6
150	1.47	0.54	0.24	0.8
200	1.96	0.9	0.37	1
250	2.45	1.04	1	1.35
300	2.94	1.64	1.15	1.48
350	3.43	1.98	1.38	1.7
400	3.92	2.2	1.77	1.78
450	4.41	2.53	2.2	1.99
500	4.9	2.9	2.5	2.42
550	5.39	3.14	2.9	2.53
600	5.88	3.32	3.12	2.69
650	6.37	3.93	3.39	2.8
700	6.86	4.2	3.68	3.3
750	7.35	5	4.12	3.59
800	7.84	5.7	4.3	3.99
850	8.33	5.92	4.5	4.42
900	8.82	6.2	4.8	4.73

950	9.31	6.9	5.12	5.1
1000	9.8	8	5.4	5.8
1050	10.29	8.6	6.41	6.5
1100	10.78	9.5	6.8	7.3
1150	11.27		7.6	8.4
1200	11.76		8.4	9.3
1250	12.25		9.1	
1300	12.74		9.8	

The following data presents lateral displacements of the spherical joint that employs LMPS-based locking mechanism in locking state.

Load (gram)	Load (N)	Displacement (mm)		
		Trial 1	Trial 2	Trial 3
0	0	0	0	0
50	0.49	0.01	0.09	0.07
100	0.98	0.02	0.16	0.16
150	1.47	0.04	0.24	0.29
200	1.96	0.07	0.28	0.42
250	2.45	0.09	0.36	0.5
300	2.94	0.13	0.42	0.67
350	3.43	0.17	0.56	0.89
400	3.92	0.21	0.67	1.12
450	4.41	0.26	0.74	1.44
500	4.9	0.29	0.78	1.8
550	5.39	0.33	0.84	2.04
600	5.88	0.46	0.9	2.12
650	6.37	0.65	0.95	2.17
700	6.86	0.77	1.06	2.23
750	7.35	0.85	1.24	2.26

800	7.84	0.97	1.42	2.32
850	8.33	1.12	1.53	2.38
900	8.82	1.26	1.59	2.42
950	9.31	1.38	2.04	2.47
1000	9.8	1.52	2.24	2.56
1050	10.29	1.69	2.47	2.6
1100	10.78	1.79	2.72	2.76
1150	11.27	1.97	2.88	2.87
1200	11.76	2.06	2.99	3.04
1250	12.25	2.39	3.12	3.33
1300	12.74	3.22	3.24	3.52
1350	13.23		3.32	3.63
1400	13.72		3.43	3.75
1450	14.21		3.51	4.09
1500	14.7		3.69	4.44
1550	15.19		3.92	4.59
1600	15.68		4.16	4.73
1650	16.17		4.38	
1700	16.66		4.66	
1750	17.15		4.81	
1800	17.64		4.92	

The following data presents lateral displacements of the revolute joint without locking mechanism.

Load (gram)	Load (N)	Displacement (mm)		
		Trial 1	Trial 2	Trial 3
0	0	0	0	0
10	0.098	3.4	3	2.8
20	0.196	6.4	5.8	6.4

30	0.294	8.7	9.6	9.1
40	0.392	13.4	13.4	14.4
50	0.49	15.2	15	15
60	0.588	15.9	16.6	16.2
70	0.686	17.5	17.1	17.1
80	0.784	18.3	17.7	18.2
90	0.882	18.9	18.6	19.3
100	0.98	20.1	19.1	20.2
110	1.078	20.7	20.1	20.8
120	1.176	21.5	20.7	21.5
130	1.274	22.3	21.1	22
140	1.372	22.8	22.1	22.7
150	1.47	23.5	22.6	23.5

The following data presents lateral displacements of the revolute joint that employs HMA-based locking mechanism in unlocking state.

Load (gram)	Load (N)	Displacement (mm)		
		Trial 1	Trial 2	Trial 3
0	0	0	0	0
10	0.098	2.98	4	4.1
20	0.196	6.5	7.6	7.8
30	0.294	9.7	11.5	11.7
40	0.392	14.3	15.6	15.7
50	0.49	17.52	16.6	16.9
60	0.588	18	18.3	19
70	0.686	19.7	20	20.3
80	0.784	21	21.2	21.7
90	0.882	22.6	22.2	22.7
100	0.98	23.8	23.6	23.4

110	1.078	24.88	24.4	24.7
120	1.176	25.8	25.1	25.3
130	1.274	26.9	26.2	26.2

The following data presents lateral displacements of the revolute joint that employs LMPS-based locking mechanism in unlocking state.

Load (gram)	Load (N)	Displacement (mm)		
		Trial 1	Trial 2	Trial 3
0	0	0	0	0
10	0.098	3.85	3.2	3.3
20	0.196	6.05	6.5	6.6
30	0.294	9.35	9.5	10.3
40	0.392	13.55	14.2	14.6
50	0.49	15.85	15.5	15.8
60	0.588	17.85	17.5	17.9
70	0.686	19.65	19.8	19.3
80	0.784	20.95	20.8	20.6
90	0.882	22.35	22	22
100	0.98	23.55	23.2	22.9
110	1.078	24.65	24.4	24
120	1.176	25.85	25.2	24.7
130	1.274	26.83	26.3	25.6

The following data presents lateral displacements of the spherical joint without locking mechanism.

Load (gram)	Load (N)	Displacement (mm)		
		Trial 1	Trial 2	Trial 3
0	0	0	0	0
10	0.098	3.4	2.9	3

20	0.196	6.5	6.2	6.6
30	0.294	10	9.9	9.3
40	0.392	14	13.6	13.1
50	0.49	15.8	15.3	14.6
60	0.588	16.4	17.1	16.8
70	0.686	19.1	18.2	18.7
80	0.784	19.6	19.4	20.2
90	0.882	20.62	20.3	21.6
100	0.98	21.5	21.2	22.3
110	1.078	22.3	22	23.4
120	1.176	23	23	24.2
130	1.274	24.2	23.8	25
140	1.372	25.1	24.9	25.4
150	1.47	25.4	25.3	26.2
160	1.568	26.3	26.5	26.7
170	1.666	27.3	27.1	27.2

The following data presents lateral displacements of the spherical joint that employs HMA-based locking mechanism in unlocking state.

Load (gram)	Load (N)	Displacement (mm)		
		Trial 1	Trial 2	Trial 3
0	0	0	0	0
10	0.098	5	4.9	5.1
20	0.196	9.6	10	9.9
30	0.294	14.7	15.3	15.7
40	0.392	18.6	18.5	18.8
50	0.49	19.8	19.9	20.3
60	0.588	22.7	22.6	22.9
70	0.686	24.9	25.1	25.6

80	0.784	26.9	27.1	27.3

The following data presents lateral displacements of the spherical joint that employs LMPS-based locking mechanism in unlocking state.

Load (gram)	Load (N)	Displacement (mm)		
		Trial 1	Trial 2	Trial 3
0	0	0	0	0
10	0.098	6.4	6.7	6.7
20	0.196	11.5	11.5	11.7
30	0.294	16.6	17.3	17.4
40	0.392	19.6	20.4	20.4
50	0.49	20.7	21.1	21.3
60	0.588	22.5	22.3	23.5
70	0.686	24.6	24.7	25.2
80	0.784	26.4	26.4	26.7

B.2 Phase Change Modules

The following data presents lateral displacements of LMPA-based single modules in rigid state.

Load (gram)	Load (N)	Displacement (mm)		
		Trial 1	Trial 2	Trial 3
0	0	0	0	0
100	0.98	5.65	6.58	7.54
150	1.47	8.18	9.64	10.5
200	1.96	10.59	12.37	12.59
250	2.45	13.03	14.76	15.42
300	2.94	15.07	16.01	18.44
350	3.43	17.31	17.86	21.05

400	3.92	19.52	19.61	23.92
450	4.41	20.09	21.84	25.76
500	4.9	21.37	23.91	27.7
550	5.39	22.62	24.95	28.64
600	5.88	24.52	26.96	29.69
650	6.37	25.55	28.49	30.69
700	6.86	27.28	29.35	32.71
750	7.35	29.34	30.51	33.8
800	7.84	29.34	32.18	34.37
850	8.33	30.08	33.93	35.59
900	8.82	32.33	34.41	36.81
950	9.31	33.2	35.35	37.61
1000	9.8	33.71	36.3	38.08

The following data presents lateral displacements of GM-based single modules in rigid state.

Load (gram)	Load (N)	Displacement (mm)		
		Trial 1	Trial 2	Trial 3
0	0	0	0	0
50	0.49	7	7.33	5.64
100	0.98	12.34	14.08	10.51
150	1.47	17.04	19.57	15.21
200	1.96	22.39	22.86	19.06
250	2.45	27	25.74	21.53
300	2.94	29.9	29.66	24.38
350	3.43	35.02	32.27	25.76
400	3.92	35.85	35.89	28.44
450	4.41	38.04	37.01	30.15

The following data presents lateral displacements of the single module without controllable stiffness element.

Load (gram)	Load (N)	Displacement (mm)		
		Trial 1	Trial 2	Trial 3
0	0	0	0	0
10	0.098	2.1	1.9	2.4
20	0.196	4.2	3.6	4.1
30	0.294	6	5.2	6.4
40	0.392	7.8	7.3	7.7
50	0.49	8.6	8.3	8.7
60	0.588	10.7	10.2	10.7
70	0.686	12.1	12.1	12.4
80	0.784	13.8	13.6	14
90	0.882	15.4	15.3	15.6
100	0.98	16.8	16.9	16.7
110	1.078	17.9	18.2	18.1
120	1.176	19.2	19.6	19.3
130	1.274	20.3	20.9	20.4
140	1.372	21.4	22	21.6
150	1.47	22.3	23	22.5
160	1.568	23.4	24.2	23.5

The following data presents lateral displacements of LMPA-based single modules in soft state.

Load (gram)	Load (N)	Displacement (mm)		
		Trial 1	Trial 2	Trial 3
0	0	0	0	0
10	0.098	2.9	3.7	3.6
20	0.196	6.3	6.7	6.5

30	0.294	8.2	9.1	8.9
40	0.392	10.6	11.7	11.6
50	0.49	11.6	12.9	12.8
60	0.588	13.4	14.8	14.5
70	0.686	15.4	16.5	15.9
80	0.784	17	17.7	18.1
90	0.882	18.7	18.7	19.6
100	0.98	20.4	20.7	20.7
110	1.078	22	22	21.9
120	1.176	23.4	23.5	23.2

The following data presents lateral displacements of GM-based single modules in soft state.

Load (gram)	Load (N)	Displacement (mm)		
		Trial 1	Trial 2	Trial 3
0	0	0	0	0
10	0.098	1.2	1.2	1.2
20	0.196	2.6	2.35	2
30	0.294	3.9	3.6	3.3
40	0.392	5.5	4.8	4.5
50	0.49	6.4	5.6	6.3
60	0.588	7.9	6.9	7.1
70	0.686	9	8.2	8.2
80	0.784	10.1	9.4	9.4
90	0.882	11.3	10.5	10.9
100	0.98	12.9	11.6	12.2
110	1.078	14	13.2	13.6
120	1.176	15.1	14.3	14.5
130	1.274	16.2	15.3	15.5

140	1.372	17	16.2	16.4
150	1.47	17.8	17.3	18
160	1.568	18.9	18.3	18.8
170	1.666	19.9	19.2	19.8
180	1.764	20.5	20.2	20.7
190	1.862	21.3	20.9	21.7
200	1.96	22.1	21.9	22.3

Appendix C
Results from Response Time Tests

This section contains results from response time (rigidifying time and softening time) tests

C.1 Softening Time

The following data describes the softening time for single modules.

	Power	HMA(R) softening time
Unit	W	s
Trial 1	3.64	9.18
Trial 2	3.9	10.57
Trial 3	4.55	8.82
Trial 4	3.77	7.43
Trial 5	3.12	6.91
Trial 6	3.77	6.3
Trial 7	4.03	10.43
Trial 8	3.25	7.98
Trial 9	3.64	7.54
Trial 10	3.77	8.3
Trial 11	3.77	6.37
Trial 12	3.64	6.74

	Power	LMPS(R) softening time
Unit	W	s
Trial 1	3	15.45
Trial 2	2.64	9.24
Trial 3	2.9	15.58
Trial 4	2.88	5.81

Trial 5	3	16.51
Trial 6	3	10.76
Trial 7	2.5	12.75
Trial 8	3	19.96
Trial 9	3	9.64
Trial 10	2.9	15.67
Trial 11	3	11.84
Trial 12	3.12	13.21

	Power	HMA(S) softening time
Unit	W	s
Trial 1	3.24	23
Trial 2	3	19.21
Trial 3	2.64	21.12
Trial 4	3.24	16.85
Trial 5	2.16	21.77
Trial 6	3.24	16.79
Trial 7	2.04	19.09
Trial 8	3	14.9
Trial 9	3.12	18.5
Trial 10	2.16	18.39
Trial 11	2.04	18.22
Trial 12	2.4	15.31

	Power	LMPS(S) softening time
Unit	W	s
Trial 1	3.64	31.84
Trial 2	3.51	27.99

Trial 3	3.77	43.49
Trial 4	3.51	23.98
Trial 5	3.51	21.59
Trial 6	3.38	27.25

	Power	LMPA softening time
Unit	W	s
Trial 1	10.695	63.9
Trial 2	9.66	73
Trial 3	7.935	67.3
Trial 4	9.315	64.44
Trial 5	9.315	60.83
Trial 6	8.625	53.17
Trial 7	7.935	68.17
Trial 8	7.935	51.2
Trial 9	7.935	67.27

C.2 Rigidifying Time

The following data describes the rigidifying time for single modules.

	HMA(R) rigidifying time
Unit	s
Trial 1	47.56
Trial 2	56.19
Trial 3	41.76
Trial 4	39.78
Trial 5	36.88
Trial 6	43.04
Trial 7	46.15

Trial 8	33.63
Trial 9	48.5
Trial 10	33.04

	LMPS(R) rigidifying time
Unit	s
Trial 1	9.71
Trial 2	8.88
Trial 3	6.24
Trial 4	6.86
Trial 5	5.93
Trial 6	10.18
Trial 7	6.49
Trial 8	6.63
Trial 9	7.61
Trial 10	5.07
Trial 11	8.14
Trial 12	11.51

	HMA(S) rigidifying time
Unit	s
Trial 1	31.55
Trial 2	31.5
Trial 3	24.27
Trial 4	34.29
Trial 5	18.78
Trial 6	29.62
Trial 7	29.6
Trial 8	34.02

Trial 9	28.08
Trial 10	42.81
Trial 11	28.04
Trial 12	30.08

	LMPS(S) rigidifying time
Unit	s
Trial 1	22.67
Trial 2	15.73
Trial 3	20.65
Trial 4	18.27
Trial 5	18.5
Trial 6	15.25

	LMPA rigidifying time
Unit	s
Trial 1	128.53
Trial 2	92.46
Trial 3	113.02
Trial 4	150.94
Trial 5	137.42
Trial 6	135.6
Trial 7	67
Trial 8	84.3
Trial 9	118.46

Appendix D
CAD Models of the Moulds for Silicone Material Casting

This section contains the CAD models of the moulds for silicone material casting.

CAD models of the moulds for the fabrication of the bellows-like structure of surface bonding module are listed as bellow:

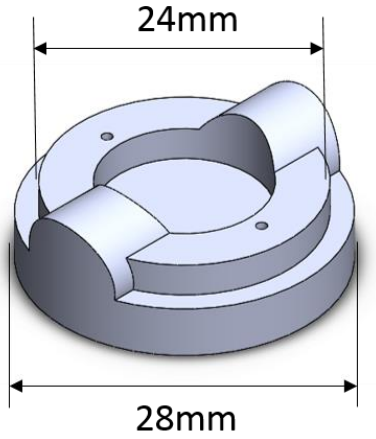

(a) End

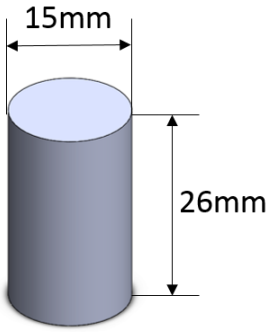

(b) Cylinder

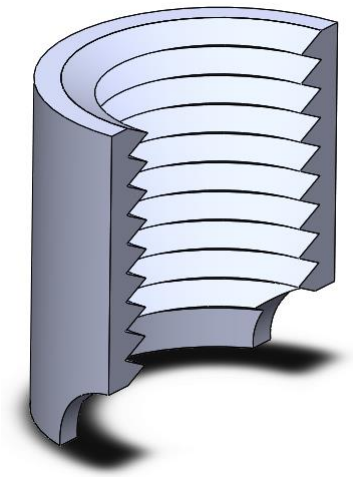

(c) Semi-Ring

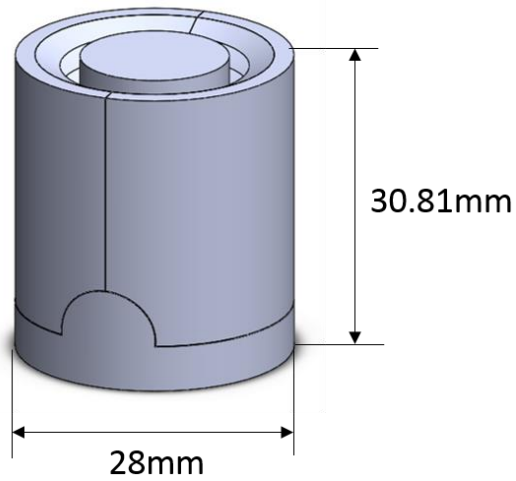

(d) Assembled Mould for R-Joint

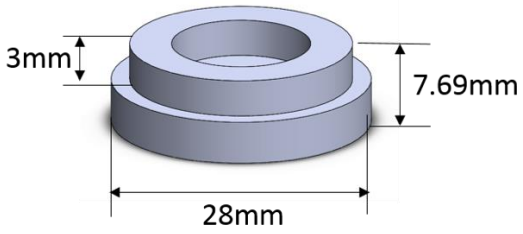

(e) End

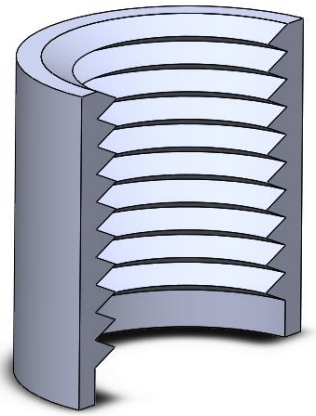

(f) Semi-Ring

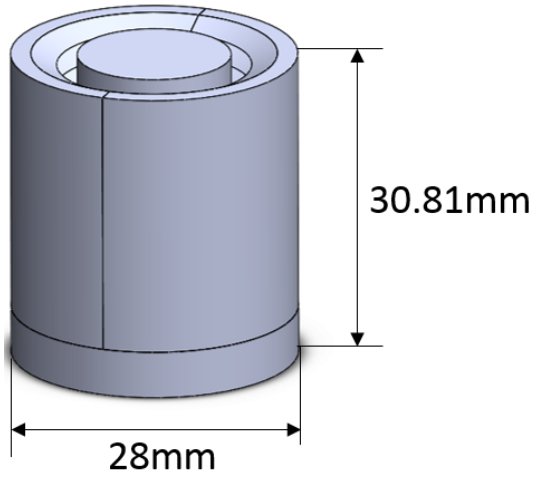

(g) Assembled Mould for S-Joint

CAD models of the moulds for the fabrication of the phase change module are listed as bellow:

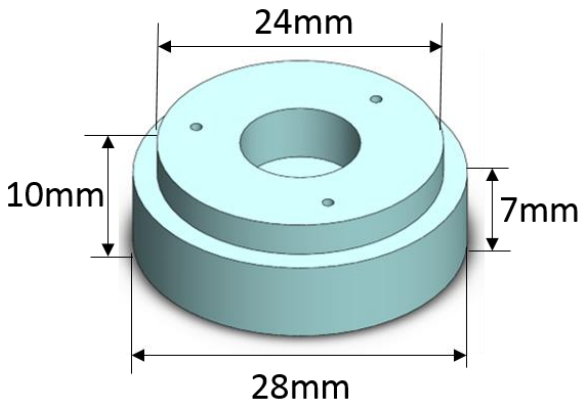

(a) End

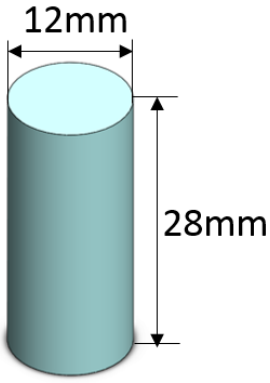

(b) Cylinder

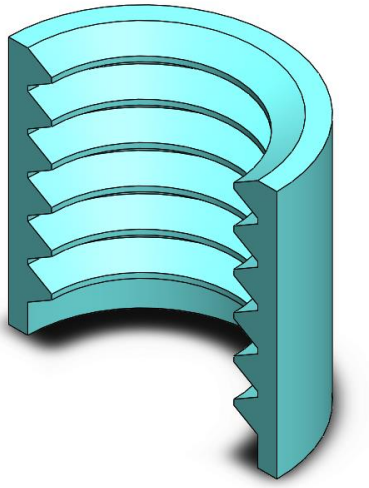

(c) Semi-Ring

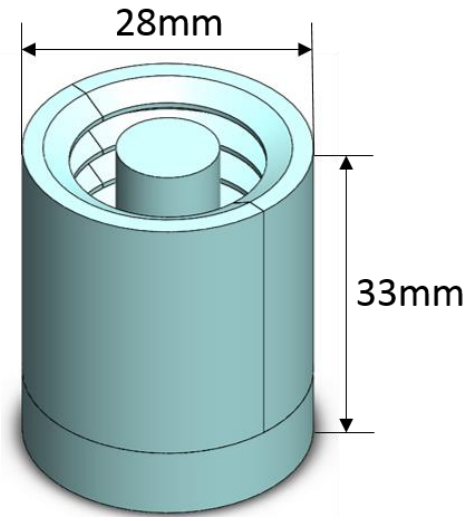

(d) Assembled Mould for Bellow

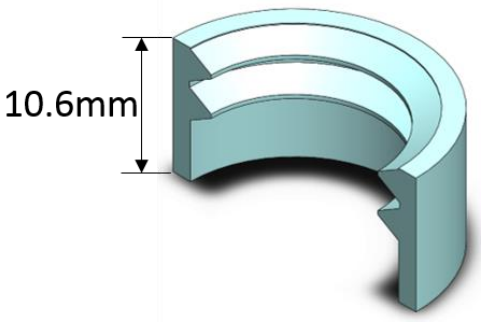

(e) Semi-Ring for Top Cap

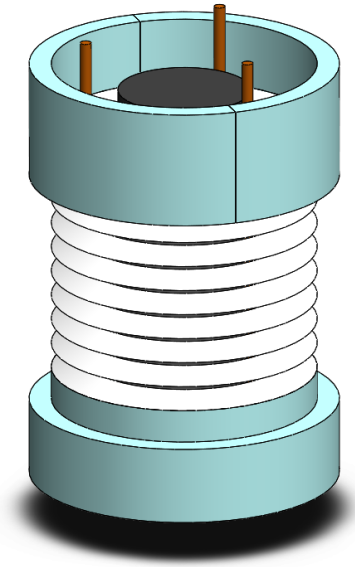

(f) Assembled Mould for Top Cap